Electromagnetic Properties of ^{21}O and the Self-Calibration of Compton Tracking Arrays

Elektromagnetische Eigenschaften von ^{21}O und die Selbstkalibrierung von Compton Tracking Arrays
vom Fachbereich Physik der Technischen Universität Darmstadt
zur Erlangung des Grades eines Doktors der Naturwissenschaften (Dr. rer. nat.)
genehmigte Dissertation von Sebastian Heil aus Frankfurt am Main
Darmstadt 2018 — D 17

1. Gutachten: Dr. Marina Petri
2. Gutachten: Prof. Dr. Thomas Aumann

TECHNISCHE
UNIVERSITÄT
DARMSTADT

Fachbereich Physik
Institut für Kernphysik

Electromagnetic Properties of ^{21}O and the Self-Calibration of Compton Tracking Arrays
Elektromagnetische Eigenschaften von ^{21}O und die Selbstkalibrierung von Compton Tracking Arrays

Genehmigte Dissertation von Sebastian Heil aus Frankfurt am Main

1. Gutachten: Dr. Marina Petri
2. Gutachten: Prof. Dr. Thomas Aumann

Tag der Prüfung: 20. Februar 2019
Veröffentlichung auf TUprints: 2019

Darmstadt, Technischen Universität Darmstadt — D 17

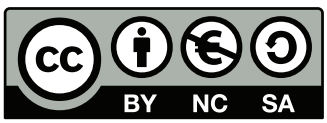

Abstract

The structure of exotic nuclei and in particular electromagnetic transitions between bound excited states are key spectroscopic observables, which provide an unparalleled testing ground for state-of-the-art nuclear interactions. Motivated by conflicting predictions from phenomenological and realistic nuclear interactions, this thesis reports on the measurement of the lifetime of the first excited state in ^{21}O and the branching ratio of its second excited state. The experiment was performed at the NSCL, using the S800 spectrograph for the detection of the reaction products. GRETINA was used for the γ-ray detection and the TRIPLEX plunger set-up guaranteed sensitivity to the lifetime. Measurements were taken using a ^{9}Be target, as well as a target degrader combination at 25 mm and 45 mm separation with a ^{181}Ta foil as the degrader. All measurements are compared to simulated spectra. The thereby measured lifetime results in $\tau_{1/2^+}=420^{+35}_{-32}(\text{stat})^{+34}_{-12}(\text{sys})$ ps, while the branching ratio is determined as $\text{BR}\left(3/2^+\rightarrow 1/2^+\right)=(11.7\pm 1.2)\%$. Comparisons are drawn to predictions from effective shell-model calculations based on the USDB interaction, as well as to ab-initio calculations building upon IM-SRG with interactions derived from chiral EFT.

Furthermore, this thesis reports on the development of a novel and notably simple method to generate a reliable, experimental signal basis for Compton tracking arrays, such as GRETINA and advanced gamma tracking array (AGATA). These detector systems use the signal basis for the position reconstruction of interactions inside the detector volume. However, obtaining a high-fidelity signal basis for such detector systems remains a big technological challenge, which hinders their optimal operation. The proposed method uses the surrounding detectors to iteratively calibrate each other by exploiting the characteristics of Compton scattering. This enables Compton tracking arrays to perform a self-calibration of their position sensitive response in-situ, opening up the way for reaching their optimum performance for the first time.

Zusammenfassung

Die Struktur exotischer Kerne, insbesondere die elektromagnetischen Übergänge zwischen gebundenen, angeregten Zuständen, bilden eine entscheidende Grundlage zum Testen neuester Interaktionen für kernphysikalische Modelle. Motiviert durch widersprüchliche Vorhersagen basierend auf phänomenologischen und realistischen Interaktionen, berichtet diese Arbeit von der Messung der Lebenszeit des ersten angeregten Zustands in ^{21}O und des Verzweigungsverhältnisses des zweiten angeregten Zustands. Die Messung wurde am NSCL durchgeführt. Zur Identifikation der Reaktionsprodukte wurde der S800 Spektrograph eingesetzt, während GRETINA zur Detektion der entstehenden γ Strahlung verwendet wurde. Die Messung der Lebenszeit wurde dabei durch den Einsatz des TRIPLEX Plungers ermöglicht. Als Target wurde eine ^{9}Be Folie verwendet, als Degrader eine ^{181}Ta Folie. Es wurden sowohl Messungen nur mit dem Target durchgeführt als auch solche mit einer Kombination aus Target und Degrader, wobei die Abstände der beiden Folien hierbei 25 mm und 45 mm betrugen. Die dabei aufgenommenen Energiespektren werden mit simulierten Spektren verglichen. Die so erhaltene Lebenszeit beläuft sich auf $\tau_{1/2^+}=420^{+35}_{-32}(\text{stat})^{+34}_{-12}(\text{sys})$ ps, während sich das Verzweigungsverhältnis zu $\text{BR}\left(3/2^+ \rightarrow 1/2^+\right)=(11.7 \pm 1.2)\%$ ergibt. Die Ergebnisse werden verglichen mit Schalenmodellrechnungen mit der effektiven USDB Interaktion sowie Ab-Initio-Rechnungen basierend auf der IM-SRG und der chiralen EFT.

Des Weiteren berichtet diese Arbeit von der Entwicklung eines neuen und bemerkenswert schlichten Verfahrens zum Erstellen einer experimentellen Basis an Referenzsignalen für Compton tracking arrays, wie zum Beispiel GRETINA und AGATA. Diese Basis wird dazu verwendet, die Interaktionspunkte der γ Strahlung innerhalb des Detektorvolumens zu bestimmen. Das Erzeugen einer hochauflösenden Basis für solche Detektorsysteme erweist sich jedoch als ausgesprochen schwierig und ist ein limitierender Faktor für die Positionsauflösung dieser Systeme. Das vorgestellte Verfahren nutzt die Charakteristik der Comptonstreuung zusammen mit den Interaktionen in den umliegenden Detektoren, um die Detektoren in iterativer Weise gegenseitig zu kalibrieren. Damit ist es möglich, eine Selbstkalibrierung der Compton tracking arrays durchzuführen und die Positionsauflösung dieser Detektorsysteme erstmals an ihre intrinsische Grenze zu führen.

Contents

Sometimes, if you pay real close attention to the pebbles you find out about the ocean.

(Terry Pratchett)

1 Introduction

In the spirit of the words of Terry Pratchett, nuclear physics looks at the miniscule building blocks of all that surrounds us, trying to answer questions about the biggest structures we observe. These building blocks are the nuclei, or more precisely the protons and neutrons, which are at the core of all matter. And, while the size of nuclei is of the order of 10^{-15} m, the interaction between their constituents governs the properties of such enormous and exotic systems as stars, supernovae, or neutron stars. For stars, the input from nuclear physics can thereby be described as rather well established. For supernovae and neutron stars, on the other hand, the situation is quite opposite. Be it the neutron-capture cross sections of very neutron-rich isotopes for the r-process in supernovae, or the density of neutron matter in neutron stars, both systems pose numerous questions which nuclear physics struggles to answer. But even the small systems, the nuclei themselves, confront us with puzzles. And nuclear physics answers with a large variety of – sometimes seemingly contradictory – models, pushing state-of-the-art supercomputers to their limits. What is it that makes the interaction between protons and neutrons so difficult?

Fundamentally, the nuclear interaction can be understood as a residual interaction of the strong force between colour polarized nucleons, much like the Van der Waals force [ME11]. As such, quantum chromo dynamics (QCD) presents itself as the natural language to formulate the nuclear interaction. However, at the low energies typical for the nuclear interaction the coupling constant of the strong force is $\alpha \simeq 1$. This makes QCD highly non-perturbative and, thus, difficult to solve. Indeed, lattice QCD can only be used for calculations connected to very limited aspects of the nuclear interaction, e.g., the nucleon-nucleon (NN) scattering lengths [BBOS06] and the charge radius of the proton [Ale17]. The computing requirements thereby severely limit the applicability of QCD for the nuclear interaction, which makes approximations unavoidable.

Despite the intricateness of the nuclear interaction, though, surprisingly simple models are able to describe certain features of nuclei. As a first example, the α decay can be described by an α particle moving freely inside the nucleus and getting deflected at the potential barrier over and over again, until it finally tunnels through the barrier. This model, developed in 1928 [GC28, Gam28], allows to draw a connection between the energy of the α decay and the lifetime of the nucleus, and is still used today as an explanation.

The second example concerns the binding energy of nuclei. While describing the nucleus as a liquid drop [vW35], the binding energy can be parametrized with five terms. The first parameter belongs to the volume term, a_V, originating from the attractive force between nucleons in the bulk of the nucleus. Since not all nucleons are equally surrounded by neighbours, the surface parameter, a_S, reduces the binding energy proportional to the surface area. Furthermore, the repulsive Coulomb force acting on the charged protons reduces the binding energy, giving a_C. The two remaining parameters are due to the asymmetry term, a_A, decreasing the binding energy for an unequal number of protons and neutrons, and the pairing term, δ, increasing or decreasing it for an even or odd number of protons and neutrons. This constitutes the semi-empirical mass formula

$$E_\mathrm{B} = a_\mathrm{V} A - a_\mathrm{S} A^{2/3} - a_\mathrm{C} \frac{Z(Z-1)}{A^{1/3}} - a_\mathrm{A} \frac{(A-2Z)^2}{A} - \delta(A,Z) \tag{1.1}$$

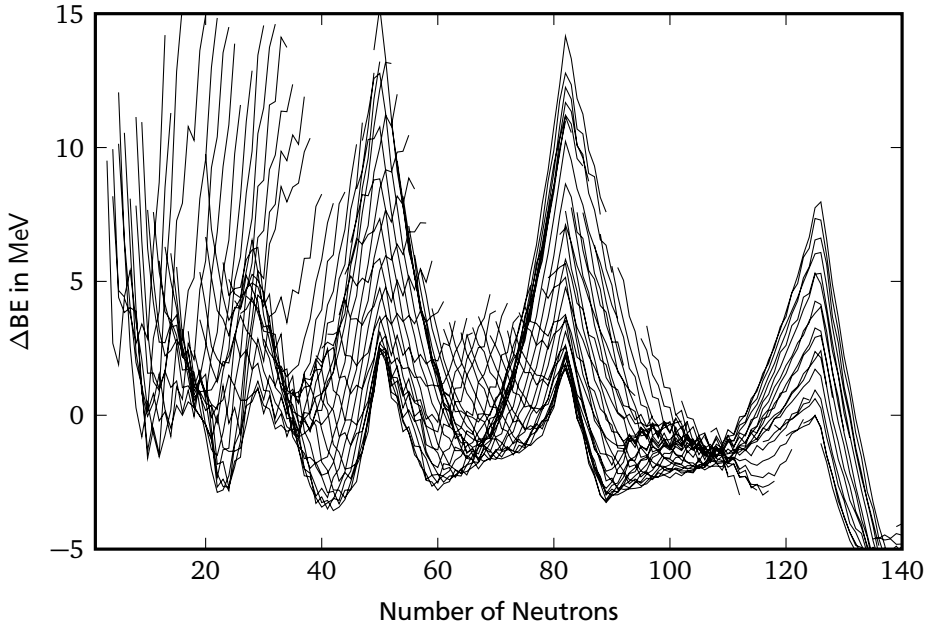

Figure 1.1: Difference ΔBE of the measured binding energies and the expectations from the semi-empirical mass formula. Nuclei with $5<Z<100$ are plotted. The general agreement is within 10 MeV, which, for heavy nuclei, is within 1% of the actual binding energy. The very prominent structure in the data is a signature of the magic numbers.

for a nucleus with A nucleons and Z protons, where the respective constants are determined by a fit to experimental data. Figure 1.1 shows the difference of the measured binding energy to the one determined from the semi-empirical mass formula. For most nuclei, the agreement is within 10 MeV. Especially for heavy nuclei, this is a remarkable accuracy of better than 1%. However, the data shows a very peculiar structure, for which nuclei around, e.g., certain neutron numbers are systematically tighter bound than expected from the liquid drop model. The same behaviour can be seen for protons as well. Such systematics are not unique to the binding energies, but can also be seen for, e.g., the neutron separation energies and the energies of the first excited states. Indeed, these structures are a signature of the magic numbers of nuclei.

The third and final example of a simple model aims at explaining the occurrence of the magic numbers. The nucleus is described as a collection of independently moving nucleons in a common mean field potential. Since the range of the nuclear interaction is short, the shape of this potential should follow the density distribution in the nucleus. A common parametrization of such a potential is given by the Woods-Saxon potential [WS54] as

$$V_{\mathrm{WS}} = \frac{-V_0}{1+\exp\left(\frac{r-R}{a}\right)} \tag{1.2}$$

with the radius of the nucleus R, the depth of the potential V_0, and the diffuseness parameter a. Using this potential to solve the Schrödinger equation produces the energy spectrum shown on the left in Figure 1.2. It correctly reproduces the first few magic numbers as large gaps in the level energies for 2, 8, and 20 nucleons, but fails for larger numbers. The further introduction of a spin-orbit potential [May49, HJS49] removes the degeneracy in total spin J with

$$V_{\mathrm{WS+LS}} = V_{\mathrm{WS}} + V_{\mathrm{LS}}\,\vec{l}\cdot\vec{s}. \tag{1.3}$$

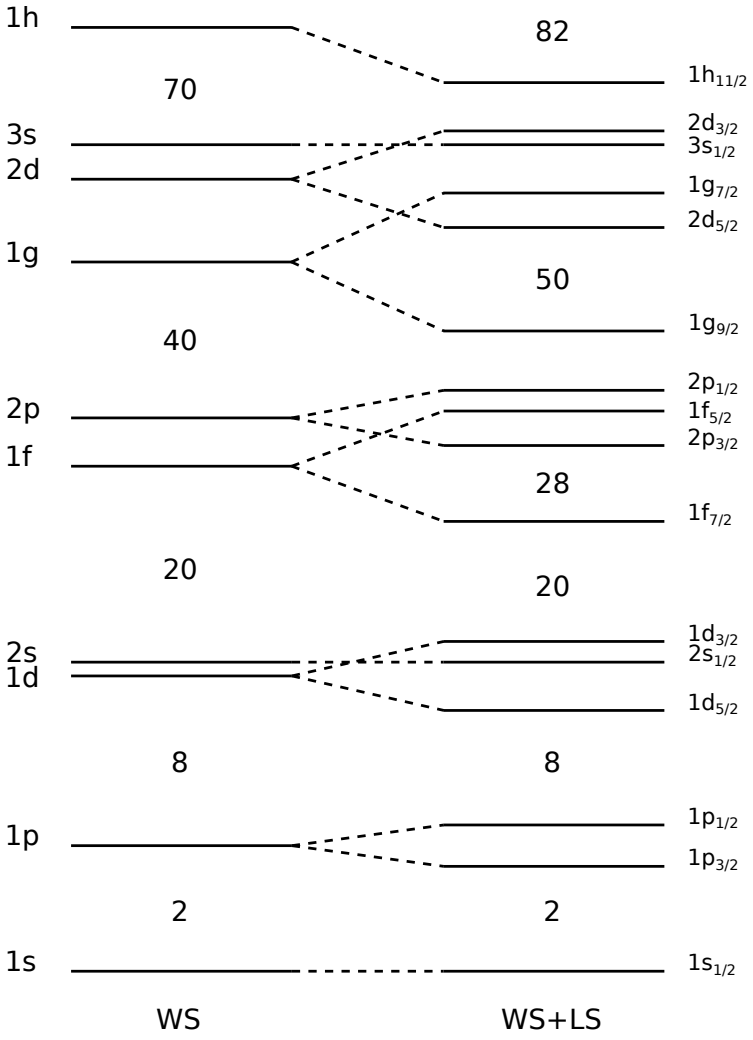

Figure 1.2: Single particle energies for a Woods-Saxon potential (left) and after including a spin-orbit coupling (right). The spin-orbit coupling reduces the energy of orbits with aligned spin and angular momentum, and increases the energy in the opposite case. The resulting gaps in energy reproduce the magic numbers. The sketch is adapted from [Cas01].

As a consequence, the energy of orbits with aligned angular momentum $\vec{l}$ and spin $\vec{s}$ get reduced in energy, while anti-aligned orbits get lifted. For an appropriate strength of the spin-orbit coupling, V_{LS}, this indeed correctly reproduces all magic numbers in stable nuclei, as illustrated on the right in Figure 1.2. Furthermore, the total spin J and the parity π of the ground state of most nuclei can be explained by the consecutive filling of these orbits. The success of this simple model cemented the role of the shell model approach as a basis for the description of the nucleus until today. Ever since, of course, the models have become more refined, extended towards more observables, describing ever more exotic nuclei.

Of those observables, the electromagnetic transition rates, which are directly related to the lifetimes of excited states, will be one focus of this thesis. The isotope investigated for this purpose is ^{21}O, a light, neutron-rich isotope, which only recently became accessible by state-of-the-art no-core shell-model (NCSM) calculations. And as for the theoretical models, where progress goes hand in hand with advancements in computing power, the experimental success is linked to the improvements of research facilities and their detector systems. Various radioactive ion beam facilities provide access to very exotic nuclei, while high resolution and high efficiency detector systems allow for precision measurements of these nuclei. In this context, another focus of this thesis is the development of a calibration method for position sensitive γ-ray detectors, potentially improving the achievable position resolution to the intrinsic limit of such detectors.

As such, this thesis presents two more steps in this century long marathon of understanding the nuclear interaction.

Part I
Self-Calibration of Compton Tracking Arrays

Compton tracking arrays constitute the technological frontier of high-resolution γ-ray spectroscopy, revolutionizing modern nuclear physics experiments. Their principle of operation lies on the precise reconstruction of the three-dimensional γ-ray interaction positions within the detector volume. The most common method to obtain these interaction points in real time is to compare the experimental signals against a reliable library of signals (signal basis) that maps the detector response as a function of the γ-ray interaction position. Obtaining a high-fidelity signal basis, however, remains a big technological challenge, which hinders the optimal operation of these state-of-the-art detector arrays.

This first part of the thesis discusses the development of a novel and notably simple method to generate a reliable, experimental signal basis, published in [HPP18]. The proposed method enables the Compton tracking arrays to perform a self-calibration of their position sensitive response in-situ, opening up the way for reaching their optimum performance for the first time.

2 Basics

This chapter provides an overview of the basics for the self-calibration. It starts with the interaction of γ rays with matter in Section 2.1, providing the basis for the detection of γ rays. Section 2.2 continues with an introduction to semiconductor detectors based on germanium, leading to the recent development of Compton tracking arrays, described in Subsection 2.2.1. After sketching the current techniques for the position calibration of such detector arrays in Subsection 2.2.3, the concept of the self-calibration is discussed in Section 2.3, before Section 2.4 closes this chapter by highlighting a few aspects of the current implementation of the self-calibration.

2.1 Interaction of γ Rays with Matter

With a main focus on γ-ray spectroscopy in this thesis, the interaction of γ radiation with matter is of key importance. Therefore, the following will provide a brief overview of the relevant types of interactions, namely the photoelectric absorption, the pair production, and the Compton scattering. Figure 2.1 shows the energy dependence of the contribution of those interactions to the attenuation of γ radiation. Comprehensive discussions of these and additional processes can be found in [Leo87, Kno89].

Photoelectric Absorption

At low energies of up to a few hundred keV the photoelectric absorption is the dominating interaction. Hereby, the γ-ray photon is absorbed by an atom, transferring all of its energy, and a photoelectron with an energy of

$$E_\mathrm{e} = h\nu - E_\mathrm{b} \tag{2.1}$$

is emitted, where E_b is the binding energy of the electron and ν is the frequency of the absorbed γ ray. The interaction probability thereby increases dramatically with the charge number Z of the atom ($\propto Z^n$ with $4<n<5$) and is largest for tightly bound electrons. The remaining ion regularly produces additional X rays or Auger electrons, which in turn deposit their energy in the surrounding material. With this, the photoelectric absorption marks the end of an interaction sequence for γ rays.

Pair Production

Even though it is already energetically allowed for energies above 1022 keV, the pair production is most relevant at large energies of several MeV. In the Coulomb field of a nucleus, the γ ray is hereby replaced by an electron-positron pair, which equally shares the total γ-ray energy. As charged particles, both will quickly deposit their kinetic energy in the surrounding material followed by the annihilation of the positron with another electron. This annihilation process

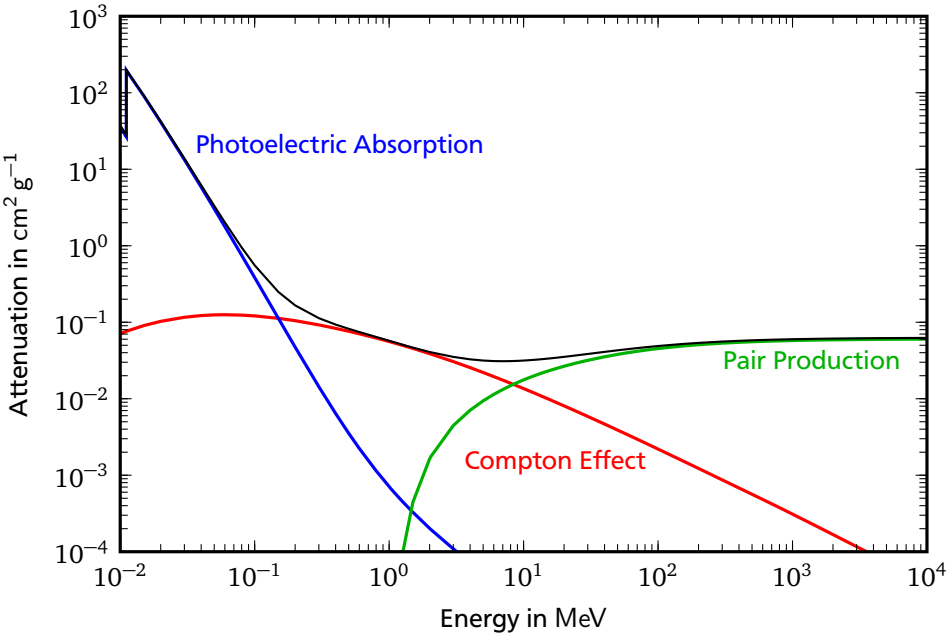

Figure 2.1: Different interaction processes of photons with matter for the case of germanium. Only the most relevant contributions are drawn. At low energies the photoelectric absorption dominates. At intermediate energies the Compton effect is most common, before the pair production takes over at high energies. The attenuation data is taken from [BHS18].

produces two 511 keV γ rays in opposite directions. If one or both of these γ rays escape the detector, the detected energy will be missing these characteristic 511 keV or 1022 keV, producing the so-called single- and double-escape peaks, respectively. Similarly, if the pair production takes place in a non-sensitive volume and only an annihilation γ-ray is detected, it will produce a peak at 511 keV in the energy spectrum.

Compton Scattering

At intermediate energies of a few MeV – and with this most common in nuclear physics measurements – Compton scattering is the primary interaction mechanism. The γ-ray photon is scattered from an electron, changing its momentum and thereby transferring part of its energy to the electron. Assuming that the electron is free and initially at rest, the energy transfer is related to the scattering angle Θ of the γ-ray photon according to

$$\cos\Theta = 1 + \frac{m_e c^2}{E_{inc}} - \frac{m_e c^2}{E_{inc} - E_{dep}}, \tag{2.2}$$

with the electron mass m_e, the energy of the γ ray before the scattering E_{inc}, and the energy transferred to the electron E_{dep}. As can be seen, forward scattering corresponds to small energy transfers, while a 180° scattering results in the maximum energy transfer to the electron. For a single Compton scattering this maximum energy is given by

$$E_{dep,max} = \frac{2E_{inc}^2}{m_e c^2 + 2E_{inc}}. \tag{2.3}$$

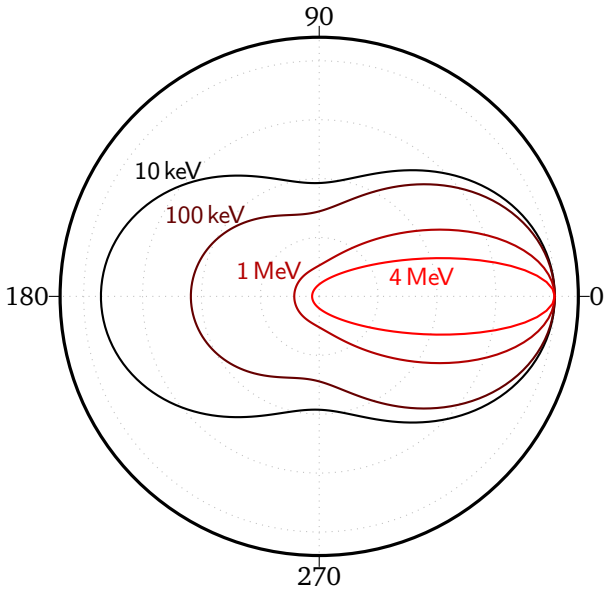

Figure 2.2: Polar plot of the probability to scatter a γ ray of a given energy under a certain angle. For higher energies, forward scattering is strongly enhanced.

All other scattering angles lead to an energy transfer between these two extremes. With this, the Compton scattering produces a characteristic feature in a measured energy spectrum, namely, the Compton continuum up to the Compton edge, which corresponds to the maximum energy transfer in a single Compton scattering. An illustration of the energy spectrum and the Compton continuum can be seen in Figure 2.4.

The differential cross section describing the angular distribution for the Compton scattering from a free electron is given by the Klein-Nishina formula [KN29]

$$\frac{\mathrm{d}\sigma}{\mathrm{d}\Omega} = \frac{1}{2}\left(\frac{\alpha\hbar c}{m_\mathrm{e}c^2}\right)^2 \frac{1}{\left(1+\frac{E}{m_\mathrm{e}c^2}(1-\cos\Theta)\right)^2}\left(1+\cos^2\Theta+\frac{\left(\frac{E}{m_\mathrm{e}c^2}\right)^2(1-\cos\Theta)^2}{1+\frac{E}{m_\mathrm{e}c^2}(1-\cos\Theta)}\right), \tag{2.4}$$

with the fine structure constant α. The resulting scattering probabilities are shown in Figure 2.2. For the relevant energy range of a few hundred keV to a few MeV, forward scattering is significantly enhanced. Since forward scattering also entails a small energy transfer, γ rays in this energy range most likely undergo multiple scatterings, before their energy is low enough for the photoelectric effect to end the interaction sequence.

All of the above is based on the assumption that the γ ray scatters from an unbound electron that is initially at rest. In a real detector this is obviously not the case. The electrons are bound, and as such, have an initial momentum. As a result, the relation of the scattering angle and the detected energy, as described by Equation 2.3 and 2.4, is washed out and only approximative. While this effect is mostly negligible for the experimental determination of the γ-ray energy, it is relevant for methods explicitly utilizing the energy-angle relation, like γ ray tracking and the here presented self-calibration. As such, this effect will be included in the later simulations.

Figure 2.3: Schematic of a section of the Gammasphere array. It shows four HPGe detectors with their surrounding BGO Compton suppression shielding and additional components, like the electronics and the cryogenics. The sketch is taken from [ES08].

2.2 High Purity Germanium Detectors

This section will provide an overview of the functional aspects of germanium based semiconductor detectors. Exhaustive discussions can be found in [LDV03, ES08]. The detection of γ rays utilizes the ionizing character of their interaction with matter to generate an electric signal. In semiconductor detectors, the produced electrons are measured directly. Hereby a p-n configuration is exposed to a reverse bias voltage, which extends the depletion zone in the semiconductor where no free charge carriers are available. The interaction of a γ ray in this depletion zone then produces free charge carriers, and thus leads to a short current, which is proportional to the amount of charge carriers produced, which in turn is proportional to the deposited energy.

The depletion zone thereby defines the sensitive volume of the detector. Maximizing its size is one of the goals in detector development. Germanium thereby has multiple practical advantages, especially for γ-ray spectroscopy. The band gap of germanium (0.7 eV) is significantly smaller than, e.g., for silicon (1.1 eV), which improves the energy resolution. Furthermore, germanium crystals can be produced with very high purity, which is required to allow the depletion zone to grow beyond a few mm with bias voltages of a few kV, hence the name high-purity germanium (HPGe) detectors. Finally, the higher Z of germanium compared to silicon increases the probability for the photoelectric absorption and, thus, increases the efficiency of detecting the full energy of a γ ray. The small band gap, however, requires operation at cryogenic temperatures to limit the leakage current due to the thermal excitation of electrons. With this, energy resolutions of $\approx$0.2% at 1.33 MeV are achieved.

To suppress events in which a γ ray deposits only a part of its energy, HPGe detectors are often surrounded by a bismuth germanium oxide (BGO) Compton suppression shield [NGT85].

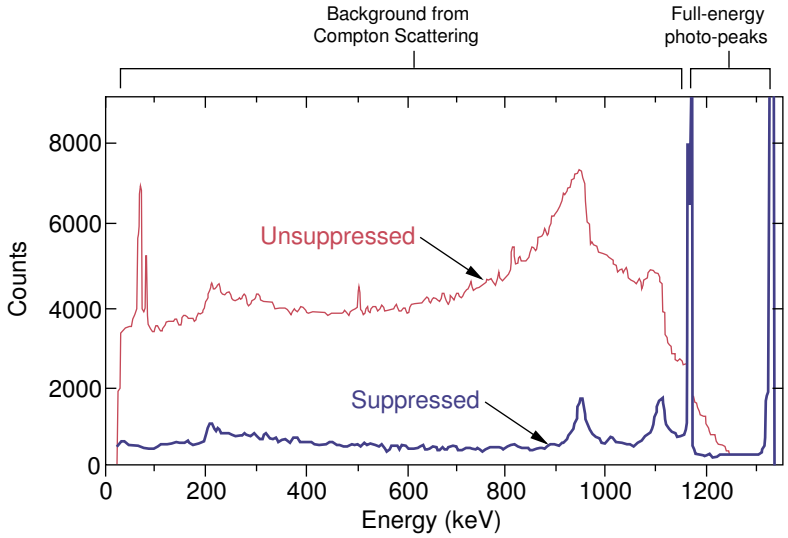

Figure 2.4: Comparison of energy spectra with and without BGO Compton suppression for a ^{60}Co source. The two full-energy peaks can be seen at 1.17 MeV and 1.33 MeV. The suppression significantly reduces the Compton continuum, leaving only two peaks at the Compton edges, which correspond to backward scattering events and therefore do not produce a signal in the BGO. The spectrum is taken from [Gam18].

BGO is a scintillator material which also is capable of detecting γ rays. The BGO suppression builds upon the very high detection efficiency due to the high Z of bismuth and the large density of BGO. The HPGe detector and the BGO shield are then operated in anti-coincidence, such that the signal of the HPGe detector is vetoed if a signal has been detected by the BGO as this implies that the γ ray has left the HPGe detector. The difference of the recorded spectra with and without the Compton suppression is shown in Figure 2.4.

Based on this and motivated by, e.g., the high γ-ray multiplicities from nuclear excited states with large spin – so-called super- and hyperdeformed states – full solid angle detector systems like Gammasphere [Lee90] and Euroball [Sim97] were developed. As an example, a sketch of Gammasphere is shown in Figure 2.3. These detector arrays have full energy efficiencies of $\approx$10% and peak-to-total ratios of $\approx$60% at a γ ray energy of 1.3 MeV.

However, improvements are still possible, since the HPGe detectors cover only around 50% of the full solid angle of these detector arrays, mainly due to the BGO shielding. While it would be possible to replace the BGO shielding with additional HPGe detectors, the need for higher granularities of such detector arrays has led to the development of position sensitive HPGe detectors.

2.2.1 Compton Tracking Arrays

With their superior energy resolution, HPGe detector arrays quickly became a vital tool for nuclear structure investigations. However, depending on the experimental details, the efficiency and intrinsic energy resolution of the detector may not be the limiting factors in a measurement.

For one, large multiplicities can pose problems if multiple γ rays are detected by the same detector, as their energies will be added up. If the full energy was detected for all γ rays, this produces the so-called sum peaks in the energy spectrum. However, if only parts of the energies were detected, the resulting energy is basically arbitrary. In this case, it is no longer possible

to disentangle the different γ-ray energies, which therefore reduces the efficiency. Also, if the isotope of interest is moving at the time of decay, the Doppler shift needs to be taken into account to determine the γ-ray energy. This requires one to know the detection angle as precisely as possible.

Both problems can be addressed by reducing the size of the detector crystals and building the detector array from more detectors. However, this significantly increases the mechanical complexity of the detector system and requires, e.g., additional readout electronics for every detector, which entails substantial cost increases. It becomes clear that simply increasing the number of detectors while reducing their size is not feasible.

Instead, the development of Compton tracking arrays (sCTAs) like GRETA [DLV99, PLM13] and AGATA [Baz04, AAA12] allows to directly measure the interaction position inside the detector volume. This is possible due to an electronic segmentation of the contacts on the detector surface and the digitization of the read-out system. Figure 2.5 shows a sketch of a 36 fold segmented detector. The central rod is used as the anode and the outer surface acts as the cathode. While the sensitive volume is built from a single HPGe crystal, the outer contacts are divided into 36 smaller segments, from which the detected signals are read out separately. If a γ ray deposits energy in the detector, electron-hole pairs are created, which will be separated by the electric field due to the bias voltage. The electrons drift towards the anode, while the holes drift to the cathode. While the central contact registers the full charge, the outer contacts might share the charges. The time dependency and details of how the contacts share the charges depend on the position of the interaction and, therefore, allow to determine this position. Figure 2.6 shows a conceptual illustration of how such signals look like.

The same time window of all signals are thereby combined to a single pulse. The segment in which the interaction took place sees a very strong, saturating signal. In addition, the neighbouring contacts, e.g., share part of the charges, or detect mirror charges. Under ideal conditions, every interaction position provides a unique set of signals in all segments. Indeed, the produced signals at the electrodes are position dependent [LDV03, ES08]. Thus, the details of the pulse shapes of all segments allow to determine the interaction position even within the segment. Practically, the position is determined by comparing the measured signals to a library of expected pulse shapes (signal basis) for different γ-ray interaction positions within the detector.

The detected energies and interaction positions are, however, only the first step in identifying the properties of a detected event. The number of initial γ rays, as well as which interactions belong together and the sequence with which the interactions occurred, need to be derived from the detected energies and positions. The sequence is thereby needed to identify the first interaction and by that the detection angle of the γ ray. For this, various tracking, clustering, and addback algorithms are developed. Compton tracking exploits the properties of Compton scattering and the range of γ radiation in matter, to identify the most probable interaction sequence and assignment. Since this can be computationally expensive for large numbers of interactions, clustering algorithms can be used to preselect subsets of interactions for the tracking. The clustering can, for example, be based on the preference of Compton scattering towards forward angles. In the simplest case, an addback algorithm might just use the geometrical distribution of interactions, e.g., by combining all interactions below a certain distance. For such addback algorithms typically the interaction with the largest energy deposition is assumed to be the first interaction. In any case, the position information is critical for the performance of CTAs.

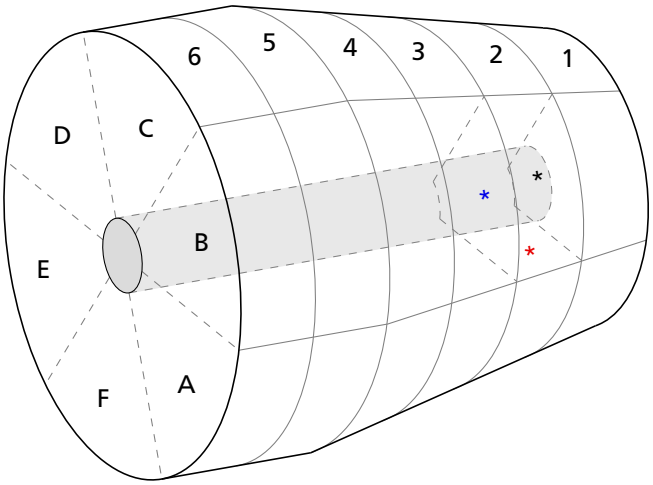

Figure 2.5: Illustration of an electrically segmented germanium detector. The volume of the detector is made of a HPGe single crystal with a central contact, marked in grey. The outer contacts are segmented into six rings and each ring is segmented into six segments, giving a total of 36 segments. Furthermore, three exemplary interactions are drawn in segment B2, for which exemplary signals are illustrated in Figure 2.6.

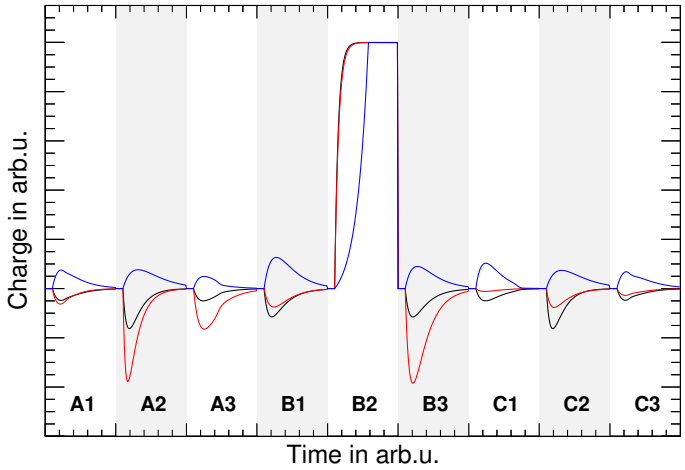

Figure 2.6: Conceptual example of pulse shapes for CTAs illustrating the position sensitivity. The signals of all segments (here examples for nine) are concatenated. Three interactions have taken place at different positions in segment B2, as depicted in Figure 2.5. The blue signal represents an interaction close to the central contact, resulting in a slower signal in B2, while the charges can spread on their way out, giving positive signals in neighbouring segments. The black and the red signals both represent interactions close to the outer surface, indicated by the fast B2 signal and the mirror charges measured in the other segments. Black shows similar signals in all other segments, pointing towards an interaction position in the middle of segment B2. Red shows significantly stronger signals in A2 and B3 compared to the remaining segments, which implies an interaction position in the corner of B2, close to A2 and B3. The details of the pulse shapes can therefore be used to determine the interaction position.

2.2.2 γ-Ray Tracking

In contrast to the tracking of charged particles, for which the large interaction density allows to detect a continuous track through position sensitive detectors like drift chambers, the tracking of γ rays relies on the correct identification of a small number of spatially separated interactions. Therefore, the development of position sensitive γ-ray detectors required the development of dedicated tracking algorithms, specifically designed for the interaction properties of γ rays. Generally, these algorithms can be categorized into two categories, namely, forward and backward tracking algorithms [LMHK04].

Forward tracking algorithms [SDL99] start with a cluster of interactions which are assumed to originate from a single γ ray. The total energy of the γ ray is thus given by the sum of the deposited energy of all interactions in the cluster. With this initial energy and the – assumed to be known – origin of the γ ray a subset of two interactions constituting the first two interactions of the track is searched for. The identification of a suitable interaction pair is done by minimizing a given figure of merit (FOM) function. This process is then continued for any subsequent pair of interactions of the track until all interactions have been assigned, resulting in a most probable interaction sequence for the given cluster.

Backward tracking algorithms [vdMC99] attempt to follow a γ-ray track backwards from the photoelectric effect, which ended the interaction sequence. This exploits the fact that the energy deposition of the final, photoelectric interaction is expected to be in a comparably narrow energy window from 100 keV to 300 keV, independent of the initial γ-ray energy. Starting with such an interaction, its vicinity is searched for a second interaction which is in agreement with the expected range in germanium of a γ ray with an energy known from the supposed final interaction. If one is found, the search is continued, also taking into account the Compton scattering properties until no more suitable interactions are found. Otherwise a different candidate for a photoelectric effect is used to end the track. During this procedure, again, a FOM function is minimized for every potential track.

2.2.3 Position Calibration of Compton Tracking Arrays

The signal basis typically contains a dense grid of predefined points and the associated signals, expected to originate from a γ-ray interaction at these points. Interpolation of the signals between the points of the grid allows for a continuous representation of the entire detector volume. The problem of position reconstruction is then reduced to producing a reliable signal basis and comparing efficiently the measured and expected signals in real time. The methods for generating a signal basis can be categorized into experimental and analytical ones. In practice, a combination of experimental and analytical methods is used to generate the signal bases that are currently in use.

The experimental approaches are based on an exhaustive scan of the crystal volume with dedicated scanning setups, hence in vitro measurements. These methods generate a signal basis from the average of the measured signals for each scanned position, see e.g. [GDPH13]. Such experimental methods have the advantage that the basis is generated without the need of an in-depth understanding and control of all factors that determine the shape of the generated signals. Common drawbacks to all experimental methods are the long acquisition time required to perform the scans for all detector modules and that the experimental conditions, e.g., the

electronics' noise level, could be different between the calibration and the actual experiment. In addition, any uncertainty in the mechanical alignment during the detector scanning can cause systematic deviations in the produced signal basis.

In analytical methods, a calculated signal basis is produced, based on electric field simulations and signal generation algorithms, see e.g. [BBR16]. The steps for such calculations include solving the Poisson equation for the given geometry and applied voltage, taking into account the intrinsic space-charge density, the electron/hole mobility, crystal temperature, and crystal orientation. The accuracy of these estimated signals depends on the precise knowledge of these factors and an accurate modelling of their influence on the shape of the signal. The accurate modelling of the signals also requires detailed knowledge of the passivated and contact thicknesses as well as the actual shape of the charge cloud and its evolution as the charges drift inside the detector. In addition, the calculated signals must account for the signal shaping caused by the front-end electronics and non-negligible cross-talk effects between the detector electronic channels.

A further challenge in producing a reliable signal basis is the possible time-dependent variation of the signal shapes during operation, e.g., due to radiation damage of the detector or electronic noise sources that may vary throughout an experimental campaign.

2.3 Self-Calibration Concept

This section will present a new approach for generating a signal basis, and with that, provide a position calibration for CTAs in a notably simple procedure. The fundamental concept of the self-calibration is to use the surrounding detectors to iteratively calibrate each other, without the need for a dedicated setup. To achieve this, a γ-ray source measurement is done, where the full array is illuminated without collimation, like it would be done for an energy calibration. The emitted γ rays interact with the detector segments and then scatter into neighbouring detector regions, where they interact again. The detected interactions (hits) are then grouped into hit collections, based on the distance between the hits. This is illustrated in Figure 2.7(a). Experimentally, this grouping can be achieved by comparison of the recorded pulse shapes in a similarity check. For simulations, the hit collections are formed using the simulated position of each hit. As a result, all hits within a certain sphere belong to the same hit collection. Hits that happen to lie within multiple hit collections are assigned to all of them, while a hit that cannot be assigned to an existing hit collection defines a new hit collection. The minimum diameter of the hit collection that can be used for grouping hits together reflects the position sensitivity of the detector, i.e., the signal variation between different positions compared to the noise level of the signals. This sensitivity is reported to be of the order of one millimeter or less, depending on the detector region [VKD00, VKL00].

This sorting process provides a set of hit collections, consisting of hits that lie close to each other. The exact positions of the hit collections in the detector volume are not known, but hits from the same hit collection are assumed to share the same position. Furthermore, every hit is part of a track produced by the corresponding interaction sequence. Therefore, these tracks connect all hit collections with each other, while following the energy and angle relations for Compton scattering, as discussed in Section 2.1. From these information alone, the positions of the hit collections can be determined. An illustration of a two dimensional example of how the angle information allows to determine the position of a hit collection is given in Figure 2.7(b). An incorrect position leads to a systematic deviation of the geometric angles from the expected

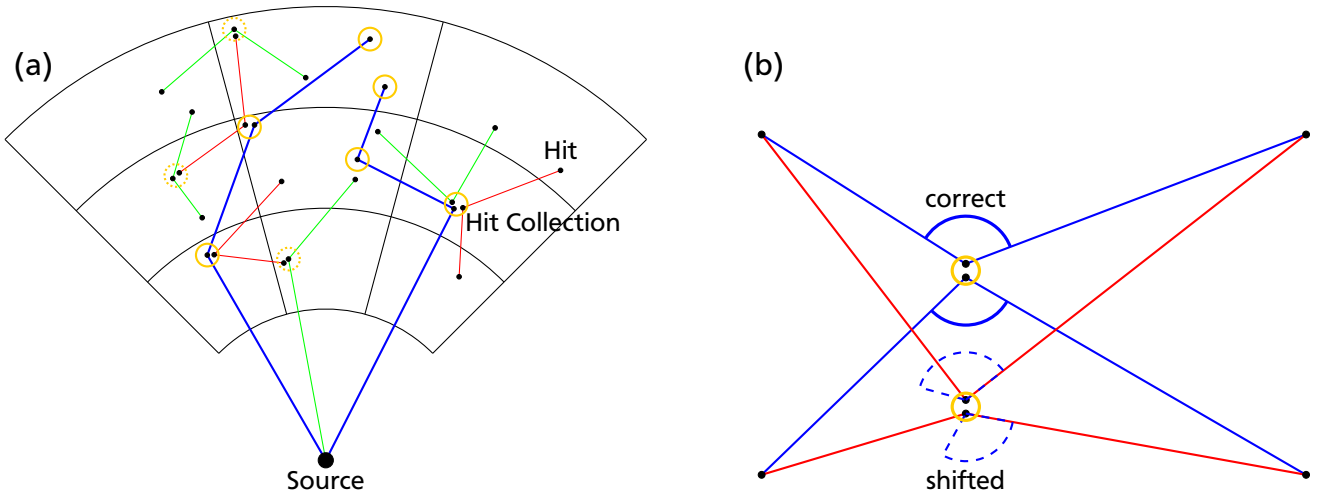

Figure 2.7: (a) Schematic representation of different γ-ray tracks in the detector volume and the grouping of their hits (black dots) into hit collections (yellow circles). Groups of hits from different γ-ray tracks form hit collections. Two exemplary tracks (blue) are shown. Their hit collections are connected to others by additional tracks, ultimately, forming a linked network of hit collections. (b) Illustration of how the angle information allows to determine the hit collection position. A shift of the hit collection position leads to a systematic deviation of the geometric angles from the expected Compton angles (dashed blue). Only the correct position matches the angles for all tracks of a hit collection.

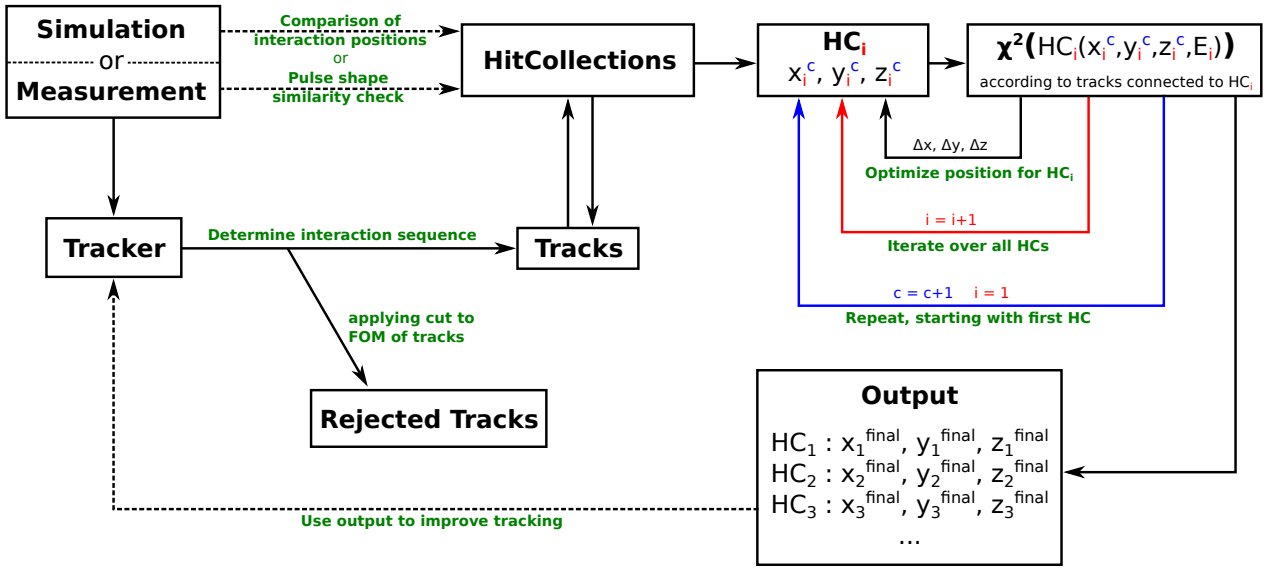

Figure 2.8: The data used as input is either generated by simulation or by measurement. From this data the hit collections are generated by comparing the simulated interaction positions or by performing a pulse shape similarity check, respectively. In addition, a tracking algorithm determines the most probable interaction sequence. The so constructed tracks connect the hit collections with each other. If needed, applying a cut to the figure of merit (FOM) of the tracks can increase the fraction of correct tracks. Now a minimization algorithm is used to subsequently optimize the position of each hit collection i with respect to all other hit collections by taking into account the track information. Once every hit collection position has been optimized, the procedure is repeated, starting again with the first hit collection. This is done repeatedly with every iteration c until a certain level of convergence, e.g., defined by the change in position between subsequent iterations, is reached. At this point, the tracking can be repeated using the output of the position minimization to improve the tracking.

Compton angles according to Equation 2.2, with a unique solution at the real position that minimizes the deviation. Assuming an isotropic spatial distribution of the tracks, this easily translates to a three dimensional case and allows to determine the hit collection position inside the detector volume.

A flowchart of the self-calibration is given in Figure 2.8. As described above, the hit collections are populated either from simulated or measured data. Furthermore, a tracker is used to determine the interaction sequences and some tracks are rejected if the tracking result is not reliable enough. However, in addition to the energy of the γ ray, the tracking requires the interaction positions, yet, without using any other calibration technique, the only position information initially available for a hit collection is the position of the segment in which the interaction took place. Therefore, a coarse initial position is assigned to the hit collections, e.g., at the centre of the corresponding segment, which is also used for the tracking. After the tracking has determined the interaction sequences, the geometrical angles obtained for all tracks are compared to the respective Compton angles, following Equation 2.2, where the initial energy is known from the source energy. Starting with one hit collection, the positions of all hit collections are adjusted iteratively, such that the difference between the geometrical and Compton angles are minimized. Although the positions were only roughly known at the beginning, the large number and spatial

distribution of the hit collections allow the minimization to obtain a position closer to the real position. After the position of every hit collection has been optimized once, the first iteration c is completed, and the procedure starts again with the first hit collection. With each iteration, the hit collection positions converge towards their real positions, which are evenly distributed throughout the detector volume. This is continued until a given condition is met and the loop is stopped, e.g., a maximum number of iterations c is reached, or the changes of the hit collection positions are below a certain threshold. The resulting positions of the hit collections can then be used as an input for the tracker, improving its reliability. This process can be repeated as a whole, until the results converge. With this, a signal basis can be produced that inherently incorporates the mechanical and electronical details of the detector array. The position resolution of the detector is then a convolution of the fidelity and the accuracy of the signal basis.

It is noted that a global position optimization of all hit collections simultaneously would give the results after a single iteration. However, this is accompanied by severe computational challenges, which have been circumvented by the iterative approach.

2.4 Implementation

While the simulations for the input data are done with Geant4 [AAA03], the implementation of the self-calibration makes use of the functionalities of ROOT [BR96]. The most relevant limitation for the implementation (at least on the available hardware) was memory. As such, various optimizations were made to reduce the memory footprint of the program. The most relevant of these is the subdivision of tracks into paths. Paths are sets of three consecutive hits from a track, which is the smallest set which still allows to compare the geometrical angle to the Compton angle. While this introduces some overhead for storing a full track as paths, it allows to selectively store only parts of a track. This is of interest because the hit density is much higher for the inner part of the detector, as can be seen in Figure 2.9. Thus, using paths allows to omit the inner parts of a track, to achieve a more uniform hit density throughout the detector volume and with this reduce the memory requirements. However, since paths are an implementation specific construct and to keep the nomenclature simple, the later discussion will be held in terms of tracks, even though paths have been utilized.

The central object of the implementation is the hit collection. A hit collection stores its position information and pointers to all paths it is part of. Neglecting most of the overhead, the minimal size of a hit collection in memory is, depending on the number of paths n, given by

- the x, y, and z positions of the hit collection: $3 \times 4\,\mathrm{B}$ (float),
- the pointer to the vector of the paths: $8\,\mathrm{B}$,
- the content of the vector: $n \cdot 8\,\mathrm{B}$.

As can be seen, this effectively results in $n \cdot 8\,\mathrm{B}$ of memory for any significant number of paths.

Each path in turn stores the incoming and deposited energy for the second hit, as well as pointers to the hit collections of all three hits. Thus, a path requires memory for

- the incoming and deposited energy: $2 \cdot 4\,\mathrm{B}$ (float),
- the pointers to the vectors of the hit collections: $3 \cdot 8\,\mathrm{B}$,
- the content of the vectors: $5 \cdot 8\,\mathrm{B}$.

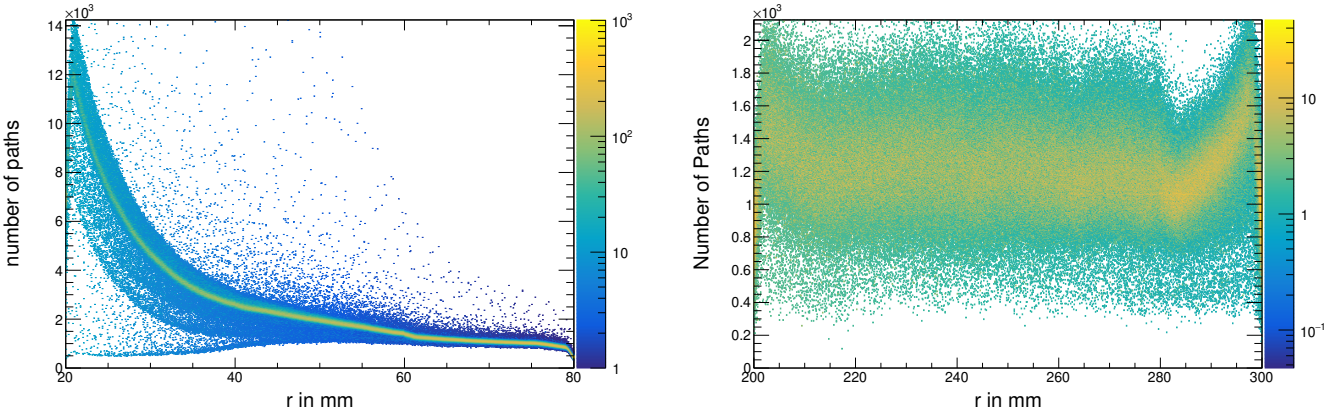

Figure 2.9: Number of paths in the hit collections depending on the position of the hit collection in the detector for a small detector geometry without omission of paths (left) and for a realistically sized geometry after omission (right). The omission leads to a much more even distribution throughout the detector volume and thus reduces the memory requirements.

This assumes that on average two out of three hits belong to two hit collections, while the third hit belongs to one hit collection. With this, the average memory required for a path is about 72 B.

Assuming a data set of 1.5 million hit collections with 500 paths each, where each path is used for three hit collections, gives a minimal size in memory of 24 GB. If, on the other hand, each path is only used by a single hit collection, 60 GB are required. A realistic data set will lie somewhere between these two extremes. Furthermore, the implementation includes additional debugging information like the real positions of the hit collections to analyse the results and the overhead for the management of the vectors, which increases the memory requirements by about a factor of 4. In fact, the biggest data sets used for the later analysis required approximately 300 GB of memory.

The position optimization is then done in a loop over all hit collections. The function used for the optimization is again a loop over all paths of the respective hit collection, calculating the sum of the absolute values of all angle differences. There is no ordering to how the paths connect hit collections and, therefore, it is not possible, to sort the paths or hit collections for an efficient access patterns. Indeed, the paths connected to one hit collection are randomly distributed throughout the memory. Similarly, an optimization by pre-caching is difficult, if not impossible.

For an exemplary case, the position optimization of a single hit collection takes approximately 20 ms, while requiring access to 500 paths and the positions of 1000 other hit collections. The size of these required data is approximately 50 kB, distributed over 200 GB in blocks of less than 100 B. While this requires a bandwidth of only 2.5 MB s^{-1}, the random access time of less than 10 μs requires a storage device with over 100 000 IOPS. This is easily achieved with random-access memory, which today commonly has random access times of 10 ns, and as such, provides the capacity for supplying several hundred threads in parallel. But, it requires all data to be held in memory the whole runtime of the self-calibration.

Furthermore, the minimizer function that calculates the estimator f, which is used for the position optimization, is a critical component of the implementation. Even though more elaborate

functions for tracking algorithms where investigated with regards to the speed of convergence and stability of the minimization, finally, the simplest function was used:

$$f = \frac{1}{N} \sum_{i=0}^{N} \left| \Theta_{\mathrm{G},i} - \Theta_{\mathrm{C},i} \right|, \tag{2.5}$$

summing over the geometrical angles Θ_{G} and the Compton angles Θ_{C} for all of the N paths of the current hit collection. Because this function has to be called a few hundred to thousand times by the minimizer to optimize the position of a single hit collection, it is called a few billion times for every iteration and is among the largest contributors to the function calls of the program. As such, the introduction of more elaborate functions leads to a significant increase of the required computation time and, thus, runtime of the self-calibration.

3 Proof of Concept

To investigate the feasibility of the self-calibration concept, a single-threaded version was developed and its performance for small geometries and controlled conditions was tested. The simulated detector geometries are hollow spheres with an inner radius of 20 mm and outer radii of 50 mm and 80 mm. A γ-ray point source with an energy of 2 MeV is placed in the centre of the spheres. This chapter will summarize the results of these first tests and the derived systematics. If not specified otherwise, the self-calibrations have been performed, using exactly 500 tracks for the minimization of every hit collection, even if more were available.

3.1 Ideal Conditions

To check the validity of the code, the simulations were done with the Geant4 physics list `emstandard`, for which the Compton scattering strictly follows the description by Klein-Nishina, as discussed in Section 2.1. Based on these simulations, the self-calibration is performed for various setups and initial conditions.

Taking the actual simulated energy depositions to calculate the Compton angle, i.e., without an additional energy resolution, and starting the self-calibration with the real positions of the hit collections confirms that the code is reliable and that the position minimization is stable. The resulting root mean square deviation (RMSD) of the radial coordinate from the initial – and therefore real – positions for a hit collection diameter of 1 mm is less than 0.1 mm and can be even smaller for larger statistics, i.e., more simulated tracks used for the self-calibration. However, especially for data where only a part of the geometry was illuminated, it can be observed that hit collections are pushed apart. This is an intrinsic tendency of the concept, though it can be compensated, as will be discussed in Section 3.3. To limit this effect for the simulations discussed in this chapter, a cut on the minimum distance between consecutive hits of 19 mm is applied, which is approximately equivalent to requiring the hits to be from separate segments in GRETA or AGATA.

After the self-calibration has proved to be stable at the real positions, the next step is to move the initial positions of the hit collections away from their real positions. Initially this was done by applying a Gaussian resolution to the positions, and, after this was confirmed to converge, the initial positions are set to be the centres of the segments to which the hit collections belong. The segmentation is thereby retroactively used for the determination of the initial position, as it is not part of the simulated geometry. In addition, the hit collections are forced to stay within the simulated detector volume.

The result for this test is illustrated in Figure 3.1 for the radial coordinate of the hit collections. It shows the difference of the determined position r and the real position R in dependence of R. As can be seen, the result shows a systematic, linear correlation of the difference and the real position, indicative of the resulting sphere being shrunk in comparison to the real sphere. This is a remainder of a systematic offset in the initial conditions and will be further discussed Section 3.3. It can be corrected for by scaling the size after the self-calibration, such that it matches the geometric size. Besides the linear correlation, however, the results are very robust,

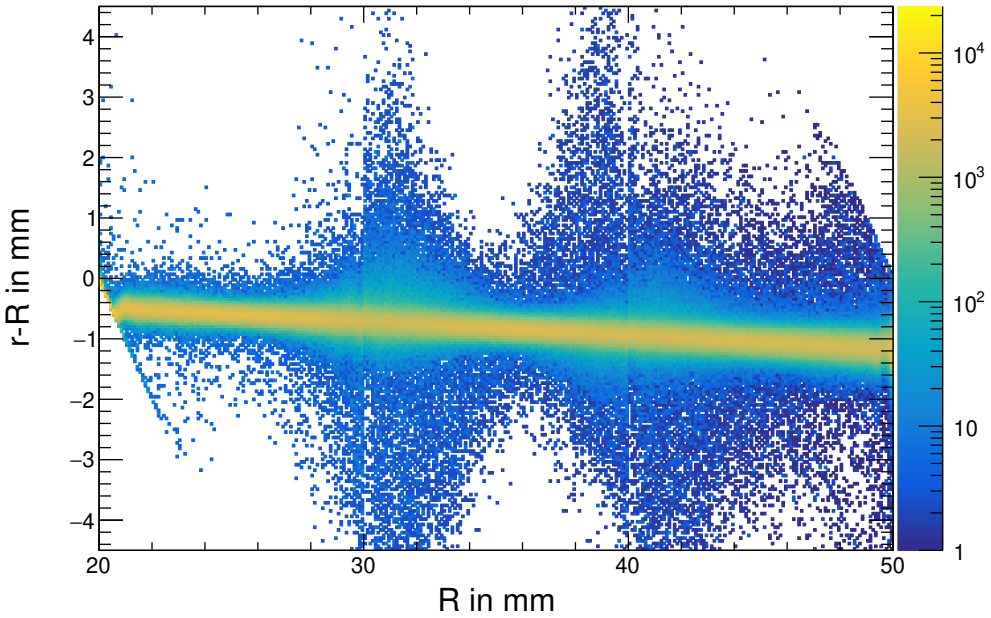

Figure 3.1: Result of the self-calibration after five iterations for ideal conditions, i.e., no additional energy resolution and Compton scattering assuming free electrons. The centres of the segments were used as initial positions of the hit collections. The plot shows the difference of the self-calibrated radial coordinate r and the real coordinate R plotted over R. The linear correlation of the difference and R is a remainder of a systematic offset in the initial conditions.

converging quickly to $\mathrm{RMSD_r}$ values below 0.25 mm, which is less than the intrinsic $\mathrm{RMSD_r}$ of $\frac{1\,\mathrm{mm}}{\sqrt{12}}$=0.29 mm due to the discretization into hit collections with a diameter of 1 mm.

3.2 Realistic Physics

With the self-calibration working under ideal conditions, the first step towards a more realistic application is done by changing the physics list used for the simulations to `emstandard_opt4`. In this physics list, the Doppler broadening and the atomic deexcitation is included in the simulation for the Compton scattering, therefore taking into account that the electrons are bound and not at rest. This is the first step away from the exact fulfilment of the energy-angle relation as described by Klein-Nishina in Equation 2.4. Using the real positions as initial condition, the self-calibration again proves to be stable, resulting in an $\mathrm{RMSD_r}$ of 0.2 mm. Similarly, the self-calibration converged when using the centres of the segments, resulting in an $\mathrm{RMSD_r}$ of 0.3 mm after 10 iterations.

Afterwards, the influence of a finite energy resolution on the self-calibration was investigated. At this stage, a Gaussian resolution with a fixed width is applied to the energy of every interaction. A summary of the results is shown in Figure 3.2. For an energy resolution of σ=2 keV the resulting $\mathrm{RMSD_r}$ was 0.36 mm. Even for an unreasonably large energy resolution of σ=5 keV, the self-calibration continued to converge and the results were only slightly deteriorated, with an $\mathrm{RMSD_r}$ of 0.51 mm. An unexpected finding in this context was that, while the additional energy resolution deteriorates the final result, a small energy resolution could increase the speed of convergence. Though not fully understood, this is attributed to the energy resolution smoothing

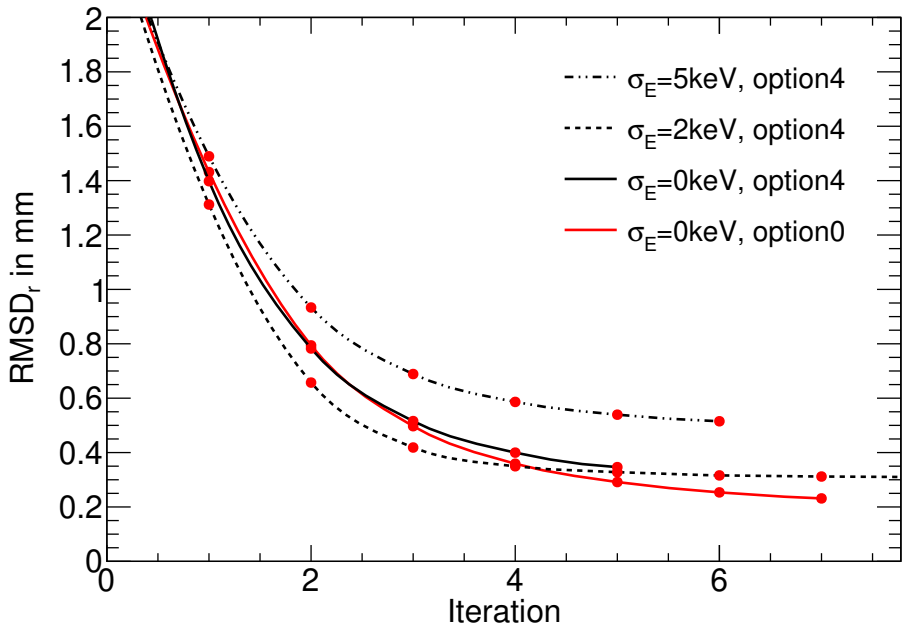

Figure 3.2: Influence of the energy resolution and Doppler broadening on the self-calibration. The plots show the RMSD$_r$ of the radial coordinate of the hit collections for every iteration. The hit collections have a diameter of 1 mm and the initial positions are the centres of the segments. For ideal conditions, without energy resolution and no Doppler broadening (option0), the best RMSD$_r$ values are expected and seen. However, introducing the more accurate model of the Compton scattering (option4) and an energy resolution only slightly deteriorates the results. In fact, a minor improvement of the speed of convergence can be seen for small energy resolutions.

the minimization function and thereby reducing the likelihood of a hit collection being trapped in a temporary, local minimum.

Similar tests were performed to investigate the influence of different initial conditions, the estimator functions used for the position minimization, the diameter of the hit collections, and the influence of the statistics. While some of the found systematics are summarized in following section, the influence of the hit collection diameter and the statistics are discussed in the context of the realistic test case in Section 4.2. In total, the self-calibration proved remarkably stable and reliable for all conditions.

3.3 Systematics

During the first tests of the self-calibration, some systematics were observed which consistently influenced the final results. For one, the positions found by the self-calibration often represented a scaled or rotated version of the initial geometry, manifesting as systematic offsets in the radial or angular components of the hit collection positions. In other cases, hit collections close to the surface of the detector or close to regions of high interaction density showed systematic offsets pointing away from such regions. Both effects can be explained by geometrical considerations presented in the following.

Symmetries

Since the self-calibration relies on the angular information to determine the hit collection positions, it immediately becomes evident that a systematic offset which preserves all angles cannot be recovered. Examples of such offsets are, e.g., scaling the detector geometry or rotating the detector around an axis through the source position. A scaling of the detector geometry can be prevented by forcing the hit collection positions to stay within the detector geometry. For a spherical detector this still allows to rotate the geometry, which can be prevented by introducing a segmentation by which the hit collections are constrained. While this prevents arbitrary movement along such lines of symmetry, the recovery speed of such systematic offsets in the initial conditions will be very slow. This is because only the hit collections which are explicitly limited by the segmentation will produce a contribution which reduces the offset, while the bulk of the hit collections will be placed at a temporary, local minimum with respect to their surrounding, thus, preventing fast changes.

One possible origin of such a systematic offset is the usage of the centres of the segments as the initial positions for the hit collections. Since the amount of hit collections at a given radius scales with the surface area of the respective sphere, there are less hit collections at smaller radii. For a segment with thickness d, the ratio of the inner and outer surface is given by

$$\frac{A_{\text{out}}}{A_{\text{in}}} = \frac{r_{\text{out}}^2}{r_{\text{in}}^2} = \frac{(r_{\text{in}} + d)^2}{r_{\text{in}}^2} = 1 + \frac{d^2}{r_{\text{in}}^2} + 2\frac{d}{r_{\text{in}}}. \tag{3.1}$$

Since this ratio is – unsurprisingly – always larger than 1, moving all hit collections to the centre of a segment moves more hit collections inwards than outwards. The offset thereby increases for larger segments (d), while it is reduced for larger detector geometries (r_{in}). While this offset can be influenced or even fully negated by adjusting the initial conditions, its importance is significantly reduced for geometries with realistic sizes.

Separation Pressure

The self-calibration exhibited the tendency to increase the separation of hit collections under certain conditions. This was the case, for example, for partial illuminations of the detector geometry and very anisotropic distributions of tracks assigned to the hit collections. This effect is caused by the incorrect positions of the surrounding hit collections used for the position optimization. Figure 3.3 illustrates how the position resolution leads to an effective pressure between close hit collections. If the distance between two hit collections is of the same order as the position resolution, the geometrical angle due to the resolution will significantly differ from the Compton angle. Increasing the distance between the two hit collections can – on average – reduce this mismatch and will thus be preferred by the self-calibration.

This effect can be reduced by requiring a minimum distance between two interactions or by using a sufficient number of tracks, which are distributed spatially isotropic around the hit collections. Such an isotropic distribution requires, e.g., to omit some parts of the tracks on the inside of the detector, since the interaction density on the inside is significantly higher than on the outside. However, at the edge of the detector geometry an isotropic distribution is unachievable, though, restricting the hit collections to the physical detector volume mitigates this surface effect.

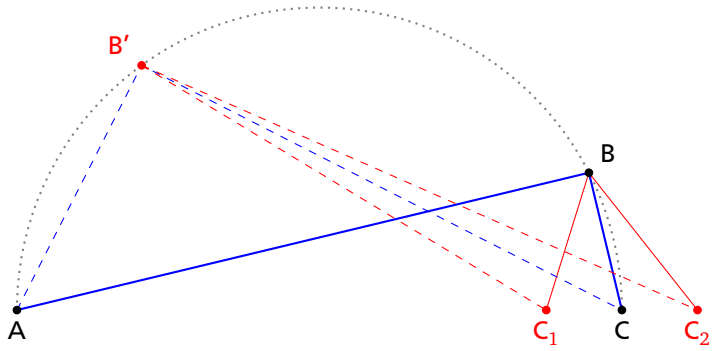

Figure 3.3: Example case illustrating the tendency of the self-calibration to push hits apart. A track (blue) has the real hit positions A, B, and C. The position of B is to be determined from the scattering angle, while A and C are fixed. There exists an arc (dotted) for which every point fulfils the required angle relation, which follows from the inscribed angle theorem. By introducing a position resolution, and thus shifting point C to C_1 or C_2, positions on the arc further away from C show – on average – a smaller angle mismatch than the real position or positions closer to C. This effect is less pronounced for larger numbers of tracks and an isotropic spatial distribution of those tracks.

4 Realistic Test Case

With the implementation of a multi-threaded version of the self-calibration and optimizations to the memory management and requirements, the code is able to handle geometries with realistic sizes on reasonable time scales. The input data for the self-calibration has been obtained from a simulation of a cut of a hollow sphere with an inner radius of 200 mm and an outer radius of 300 mm, as depicted in Figure 4.1. A γ-ray point source with an energy of 2 MeV was placed in the centre of the sphere, for a total of 5×10^9 γ rays directed at the detector. For the self-calibration, the geometry is segmented into 5 radial segments, 4 segments in polar direction, and 4, 12, 16, and 24 segments in azimuthal direction, respectively, giving segments of approximately equal size. The simulations include the Doppler broadening and the atomic deexcitation (option4). In addition, the detected energy depositions have an energy dependant Gaussian resolution typical for that of a real HPGe detector

$$\sigma_E = \sqrt{n + aE}, \tag{4.1}$$

with $n = 1\,\mathrm{keV}^2$ and $a = 3 \times 10^{-3}\,\mathrm{keV}$. In a measurement, interactions that take place too close to each other would not be resolved as separate hits. To account for this, simulated interactions that are separated by less than 2 mm are merged into one hit. The interaction sequence is assumed to be unknown. Thus, a tracker is used to determine the most probable interaction sequence, which is then used by the self-calibration.

The tracking results are thereby discussed in Section 4.1. Afterwards, the results of the self-calibration with the aforementioned, simulation data is presented in Section 4.2. These results mainly focus on hit collections with a diameter of 5 mm, while finally presenting results for a long self-calibration for hit collections with a diameter of 3 mm.

4.1 Tracking

In a measurement, the interaction sequence of a track is unknown and has to be determined from the measured positions and energy depositions. Even under ideal conditions some tracks will lead to ambiguous results and the correct interaction sequence cannot be determined. Especially with the assumption of not having a position calibration yet, the tracking is expected to have a significant fraction of wrong tracks.

Thus a very simple tracker was implemented to provide input data with a reasonable fraction of wrong tracks. The FOM is calculated as

$$\mathrm{FOM} = \sum_i \exp\left(40 \times \left|\cos\theta_{i,\mathrm{C}} - \cos\theta_{i,\mathrm{G}}\right|\right) \tag{4.2}$$

with the geometrical scattering angle θ_G and the angle derived from the deposited energy θ_C for every interaction i. The factor of 40 is thereby included for technical reasons to avoid problems with the machine accuracy. This value is calculated for all permutations and the permutation

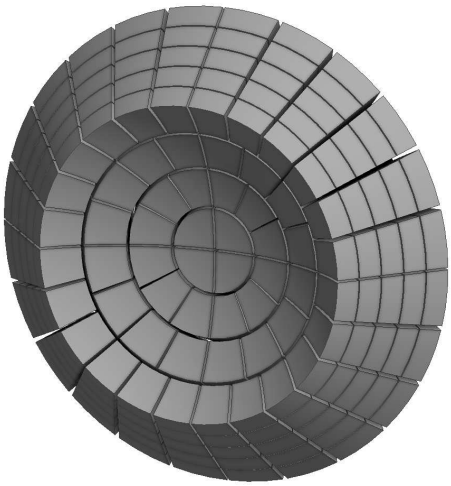

Figure 4.1: Illustration of the simulated detector geometry with a realistic size. It is a cut of a hollow sphere with an inner radius of 200 mm and an outer radius of 300 mm, covering an angular range of 45 ° in polar direction and the full 360 ° in azimuthal direction and a solid angle of 0.586 π sr. The geometry is segmented into 5 radial segments, 4 segments in the polar direction, and 4, 12, 16, and 24 segments in the azimuthal direction, respectively. The simulated geometry does not contain gaps to separate the segments, instead, they are only displayed for the visualization.

with the minimum FOM is assumed to be correct. Since the source energy, and with this the incident energy of the γ ray, is well known, the tracker uses forward tracking. As can be seen, the tracker is based only on the energy-angle relation, thus, not taking into account information on, e.g., the mean free path or the scattering angle probabilities. Indeed, the tracker is by no means optimized, as its main purpose is to produce tracks with reasonably wrong interaction sequences. As such, it is noted that for a real application the tracker and its results can be significantly improved.

The results of this simple tracker are summarized in Figure 4.2. When using the centres of the segments as initial positions for the hit collections, the tracker finds the correct interaction sequence for 33% of the tracks. For these initial conditions, the FOM exhibits peak structures, which are caused by the discretization of placing the hit collections in the centres of the segments, and mostly correlate with scattering angles of approximately 90°. In addition, the FOM of tracks for which interactions were separated by less than 2 mm and, thus, have been merged into a single hit is shown. Since this happens almost exclusively for consecutive interactions, a sensible definition of a correct sequence is still possible, even if interactions have been merged. In general, the behaviour of the FOM for these merged tracks is similar to the FOM of the wrong tracks.

The FOM allows to further improve the reliability of the tracking by applying cuts. The FOM of the best sequence (FOM_1) shows that for smaller values the ratio of correct to wrong sequences is improved. Similarly, the ratio of the FOMs of the best and second best sequence ($\mathrm{FOM}_1/\mathrm{FOM}_2$) provides an improved ratio of correct to wrong sequences for smaller values. Thus, by using the cuts

$$\log(\mathrm{FOM}_1) < 30 \tag{4.3}$$

$$\log(\mathrm{FOM}_1/\mathrm{FOM}_2) < -40 \tag{4.4}$$

the fraction of correct sequences can be improved from 33% to 83%, while reducing the total number of correct tracks by only about 50%. The remaining tracks (including the 17% wrong tracks) are then the first data set used as input for the self-calibration.

Later, the output of the self-calibration was used to re-track the simulation data. As can be seen, the peak structures due to the previous discretization have disappeared and the sequence is correct for 69% of the tracks. Again, cuts can be applied. With

$$\log(\mathrm{FOM}_1) < 20 \tag{4.5}$$

$$\log(\mathrm{FOM}_1/\mathrm{FOM}_2) < -5 \tag{4.6}$$

the fraction of correct tracks is improved to 88%, while losing less than 25% of the correct tracks.

The results so far were obtained under the assumption that interactions which are separated by more than 2 mm can be identified as being separate. Figure 4.3 shows the results for the tracking if all interactions in the same segment are merged into one hit. The fraction of correct tracks is reduced to 25%, yet, the basic structures are unchanged. Again, the tracks for which interactions have been merged follow the general behaviour of the wrong tracks. However, since in this case merged interactions are not necessarily consecutive, the definition of a correct sequence for such tracks no longer makes sense and, thus, all merged tracks are defined as wrong. Similar to the case of the wrong tracks, applying cuts to the FOM allows to suppress merged tracks.

4.2 Results

The tracked simulation data discussed before is now used as input for the self-calibration. For the first self-calibration, the data has been tracked using the centres of the segments and interactions within 2 mm have been merged. The first cuts (c.f. Equation 4.3 and 4.4) have been applied to the FOM, resulting in approximately 17% wrong tracks. The diameter of the hit collections is 5 mm and with this the number of tracks ranges between 1000 and 3000 tracks per hit collection. While the influence of the diameter will be discussed later, the choice of 5 mm presents a compromise between the computation time, the fidelity of the basis, and the simulated interaction density. Initially the hit collections are positioned in the centres of the segments. To evaluate the results of the self-calibration, the obtained positions of the hit collections are compared to their real positions from the simulation. Figure 4.4 shows the results of the self-calibration.

After the first iteration, the hit collections are spread throughout the segments. The distribution of the hit collections clearly shows the segmentation of the detector, since hit collections get pushed against the borders of the segments. For the same reason, the difference Δr of the radii of the self-calibrated position r and the real position R shows a peak at 0, because all hit collections whose real position is at the border of a segment get pushed against it. The triangular structures, in which no hit collections are found, are also an artefact due to the segmentation. Since hit collections cannot be moved further in- or outwards than to the borders of their segments, Δr can only be as big as the distance to the respective border.

With additional iterations, the hit collections are distributed throughout the volume more evenly and the difference of the self-calibrated position and the real position becomes smaller. However, for larger R the hit collections are slightly shifted inwards, giving $\Delta r < 0$. Thus, the Δr over R graph is slightly tilted within each segment and also tilted over the whole detector. This correlation is a remainder of the initial conditions, since for geometrical reasons slightly more

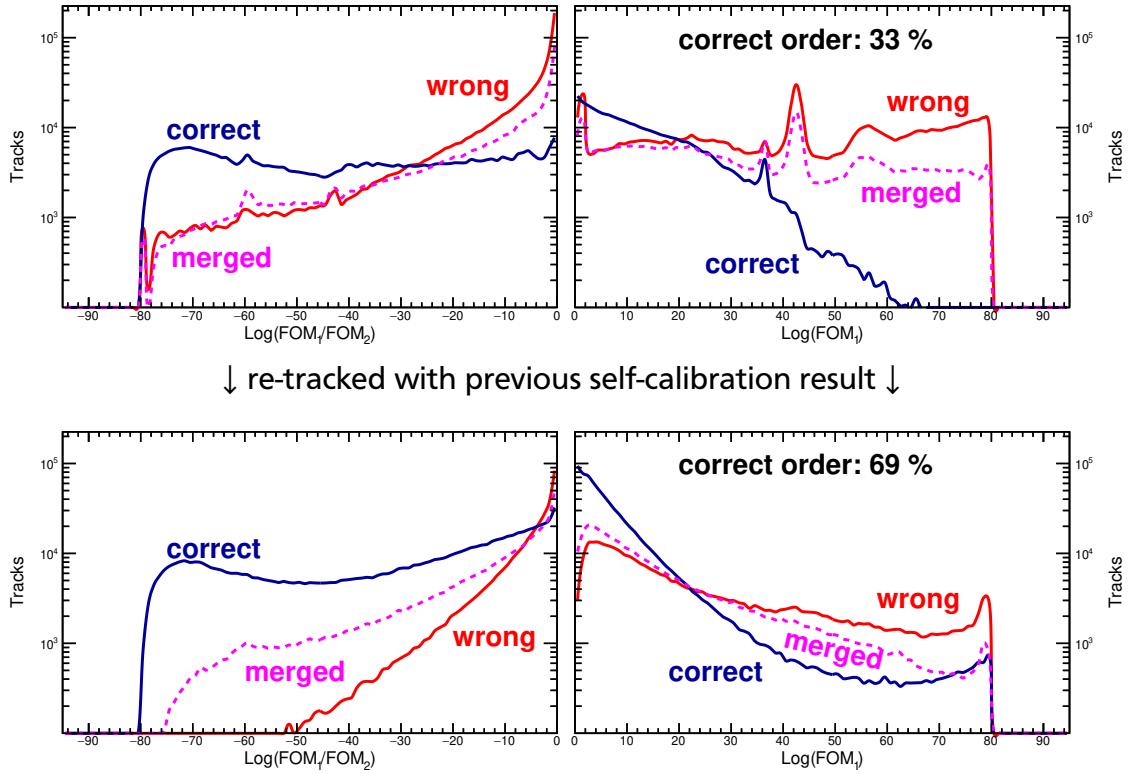

Figure 4.2: Results of the tracker using centres of the segments as initial conditions (top) and using the results of the first self-calibration procedure (bottom). The right graphs show the abundance of tracks with a given FOM for the best interaction sequence (FOM_1). The left graphs show the ratio of the best to the second best sequence (FOM_1/FOM_2). They are shown separately for tracks for which the interaction sequence has been determined correctly or not and for which interactions have been merged into a single hit. For small values of FOM_1 and FOM_1/FOM_2, the sequences are predominantly correct. Thus, applying a cut allows to significantly improve the fraction of correctly reconstructed tracks. The peak structures in the top right plot are a result of the discretization induced by putting all hit collections into the centres of segments. The structures disappear when different initial conditions are used for the positions of the hit collections, as shown on the re-tracked plot (bottom right).

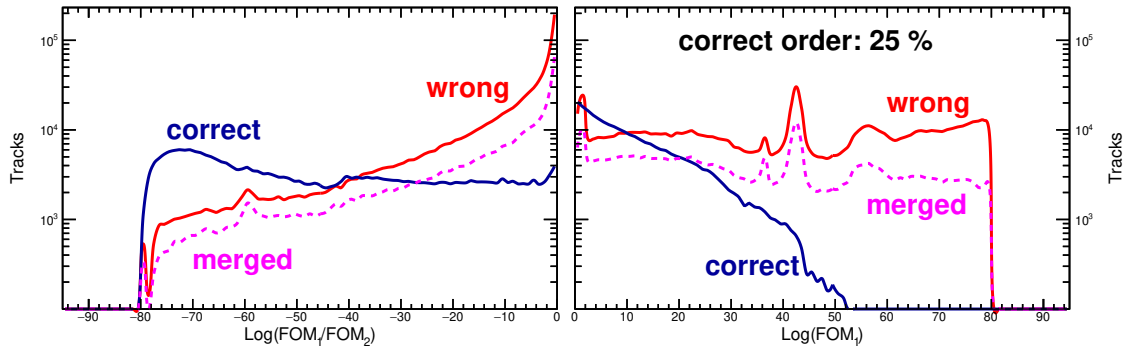

Figure 4.3: Results of the tracker using the centres of the segments as initial conditions, as in Figure 4.2, but all interaction that took place in the same segment have been merged into one hit.

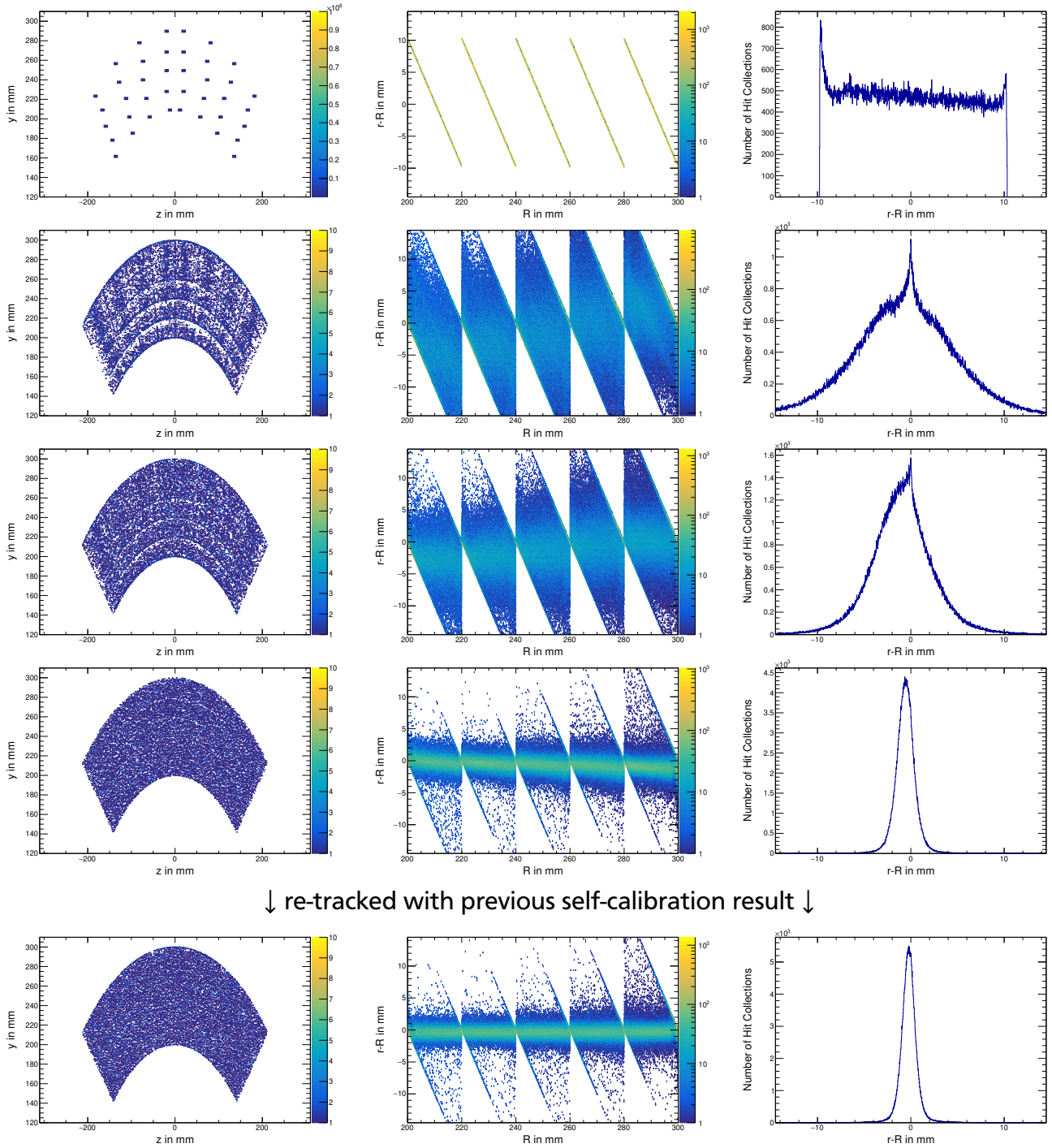

Figure 4.4: Overview over the results of the self-calibration for a realistic detector size and a hit collection diameter of 5 mm. The left column shows the hit collection positions for a slice of the detector. The middle column shows the difference Δr of the radii of the self-calibrated positions r and the real positions R plotted over R. The right column shows Δr for all hit collections. The plots show from top to bottom: Starting condition, 1st, 2nd, and 10th iteration. The last row shows the results after the 10th iteration for data which has been re-tracked using the results of the previous self-calibration. The resulting $\mathrm{RMSD_r}$ between the radius of the self-calibrated and real positions of the hit collections after 10 iterations is 1.22 mm and 1.06 mm after re-tracking. The systematic offsets after 10 iterations are −0.59 mm and −0.23 mm.

hit collections from larger radii get moved in to the centre, than hit collections from smaller radii get moved out, as discussed in Section 3.3. The effect is hereby significantly smaller than it was for Figure 3.1. For one, this is because the systematic offset of the initial condition is less severe for larger geometries. Secondly, the restriction of the hit collections to stay within their segments limits the formation of the offset, since every segment border acts as an anchor for the hit collections. After 10 iterations the $\mathrm{RMSD_r}$ is 1.22 mm with a systematic offset of −0.59 mm.

After this first self-calibration, the result is used to re-track the simulation data. Once more, the first set of cuts (c.f. Equation 4.3 and 4.4) is applied to the FOM and the self-calibration is repeated for a hit collection diameter of 5 mm. With this, the fraction of correct tracks is improved from 33% to 69% without the cuts and from 83% to 98% after applying the cuts. Again, the centres of the segments are used as initial conditions for the self-calibration. Now, after 10 iterations, the $\mathrm{RMSD_r}$ is 1.06 mm with a systematic offset of −0.23 mm. As can be seen in Figure 4.4, the Δr over R correlation is no longer visible. After 12 iterations the results were once more used to re-track and restart the self-calibration.

Figure 4.5 shows the progress of the $\mathrm{RMSD_r}$ and σ_r over the course of the iterations and the re-tracking. The first self-calibration was stopped after 10 iterations, the second after 12, and the last after 43. σ_r is thereby obtained by fitting a Gaussian function to Δr and is well suited to describe a large fraction of the hit collection. The $\mathrm{RMSD_r}$ is systematically larger than σ_r. This is caused by a small number of hit collections significantly further away than expected for a normal distribution, while the bulk of the hit collections follows the Gaussian shape, as can be seen in Figure A.1. The improvement due to the first re-tracking is clearly visible. The second re-tracking did not lead to a further improvement. But, since the resulting $\mathrm{RMSD_r}$ had only slightly improved with the first re-tracking and the tracker is expected to already be very reliable for an $\mathrm{RMSD_r}$ of 1.22 mm, this is to be expected.

Instead, as the inlay shows, continuing the self-calibration for more iterations gradually improves the result. The $\mathrm{RMSD_r}$ thereby slowly approaches the σ_r, reducing the deviation from the Gaussian shape. Similarly, the systematic offset continues to shrink with every iteration.

The interaction sequence of the tracks obtained from the twice re-tracked data was then used as input for a self-calibration with a hit collection diameter of 3 mm. The statistics was thereby increased by using the second set of cuts (c.f. Equation 4.5 and 4.6) for the FOM of the tracks. With this the 3 mm large hit collections have approximately half as many tracks as the 5 mm large hit collections from before, even though the volume was reduced by 78%. The results are very close to the 5 mm case, with an $\mathrm{RMSD_r}$ of 1.17 mm after 10 iterations, reaching down to 0.98 mm after 100 iterations. The systematic offset is −0.201 mm and −0.174 mm, respectively. An overview of the results can be found in Figure A.2. The long term evolution of these results is shown in Figure 4.6. As already seen before in Figure 4.4 for the 5 mm case, both $\mathrm{RMSD_r}$ and σ_r continue to improve for every iteration. The same holds true for the offset. However, as can be seen from these semi-logarithmic plots, the improvement is approximately proportional to the logarithm of the number of iterations. With this, the speed of convergence is indeed very slow and hardly justifies the computation time beyond few hundred iterations, especially as the convergence has to flatten at some point.

The influence of the hit collection diameter, on the achievable $\mathrm{RMSD_r}$ is shown in Figure 4.7(a). Similarly, the influence of the number of tracks per hit collection is shown in Figure 4.7(b). The data for the (a) is taken from the 5 mm data set discussed before, tracked, using the centres of the segments. Each of the self-calibrations with different hit collection diameters is limited to 300 tracks per hit collection, to remove the influence of the number of tracks. The data for (b),

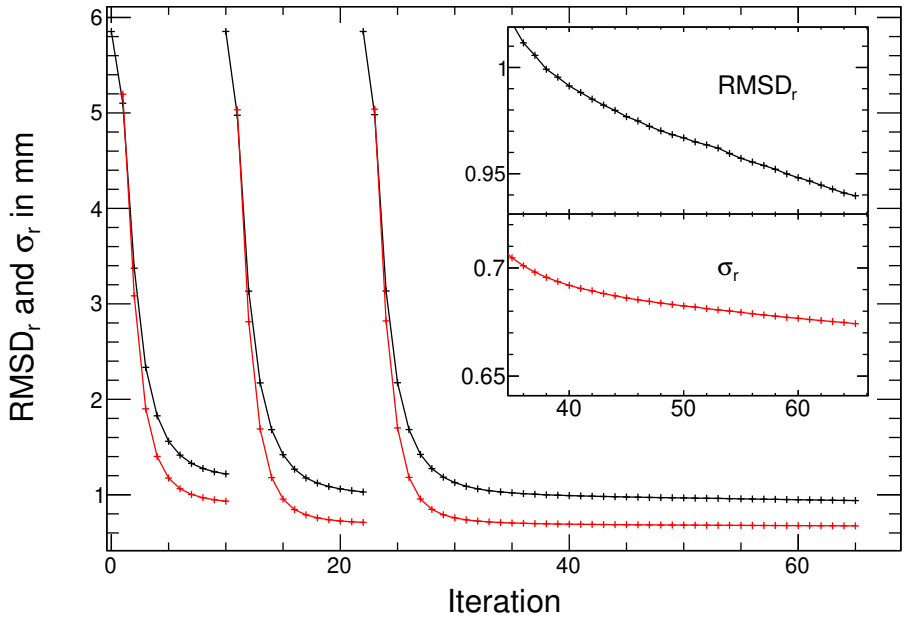

Figure 4.5: Resulting RMSD$_r$ (black) and σ_r (red) over the course of the iterations and the re-tracking for a hit collection diameter of 5 mm. The data was re-tracked and the self-calibration restarted after 10 and 12 iterations. The self-calibration continues to slowly improve even after a large number of iterations, as can be seen in the inlay.

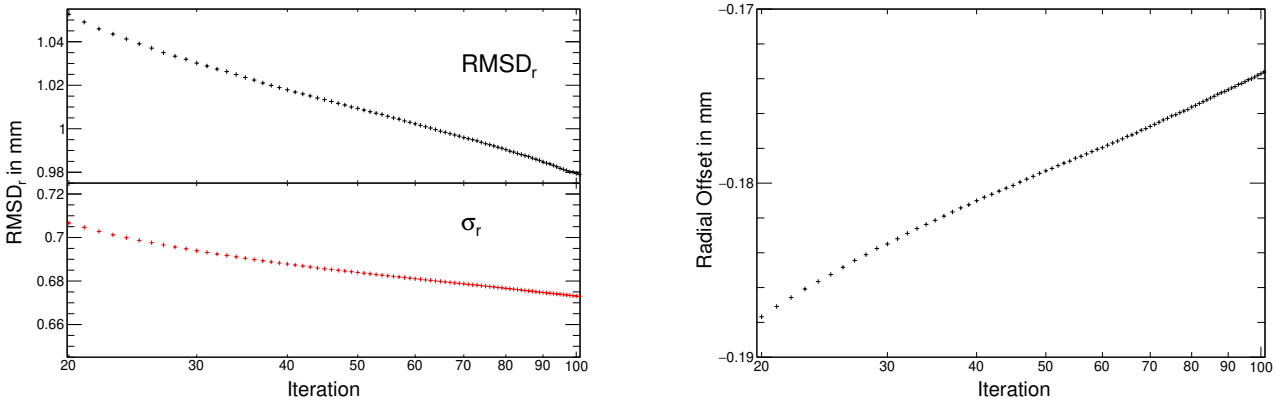

Figure 4.6: Resulting RMSD$_r$ and σ_r (left) and offset (right) of the self-calibration for a large number of iterations for a hit collection diameter of 3 mm. The results continue to improve even after a large number of iterations and the RMSD$_r$ continues to approach σ_r.

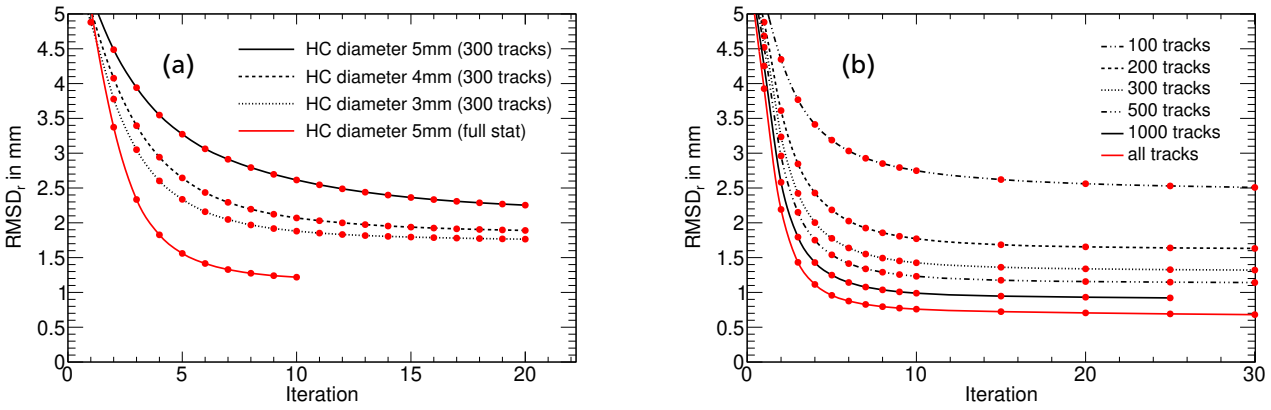

Figure 4.7: Influence of (a) the hit collection diameter and (b) the number of tracks in a hit collection on the achievable RMSD$_r$. The data for (a) was tracked using the centres of the segments. The data for (b) was tracked with a small Gaussian position resolution. Thus, the absolute values are not directly comparable. The results are only slightly influenced by the diameter of the hit collections, while changing the number of tracks significantly changes the results. Since changing the diameter of the hit collections also reduces the number of tracks, the net result will mostly be a deterioration of the achievable result.

however, is taken from a data set which was tracked with a small Gaussian position resolution. As such, the absolute values of the RMSD$_r$ are not directly comparable.

As can be seen in Figure 4.7(a), the diameter of the hit collection exhibits a small influence on the RMSD$_r$, with smaller diameters improving the results. The influence shown here is actually larger than seen for most other data sets, which show almost no correlation. On the other hand, removing the limitation to 300 tracks, and instead using the full data of approximately 2000 tracks per hit collection, leads to an improvement significantly larger than due to the hit collection diameter. Indeed, the number of tracks show a much stronger influence on the achievable RMSD$_r$, as can be seen from Figure 4.7(b). Since reducing the diameter of the hit collections necessarily leads to a reduction of the number of tracks per hit collection, the net result will in most cases be a deterioration of the achievable RMSD$_r$. As such, the acquired statistics is the main factor in achieving optimal results. Yet, even for very low numbers of tracks (<100) the self-calibration proved to be stable.

To finally extend the picture beyond the radius to the remaining coordinates, Figure 4.8 shows the results of the self-calibration with a hit collection diameter of 3 mm for the angles Φ and Θ, as well as for the Cartesian coordinates. The centres of the segments were used as initial conditions and the simulation data was tracked using the results from a previous self-calibration. The results are listed in Table 4.1. The Cartesian coordinates show very consistent results. The systematic offset for Θ has the same origin as the offset for r. Since there are more hit collections at larger Θ due to the larger solid angle, using the centres of the segments pulls in more hit collections. As such, the initial conditions have a bias towards smaller Θ. All in all, the remaining coordinates are consistent with the results for the radial component of the hit collection positions.

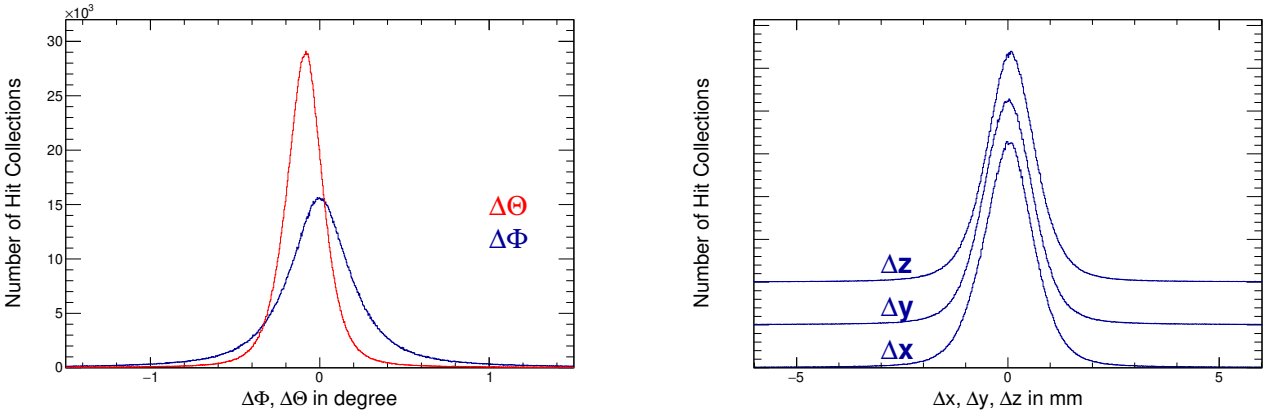

Figure 4.8: Results for polar (left) and Cartesian (right) coordinates of the self-calibration for a hit collection diameter of 3 mm after 100 iterations. The input data has been tracked, using the results of a previous self-calibration. The resulting RMSD, σ, and offset values are given in Table 4.1. The systematic offset of $\Delta\Theta$ is a remainder of the initial conditions.

Table 4.1: Results of the self-calibration for hit collections with a 3 mm diameter, using the centres of the segments as initial conditions, after 100 iterations. The input data has been tracked, using the results of a previous self-calibration.

	r in mm	Θ in deg	Φ in deg	x in mm	y in mm	z in mm
σ	0.580	0.127	0.235	0.624	0.615	0.608
RMSD	0.979	0.447	0.670	1.412	1.432	1.3434
offset	−0.174	−0.100	−0.001	0.005	0.002	0.083

5 Closing Remarks

The self-calibration is a novel technique to perform an in-situ position calibration of CTAs utilising a notably simple procedure. The primary input is the detector geometry and the initial energy of the γ ray, while no detailed knowledge of the electronic properties or the detector response is required. The method delivers a signal basis with unprecedented fidelity, while keeping the required calibration times to a minimum. At the same time the method proves to be robust against all tested influences, including energy resolution, wrong interaction sequences, coalescence distance, and low statistics. The presented method opens up the way for obtaining an optimum tracking performance, approaching the limits imposed by the sensitivity and the noise level of these CTAs.

It is hereby noted once more that the position resolution of the detector is a convolution of the fidelity of the signal basis and the accuracy of the basis. As such, the RMSD and σ values discussed before are a measure for the accuracy, while the diameter of the hit collections describes the fidelity of the basis. In a real detector system, the hit collections are not equal in size, nor are they spherical. Instead, they are shaped according to the pulse shape similarity, and thus, reflect the local sensitivity and noise levels of the detector. However, the self-calibration does not rely on either of these properties, but rather will converge at a position which – on average – best describes the hit collection.

While the self-calibration has been discussed and shown to work as a self sufficient calibration method, it can build upon the huge progress which has already been made with other techniques for these arrays. As such it is possible to start with an existing position calibration and from there improve the signal basis.

Obtaining a clear signal for the similarity check, though, requires a threshold on the deposited energy. The position sensitivity for energy depositions of above 100 keV has thereby been reported to still be of the order 1 mm [VKD00]. Nonetheless, the position resolution is energy dependent, but the discussed simulations and proof of principle do not allow to investigate this behaviour. Instead, a cut on the minimum energy deposition is assumed in the context of the feasibility to estimate the required measurement time.

Finally, the finite size of the source and the accuracy of its position inside the detector can influence the results. However, both influences can be eliminated in principle, since the source position can be included in the position optimization as well or not be used at all, thus, only using the interactions in the detector.

5.1 Feasibility

Based on the analysis, an estimated hit density of about 20 hits per mm^3 is sufficient to achieve robust convergence. This corresponds to approximately 300 hits per hit collection with a diameter of 3 mm, for which $RMSD_r$ values below 2 mm were reached. To achieve this interaction density at the back of the detector, roughly 2×10^{11} events need to be simulated for the full solid angle. This is equivalent to approximately 5×10^9 impinging γ rays per crystal of AGATA or

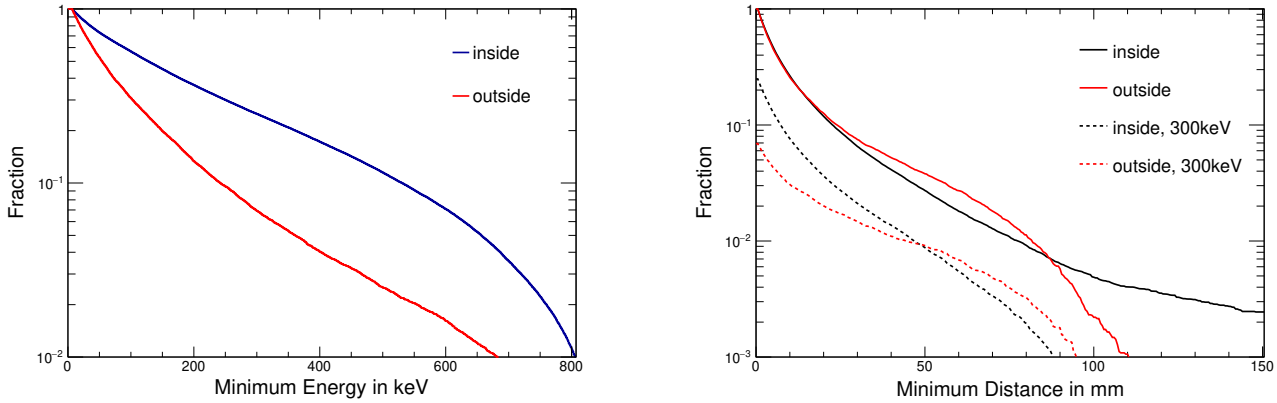

Figure 5.1: Fraction of tracks remaining after applying cuts to the minimum energy deposition (left) and the minimum distance between interactions (right). A track is counted if the first two or three consecutive interactions lie within the cut, since three interaction positions (including the source position) are the minimum requirement for the self-calibration. The numbers are based on the simulations of the geometry with realistic size, as shown in Figure 4.1. The fractions are shown separately for the innermost and outermost 5 mm of the detector. Since the interaction density on the inside is significantly larger than on the outside, equivalent reductions at the inside of the detector are less severe. The dashed lines show the remaining fractions depending on the minimum distance, including a cut of 300 keV on the minimum energy.

GRETA. Assuming a detection efficiency of 50% and keeping the detection rate for a crystal below 10 kHz, limits the source activity to below 2 MBq.

In an actual experimental implementation, requiring at least 300 keV energy deposition per hit, a minimum distance of 20 mm between hits, and a detection rate per crystal of a few kHz, one would need about 10 days of measurement time with a 1 MBq source. The effects of the cuts on the deposited energy and the distance between hits can be seen in Figure 5.1. The fraction of tracks remaining after applying the cuts steeply declines, especially for the outside of the detector. For the mentioned cuts, only about 3% of the tracks remain. As such, the cuts significantly influence the required measurement time. It is, however, emphasized that within this timescale the full array is calibrated.

With the current (not optimized) implementation of the self-calibration, one iteration for a crystal takes approximately 2.5 hours of CPU time on a Xeon E5-2690 at 2.90 GHz. The self-calibration is a highly parallelizable procedure with minimal multithreading overhead. Indeed, typically up to 56 cores were used, which brings the time down to about 3 minutes per iteration and crystal. Currently, the memory requirement per crystal is around 30 GB, though significant optimizations are certainly possible and can be reduced by a factor of three.

5.2 Outlook

The following will briefly discuss potential applications and additions to the self-calibration which could not be investigated in the course of this thesis.

In-Beam Measurement

While discussed in the context of a dedicated source measurement, the self-calibration does not rely on a specific measurement or setup. The only requirements are a known γ-ray energy and sufficient statistics. As such, even the use of in-beam data might be possible under certain conditions. While the prominent 511 keV might be to low in energy for a practical application, other background radiation with well known energies, like γ rays from Al(n,γ) reactions, could be used.

Uncertainty Information

Knowing the position of the hit collection is the most important step, though, the uncertainty of the thereby determined interaction positions is just as interesting. This uncertainty is linked to the fidelity of the signal basis, which is based on the size and shape of the hit collections. While a basic measure of the fidelity can be derived from the hit collection density alone, the actual size and shape of a hit collection will not be known for a real measurement. But, the size correlates with the number of tracks in a hit collection and its position in the detector. The position can thereby be determined from the self-calibration and the local interaction density can be simulated. From this, the size of the hit collection can be inferred directly. Similarly, the shape of the hit collection might be derived from the positions and sizes of the surrounding hit collections. This could provide additional information on the basis which can be used for an uncertainty estimation.

Multi-Hit Identification

Correctly identifying the pulse shapes of events with multiple hits in the same or neighbouring segments is a topic that needs further investigation. The hit collections are produced by pulse shape comparison. Therefore, such multi-hit events will be sorted into their own dedicated hit collections, unless the detector is inherently unable to resolve these events. Since merging multiple interactions this way destroys the energy-angle relation due to the Compton scattering, a position determination of such hit collections is impossible and meaningless. While it was already demonstrated in Section 4.1 that the tracker is able to preferentially remove these types of events from the input data, an explicit identification is still necessary to build a proper signal basis. The obvious approach is to check the recorded signal basis for linear dependencies. If the pulse shape of one hit collection can be generated by combining the pulse shapes of other hit collections, it is based on a multi-hit event. This can be computationally challenging, since the number of permutations which need to be checked is huge.

But, the number of tracks assigned to a hit collection might provide a sufficient marker to reliably identify multi-hit candidates and by that reduce the permutation space. Since identical multi-hit events – which lead to the same pulse shape and, thus, are sorted into the same hit collection – are less likely to occur than single-hit events, only hit collections with very low numbers of tracks have to be considered as multi-hit candidates. Therefore, only a fraction of all hit collections has to be checked for linear dependency.

Combination with other Measurements

The data collected in the context of the self-calibration is of course not limited to the application for the self-calibration. They can also be used for other applications, such as a position dependent energy calibration, e.g., in the context of correcting the change in energy resolution due to neutron damage, as discussed in [DLL05, BB13].

Extension Beyond Energy-Angle Relation

The presented analysis is based only on the energy-angle relation due to the Compton scattering. In principle, additional parameters can be included in the determination of a most probable hit collection position, for example, the differential cross section following the Klein-Nishina formula in Equation 2.4 and the mean free path of γ rays in matter. Both provide additional information that could allow for a faster convergence and provide additional constraints for the minimization, as the mean free path, for example, does not allow to arbitrarily scale the geometry.

And now for something completely different

(John Cleese)

Part II
Electromagnetic Properties of ^{21}O

The structure of exotic nuclei, in particular electromagnetic transitions between bound excited states, are key spectroscopic observables that provide an unparalleled testing ground for state-of-the-art nuclear interactions. Motivated by conflicting predictions from phenomenological and realistic nuclear interactions, this second part of the thesis reports on the measurement and analysis of the electromagnetic properties of ^{21}O, namely, the lifetime of its first excited state and the branching ratio of its second excited state. The experiment was performed in March 2016 at the NSCL facility, using the S800 spectrograph, the TRIPLEX plunger, and GRETINA.

6 Basics

This chapter discusses the basics for the lifetime measurement of ^{21}O. Section 6.1 gives an introduction to the oxygen isotopic chain and its relevance for nuclear structure investigations. The structure of the isotope of interest, ^{21}O, are discussed in Section 6.2. Section 6.3 then introduces shell model calculations, followed by Section 6.4 discussing ab-initio calculations. Finally, Section 6.5 presents the general concept of lifetime measurements and the methods used in this experiment.

6.1 Oxygen Isotopes

With the magic number of eight protons, the oxygen isotopic chain is the first magic chain providing a large variety of properties. Experimentally, the oxygen chain is by now accessible from the proton drip line at ^{13}O to the neutron drip line at ^{24}O, and even beyond, with the proton unbound ^{12}O and the neutron unbound $^{25\text{-}28}$O, as illustrated in Figure 6.1. As early as the late 1960's, starting from the doubly magic ^{16}O, calculations based on the free nucleon-nucleon interaction were used to calculate the spectrum of ^{18}O in the sd model space [KB66]. This laid the foundation for the development of the universal sd shell (USD) interaction, which is further discussed in Section 6.3.

With the calculations extending beyond ^{18}O, the oxygen isotopic chain presented various challenging features for nuclear theory. These include, for example, the very small strength of the Gamow-Teller β-decay of ^{14}O [CWB93] and the closed-shell properties of ^{22}O [SAD04, HMS13, CBN13]. The most prominent feature, though, is the so-called oxygen anomaly, where the neutron drip line jumps by six isotopes when going from oxygen to fluorine. ^{25}O [LQB85], ^{26}O [GMJK90], and even ^{28}O [TAA97] – which is doubly magic in the simple shell model – have been confirmed to be unbound. This puts the neutron drip line at ^{24}O, which proved to be difficult to reproduce by theory. While already implied by coupled-cluster calculations [HPD09], the successful reproduction of the neutron drip line in shell-model calculations decisively demonstrated the importance of three-nucleon (3N) forces for the description of all these features [OSH10]. As such, the oxygen isotopic chain became a key benchmark for the relatively recent development of calculations including 3N forces.

For the investigation of 3N forces, ab-initio approaches have proven to be highly effective, and have been applied very successfully for light nuclei [PW01]. In recent years, driven by the increase in computing power and the development of new theoretical methods, the applicable mass range for such ab-initio calculations has been extended dramatically [BLCR14]. As a result, e.g., interactions derived from chiral effective field theory (EFT) [ME11], calculations based on the in-medium SRG (IM-SRG) [BHH14], as well as conventional NCSM calculations [HBB13, HBC13], have been used to systematically study the closed-shell oxygen isotopes, followed by the extension to open-shell nuclei [GVHR17]. Section 6.4 gives a further introduction to ab-initio calculations.

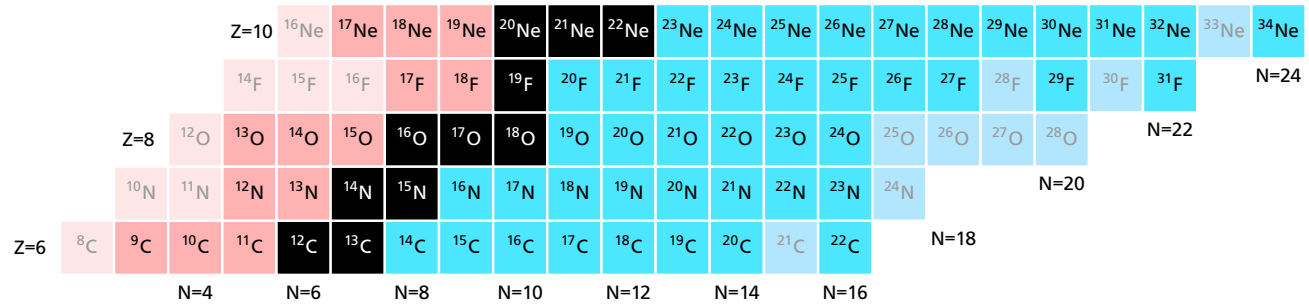

Figure 6.1: Nuclear chart around the oxygen isotopic chain. It shows the isotope for different proton number Z and neutron number N. The stable isotopes are black, β^+ unstable isotopes are red and β^- unstable isotopes are blue. The respective greyed out isotopes are unbound. Noteworthy is the step of the neutron drip line from ^{24}O to ^{31}F, where one additional proton binds six additional neutrons. The isotope of interest is the neutron rich ^{21}O.

In addition to bound oxygen isotopes, the properties of the unbound oxygen isotopes are an active topic of current research as, e.g., investigating ground-state resonances [LDK12, CSA13], and the possible two-neutron radioactivity of ^{26}O [KBB13, KCA17].

6.2 Details of ^{21}O

^{21}O is a neutron rich oxygen isotope located next to the weakly doubly magic ^{22}O. It has a lifetime of (4.93 ± 0.15) s [ALOM81] and decays via β^- decay to ^{21}F. The first measurements of excited states in ^{21}O via the reactions ^{18}O(^{18}O,^{21}O)^{15}O [NDRS82] and ^{18}O(^{18}O,^{15}O)^{21}O [CFOW89] laid the groundwork for the development of its level scheme, shown in Figure 6.2. The observation of multiple γ-ray transitions beyond the first excited state and $\gamma-\gamma$ coincidences [SAD04] solidified the level scheme. The energy of the first excited state has been measured twice via β-delayed γ-ray measurements with high precision as (1222 ± 3) keV [Lee09] and (1221 ± 3) keV [SMD10]. Combining these two measurements yields an energy of the first excited state of (1221.5 ± 2.2) keV. Transitions between the higher lying states have been measured only once before [SAD04]. The level scheme adopted for the analysis in this thesis is shown in Figure 6.2, where the energies of the higher lying states are based on the measurement in this thesis. The transition between the $3/2^+$ and $1/2^+$ of 900.5 keV has thereby been observed for the first time. The results of this measurement are further discussed in Section 8.3.

^{21}O has a $5/2^+$ ground state [SCO00], which is often described as a 0p–1h ground state with respect to the closed shell ^{22}O. The shell structure is given in Figure 6.3. All excited states given in the level scheme can be described as 1p–2h excitations, coupling the neutron in the $s_{1/2}$ to the $(d_{5/2})^{-2}$ states (0^+, 2^+, and 4^+), resulting in the excited states $1/2^+$, $3/2^+$, $5/2^+$, $7/2^+$, and $9/2^+$. With this, the excited states are expected to probe the $d_{5/2}$–$s_{1/2}$ effective single particle energy (ESPE) gap of approximately 4 MeV [SAD04, HMS13].

While all other transitions also have M1 components, the transition from the first excited state to the ground state is, in lowest order, an E2 transition. As such, the lifetime of the first excited state is a direct probe of the reduced electromagnetic transition strength B(E2) (c.f. Section 6.5). In addition, the branching ratio of the second excited state allows to constrain the B(M1) and B(E2) values of the respective transitions. Initial predictions based on USDB and NN+3N forces

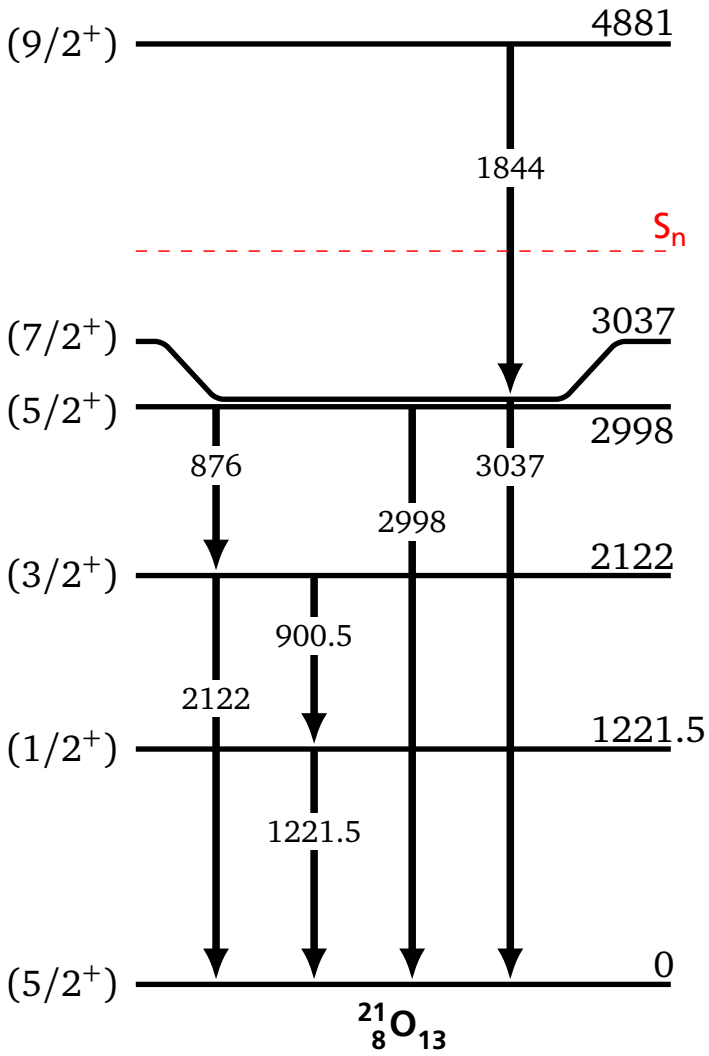

Figure 6.2: Level scheme of ^{21}O as determined by this experiment, with energies given in keV. The energy of the first excited state is obtained by combining the measurements in [LLY09] and [SMD10]. The energies of the higher lying states are obtained from the measurement in this thesis, using the well known energy of the first excited state as a reference. The 900.5 keV transition from the second to the first excited state is observed for the first time. Details on the energies and their uncertainties are given in Section 7.6 and Table 7.4.

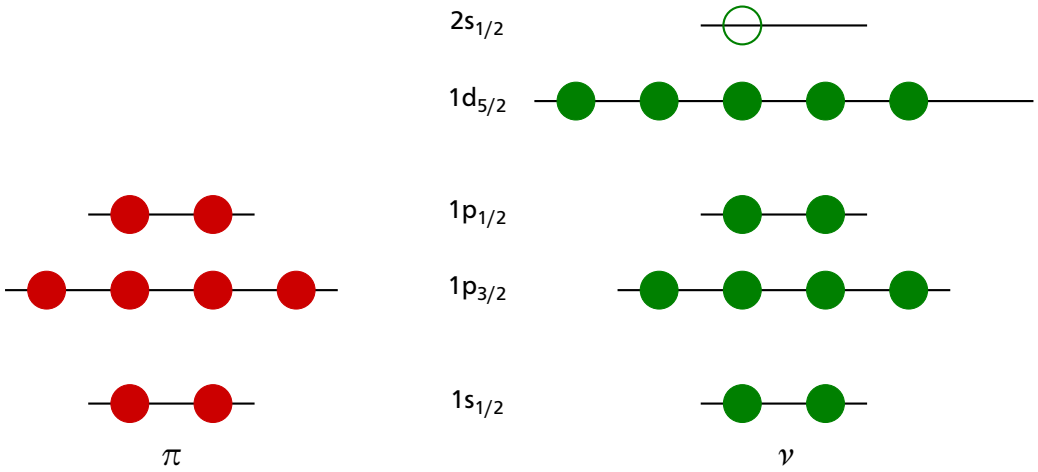

Figure 6.3: Shell structure of ^{21}O. The eight protons fill the s and p shell. The 13 neutrons reach up into the sd shell, where 5 neutrons occupy the $d_{5/2}$ orbit. The excited states are produced by exciting one neutron to the $s_{1/2}$ orbit and coupling it to the remaining $d_{5/2}$ neutrons. Therefore, the excited states probe the $d_{5/2}$–$s_{1/2}$ ESPE gap.

suggested a lifetime of around 100 ps and a branching ratio of around 10%. Therefore, these two observables mark the goal of the measurement in this thesis, since no experimental information is available yet on the transition strengths in ^{21}O.

The neutron separation threshold is 3.8 MeV, and with this the excited $9/2^+$ state at 4.9 MeV is unbound by 1.1 MeV. Nonetheless, it is observed to decay via γ-ray emission, since the respective neutron decay is strongly suppressed, as it can only couple to the 0^+ ground state of ^{20}O via an emission of an l=4 neutron, which is forbidden in the sd shell [CFOW89, SAD04].

6.3 Shell Model Calculations

This section will provide an introduction to shell-model calculations, starting with the general motivation of the concept, following the descriptions of, e.g., [Ber07, SP08]. After this, the explicit development of the USD interaction will be sketched in the context of the oxygen isotopic chain. Further information can be found in, e.g., [Bro17].

The fundamental problem which needs to be solved, is the Schrödinger equation

$$\hat{H}\,|\Psi\rangle = E\,|\Psi\rangle\,, \tag{6.1}$$

for which the details of the nuclear interaction are contained in the Hamiltonian $\hat{H}$. Separating the Hamiltonian into a kinetic energy operator $\hat{T}$ and potential $\hat{V}$ gives

$$\hat{H} = \sum_{i}^{A} \hat{T}_i + \hat{V}_A, \tag{6.2}$$

where $\hat{V}_A$ describes the potential of the nuclear A-body problem, which is, however, fundamentally unsolved. Motivated by the short range of the nuclear force, though, the potential can be limited to two-body interactions, resulting in the Hamiltonian as

$$\hat{H} = \sum_{i}^{A} \hat{T}_i + \sum_{i<j}^{A} \hat{V}_{ij}. \tag{6.3}$$

Hereby, $\hat{V}_{ij}$ describes the two-body NN interaction between the nucleons i and j. With this Hamiltonian, solving the Schrödinger equation on a basis of Slater determinants derived from, e.g., a harmonic oscillator (HO) basis, is in principle possible. For practical reasons, the basis has to be finite and thus truncated. This truncation is often expressed in terms of the principal quantum number of the HO, and thus the single-particle energy, as $n\hbar\omega$. A closer discussion of the basis and the details of the interaction in the context of such calculations is given in Section 6.4.

However, directly solving this problem, which is equivalent to diagonalizing the respective matrix H to obtain the eigensolutions, quickly becomes impossible for larger nuclei, as the dimensionality of the problem exceeds the computational capacities of current super computers.

To solve this problem of computability, the fundamental assumption of the shell-model approach is, to approximate the two-body interaction with a central potential $\hat{U}$ as

$$\hat{H} = \sum_{i}^{A} \left(\hat{T}_i + \hat{U}_i\right) + \sum_{i<j}^{A} \hat{V}_{ij} - \sum_{i}^{A} \hat{U}_i \tag{6.4}$$

$$= \quad \hat{H}_0 \quad + \quad \hat{H}_{\text{res}}. \tag{6.5}$$

In this case, $\hat{H}_0$ describes a system of independent particles in a central potential, and $\hat{H}_{\text{res}}$ describes the residual interaction between those particles, which is expected to be small if the mean field approximation is justified. Neglecting the residual interaction and, e.g., using a Woods-Saxon potential for $\hat{U}$, modified by a spin-orbit interaction, gives rise to the well known simple shell model. While this allows to describe some of the large scale systematics of nuclei, like, the magic numbers and many ground state spins J^π, the details are mostly lost. To recover these details, the residual interaction needs to be estimated.

The estimation of the residual interaction is based on the assumption that the nucleus can be described by N valence nucleons orbiting an inert core of A–N nucleons. Therefore, the Hamiltonian in Equation 6.4 can be split into two parts $\hat{H}$=$\hat{H}_{\text{core}}$+$\hat{H}_{\text{N}}$ as

$$\hat{H}_{\text{core}} = \sum_{i=N+1}^{A} \left(\hat{T}_i + \hat{U}_i\right) + \sum_{i<j=N+1}^{A} \hat{V}_{ij} - \sum_{i=N+1}^{A} \hat{U}_i \qquad \text{and} \tag{6.6}$$

$$\hat{H}_{\text{N}} = \sum_{i=1}^{N} \left(\hat{T}_i + \hat{U}_i\right) + \sum_{i=1}^{N} \sum_{j=N+1}^{A} \hat{V}_{ij} + \sum_{i<j=1}^{N} \hat{V}_{ij} - \sum_{i=1}^{N} \hat{U}_i. \tag{6.7}$$

Again, both parts can be understood as the sum of a central and residual term. In the limit of NN interactions, this formulation of the Hamiltonian holds true for any central potential $\hat{U}$, while the choice of $\hat{U}$ defines the size and accessibility of the residual interaction. Following the assumption of an inert core and the limitation to NN interactions, it is easy to motivate the central potential $\hat{U}$ as the mean potential produced by the two-body forces of the nucleons of the inert core

$$\hat{U}_i = \sum_{j=N+1}^{A} \hat{V}_{ij} \qquad \text{for } i<j, \tag{6.8}$$

which simplifies Equations 6.6 and 6.7 to

$$\hat{H}_{\text{core}} = \sum_{i=N+1}^{A} \left(\hat{T}_i + \hat{U}_i\right) \tag{6.9}$$

$$\hat{H}_{\text{N}} = \sum_{i=1}^{N} \left(\hat{T}_i + \hat{U}_i\right) + \sum_{i<j=1}^{N} \hat{V}_{ij}. \tag{6.10}$$

As can be seen, the residual interaction is reduced to the NN potential of the valence nucleons. This dramatically reduces the dimensionality of the problem, while keeping the residual interaction accessible in terms of the NN potentials, called the two-body matrix elements (sTBMEs).

Still, the TBMEs need to be determined, and with them, the effective NN interaction. An empirical approach to obtain such effective interactions is, e.g., by parametrizing the NN potential [EF55]. While such empirical effective interactions have been used successfully, their interpretation in terms of the underlying nuclear physics can be difficult. Instead, a more fundamental, microscopic approach to derive the effective NN interaction will be summarized in the following.

Universal sd Shell Interaction (A,B)

For the oxygen isotopes, the first approach to obtain the values of such TBMEs was an application in the sd shell for ^{18}O [KB66]. The sd shell (third principal quantum number) thereby describes the models valence space. The effective model space is reduced, because the first two shells are defined as the core. The TBMEs for this sd-shell interaction were derived, starting from the free nucleon-nucleon interaction. However, the interaction for bound nucleons differs significantly from the one for free nucleons, due to the Pauli principle. In fact, deriving the TBMEs from, e.g., scattering data proved to be very difficult. Instead, the TBMEs from the ^{18}O case were modified by fit to various experimental data, giving the USD interaction [BW88], which was later refined again, resulting in USDA and USDB [BR06]. The thereby obtained Hamiltonians, in particular USDB, have since been applied very successfully, predicting many excited states as well as reproducing the correct position of the neutron drip line at ^{24}O [Bro17].

As already mentioned in Section 6.1, the correct description of the neutron drip line for the oxygen isotopes requires the consideration of 3N interactions. Yet, the shell model approach of the USD, as sketched here, is limited to NN interactions. Instead, the success of the USDB Hamiltonian can be understood as a result of its effective nature. By looking at the 3N interactions as two core nucleons interacting with a single valence nucleon, or one core nucleon interacting with two valence nucleons, one can see how the appropriate choice of a central potential and the fit of the TBMEs to experimental data can incorporate at least some components of the 3N interactions.

6.4 Ab-Initio

The intention of ab-initio calculations is to describe the properties of nuclei starting from fundamental physical principles. In contrast to the effective approach discussed in the previous section, fits to experimental data are kept to a minimum, even though, no strict line can be drawn to separate the two. There are various ab-initio methods, but the focus of this section will be towards the ab-initio NCSM.

The initial problem is, again, given by the Schrödinger equation and the respective Hamiltonian in Equation 6.1 and Equation 6.2. And as for the shell model case, the nuclear A-body potential has to be treated in an approximative manner, splitting the potential into different many-body terms

$$\hat{H} = \sum_{i}^{A} \hat{T}_i + \sum_{i<j}^{A} \hat{V}_{ij}^{(\mathrm{NN})} + \sum_{i<j<k}^{A} \hat{V}_{ijk}^{(\mathrm{3N})} + \ldots, \tag{6.11}$$

with the two-body potential $\hat{V}^{(\mathrm{NN})}$, the three-body potential $\hat{V}^{(\mathrm{3N})}$, and omitted higher-body terms. The argument for the dominance of two-body interactions based on the short range of the nuclear force is still valid and, thus, it is no surprise that the resulting approximation is very similar to the shell model case. However, the fundamental justification can now be found in the underlying physical properties, e.g., derived from QCD.

There are many different potentials which are used for ab-initio calculations, like Argonne-V18 [WSS95], CD-Bonn [Mac01], or $\mathrm{V_{low\,k}}$ [BKS03]. Argonne-V18 and CD-Bonn are thereby phenomenological NN interactions based on a one-pion exchange in the former, and a more general one-meson exchange in the latter case. $\mathrm{V_{low\,k}}$, in turn, is an NN potential for which high- and low-momenta have been decoupled using the renormalization group (RG) method.

In the case of this thesis, the focus is put on the Hamiltonian by Entem and Machleidt (EM) [EM03] derived from chiral EFT. The following will, therefore, summarize the chiral EFT approach to derive this interaction, before Subsection 6.4.2 extends upon solving NCSM calculations.

6.4.1 Chiral Effective Field Theory

The interaction between nucleons fundamentally originates in the strong interaction described by QCD. In the low energy region relevant for nuclear physics, however, QCD is non-perturbative, which makes the description of the interaction between nucleons highly non-trivial. Lattice QCD, in principle, provides the tools to solve this problem, having been applied to, e.g., the neutron-proton scattering lengths [BBOS06]. But, the required computing power still limits its applicability for the general problems of nuclear physics and thus, lattice QCD can only be used for cross checks of key features. Instead, the development of chiral EFT allows to approximate the nuclear interaction, for which an extensive treatise can be found in [ME11].

Chiral EFT utilizes the symmetries of QCD at low energies and the separation of scales based on the pion mass (140 MeV) compared to the vector mesons at around 800 MeV. Starting from the QCD Lagrangian, an effective Lagrangian

$$\mathscr{L}_{\mathrm{eff}} = \mathscr{L}_{\pi\pi} + \mathscr{L}_{\pi N} + \mathscr{L}_{NN} + \ldots \tag{6.12}$$

is derived, for which $\mathscr{L}_{\pi\pi}$ describes the interaction among pions, $\mathscr{L}_{\pi N}$ describes the pion-nucleon interaction, and $\mathscr{L}_{NN}$ describes the contact term of the nucleon-nucleon interaction. Higher terms

of the Lagrangian are omitted here. Each term of this effective Lagrangian can itself be expressed by increasing orders as

$$\mathscr{L}_{\pi\pi} = \mathscr{L}^{(2)}_{\pi\pi} + \mathscr{L}^{(4)}_{\pi\pi} + \dots \tag{6.13}$$

$$\mathscr{L}_{\pi N} = \mathscr{L}^{(1)}_{\pi N} + \mathscr{L}^{(2)}_{\pi N} + \mathscr{L}^{(3)}_{\pi N} + \dots \tag{6.14}$$

$$\mathscr{L}_{NN} = \mathscr{L}^{(0)}_{NN} + \mathscr{L}^{(2)}_{NN} + \mathscr{L}^{(4)}_{NN} + \dots \tag{6.15}$$

$$\dots$$

At this point, the effective Lagrangian has infinitely many terms with no obvious ordering to the importance of the terms. Chiral perturbation theory provides the tools to sort the various terms according to powers ν of, e.g., the ratio $(Q/\Lambda_\chi)^\nu$ of the pion mass or momentum Q and the chiral breakdown scale $\Lambda_\chi \approx 1\,\text{GeV}$. From this, it can be shown that for a given order ν, only a finite set of terms contributes to the effective Lagrangian. The order ν thereby also provides an estimate of the relative size of the different contributions. This so-called power counting allows to create a hierarchy of nuclear forces, depicted in Figure 6.4. At leading order (LO) the two contributions are the nucleon contact term and the one-pion exchange, for good reason resembling the well-known Yukawa potential. At next to leading order (NLO) the higher order contact term is accompanied by multiple two-pion exchanges. The first onset of 3N forces can be found at second-next to leading order (N^2LO), while 4N forces appear at third-next to leading order (N^3LO).

As stated before, the expansion is based on powers of the ratio Q/Λ_χ. This necessitates that the potential is cut off for high momenta, typically around Λ=500 MeV, to avoid divergences. This is called regularization and is typically done with a local or non-local regulator function multiplied to the potential as

$$\hat{V}\left(\vec{p}\,',\vec{p}\right) \mapsto \hat{V}\left(\vec{p}\,',\vec{p}\right) f\left(p',p;\Lambda\right) \tag{6.16}$$

with

$$f\left(p',p;\Lambda\right) = \exp\left[-\frac{\left(p'-p\right)^{2n}}{\Lambda^{2n}}\right] \qquad \text{(local)} \tag{6.17}$$

$$f\left(p',p;\Lambda\right) = \exp\left[-\left(\frac{p'}{\Lambda}\right)^{2n} - \left(\frac{p}{\Lambda}\right)^{2n}\right]. \qquad \text{(non-local)} \tag{6.18}$$

The regulator is constructed such that $f\left(\vec{p}\,',\vec{p};\Lambda\to\infty\right) = 1$ and n is chosen according to the order of the interaction. Large momenta thereby correspond to interactions at short distances, for which Q/Λ_χ no longer provides a valid expansion. Instead, contact terms are introduced to describe the short range behaviour. The thereby appearing so-called low energy constants (sLECs) can be fitted to, e.g., scattering data, and thus, renormalise the potential after the previous regularization.

Based on this, the EM Hamiltonian is constructed from an N^3LO NN and an N^2LO 3N interaction, which are fitted to NN scattering data as well as the properties of A=3 and A=4 nuclei [EM03]. Two variants of this interaction will be used for the later comparison in 8.4. The first variant is the EM(400), for which a reduced cut-off of Λ=400 MeV is used with a local regulator [Nav07]. The more recent interaction is the EM(500), for which a cut-off at 500 MeV is used with a non-local regulator [EM03]. Furthermore, Entem-Machleidt-Nosyk (EMN)(500) extends the NN potential to N^4LO with the 3N interaction at N^2LO with a non-local regulator and a cut-off at 500 MeV [EMN17, EKMN15].

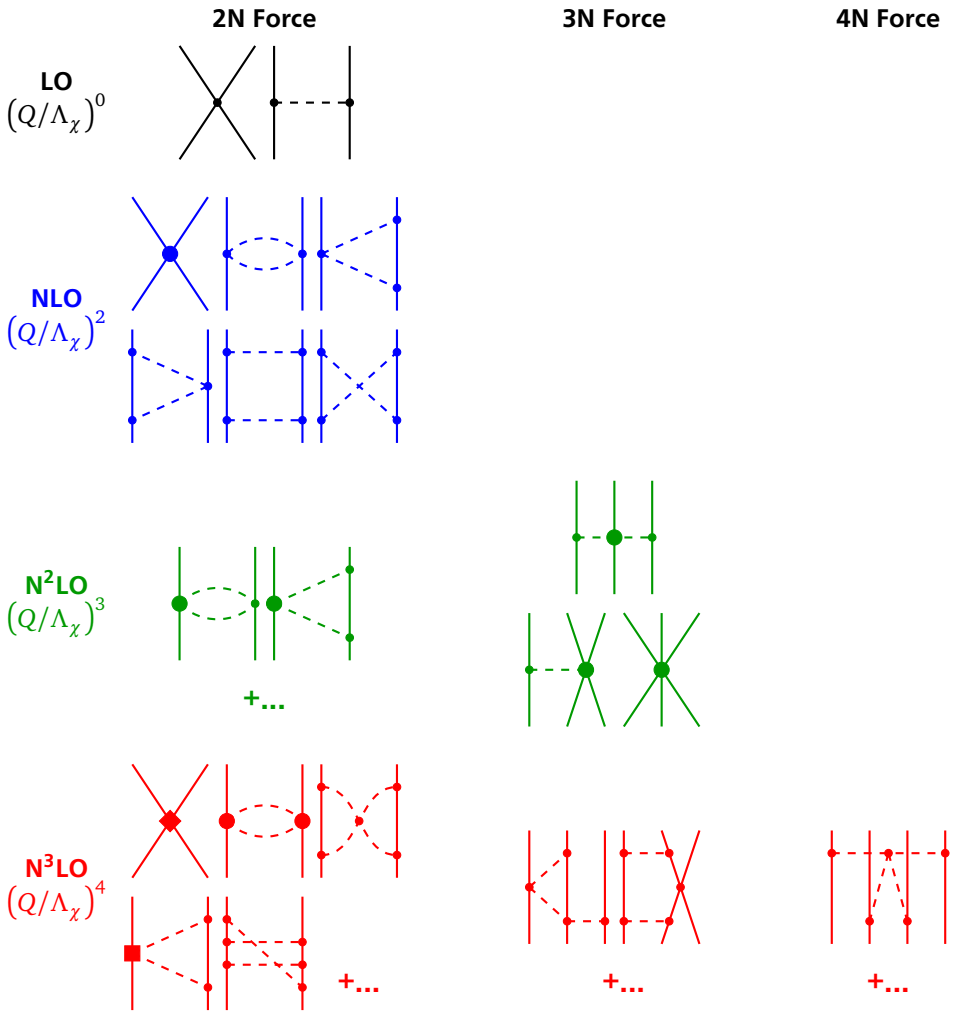

Figure 6.4: Hierarchy of nuclear forces from chiral perturbation theory. Solid lines represent nucleons, dashed lines represent pions. Small dots, large dots, squares, and diamonds denote vertices of order 0, 1, 2, and 4, respectively. At LO the nucleon contact term and one-pion exchange contribute. At NLO additional two-pion exchanges occur. At N^{2}LO 3N forces appear, at N^{3}LO 4N forces. The figure is adopted from [ME11].

6.4.2 No-Core Shell Model

An overview over the NCSM can be found in, e.g., [BNV13], of which a brief introduction follows below. Given a potential, the next requirement to solve the Schrödinger equation is the definition of a basis in which it will be calculated. Because nucleons are fermions, the basis, thereby, needs to be antisymmetric. Motivated by the symmetries of nuclei, a HO basis is most typically used, which, in addition, allows to utilize many tools developed in the context of this basis. A natural choice of coordinates for the nuclear problem are the relative coordinates of the nucleons, the Jacobi coordinates. However, while it is in principle possible to antisymmetrize a Jacobi coordinate basis for any given A, it becomes impractical for systems with A>4. Instead, typically a regular single-particle HO basis is used as a starting point

$$|\alpha\rangle = |nlm_l\rangle \otimes |sm_s\rangle \otimes |tm_t\rangle\,, \tag{6.19}$$

with the principal quantum number n, angular momentum l, spin s, and isospin t, as well as their respective projections m. From this, an antisymmetric Slater determinant for an A-body system is constructed as

$$|\alpha_1\alpha_2\ldots\alpha_A\rangle = \frac{1}{\sqrt{A!}}\sum_\pi \mathrm{sgn}(\pi)\hat{P}_\pi\left(|\alpha_1\rangle \otimes |\alpha_2\rangle \otimes \cdots \otimes |\alpha_A\rangle\right). \tag{6.20}$$

With this, the wave function $|\Psi\rangle$ can be written as a combination of Slater determinants

$$|\Psi\rangle = \sum_{\alpha_1<\alpha_2<\cdots<\alpha_A} C_{\alpha_1\alpha_2\ldots\alpha_A}\,|\alpha_1\alpha_2\ldots\alpha_A\rangle\,. \tag{6.21}$$

At this point the basis is infinite. Thus, the model space needs to be truncated for the problem to be tractable. In light of the HO basis, the choice for the truncation is, unsurprisingly, given in terms of the principal quantum number n and angular momentum l, e.g., as

$$N_{\mathrm{tot,max}} \geq \sum_i^A (2n_i + l_i). \tag{6.22}$$

As a result, the total excitation energy of all nucleons is limited. The dimension of the problem thereby increases combinatorially with $N_{\mathrm{tot,max}}$ and A. Regularly, the truncation is given with respect to the ground state as N_{max}. A method to further improve the truncation is the importance truncation method [Rot09], derived from multi-configuration perturbation theory.

At this point, solving the Schrödinger equation is mostly a computational problem. It is equivalent to diagonalizing the respective matrix or making use of the variational principle. However, to obtain accurate results, the model space needs to be very large, which is only feasible for very small systems. To extend the applicability of the ab-initio NCSM to larger systems, methods have been developed to improve the computability, of which the following introduces methods based on the similarity renormalization group (SRG) [BFP07].

6.4.3 Similarity Renormalization Group Methods

The fundamental motivation of the SRG methods is the transformation of the Hamiltonian into a more convenient form, without changing its spectrum and thus the described physics. Following the descriptions in [HBM16, Her16], the Hamiltonian is modified by a continuous unitary transformation as

$$\hat{H}_\alpha = \hat{U}_\alpha \hat{H} \hat{U}_\alpha^\dagger, \tag{6.23}$$

with the flow parameter α, which parametrizes the unitary transformation $\hat{U}$.

Using an anti-Hermitian generator

$$\hat{\eta}_\alpha = -\hat{\eta}_\alpha^\dagger = -\hat{U}_\alpha^\dagger \frac{\mathrm{d}}{\mathrm{d}\alpha} \hat{U}_\alpha, \tag{6.24}$$

the operator flow equation is given by the derivative of Equation 6.23 as

$$\frac{\mathrm{d}}{\mathrm{d}\alpha} \hat{H}_\alpha = \left[\hat{\eta}_\alpha, \hat{H}_\alpha\right]. \tag{6.25}$$

With this, the Hamiltonian can be smoothly transformed by integrating the flow equation for $\alpha \to \infty$. The choice of the generator $\hat{\eta}_\alpha$ is thereby crucial and defines how the Hamiltonian will be transformed. One, rather simple, example is given by the relative kinetic energy in NN space as

$$\hat{\eta}_\alpha = \left[\hat{T}_{\mathrm{rel}}, \hat{H}_\alpha\right]. \tag{6.26}$$

For this generator, the Hamiltonian is driven towards a diagonal in the momentum eigenbasis of the kinetic energy operator. As a consequence of this diagonalization, the low and high momentum parts of the Hamiltonian become decoupled, which allows for significantly improved convergence properties.

An extension upon the SRG, the IM-SRG [TBS11], uses normal ordering and Wick's theorem to evolve the A-body operators and approximates them, using – computationally cheap – two-body methods. With the generalized normal ordering and Wick's theorem, the method is extended to the multi-reference IM-SRG (MR-IM-SRG) [HBC13, Her16, GVHR17]. The MR-IM-SRG is thereby capable of describing closed- and open-shell nuclei with respect to a reference state. For technical reasons, this reference state should have $J^\pi{=}0^+$. This requirement presents a complication for the MR-IM-SRG application to odd-A nuclei, which necessarily have half-integer spin. A publication describing a method using reference states from the neighbouring nuclei, as it is used for ^{21}O, is pending.

In the end, the MR-IM-SRG provides a Hamiltonian, which is constructed for a specific reference state and model space and which is decoupled from all other Slater determinants beyond this model space. Practically, this allows for relatively small model spaces, and thus, very fast convergence. At the same time, the results are still close to the unmodified Hamiltonian with larger model space, due to the decoupling. The observables of interest can then be obtained by an equivalent transformation of the respective operators.

6.5 Lifetime Measurements

In simple terms, the goal of measurements in nuclear physics can often be described as the endeavour to access information about the wave functions and matrix elements governing the nuclear interactions, and their comparison to the predictions from theoretical models. Measurements of the lifetimes of excited states are thereby one of the many ways to experimentally access this information. Following the comprehensive description in [Ber07], the decay of an initial state $|J_\mathrm{i}\rangle$ to a final state $|J_\mathrm{f}\rangle$ via electromagnetic radiation is described by the reduced matrix element of the electromagnetic transition operator as

$$\langle J_\mathrm{f}||\mathscr{M}(\sigma l)||J_\mathrm{i}\rangle\,, \tag{6.27}$$

with σ stating the type of transition as electric (E) or magnetic (M), and the multipole order of the transition l. This operator is connected to the reduced electromagnetic transition strength by

$$B\,(\sigma l; J_\mathrm{i}{\rightarrow}J_\mathrm{f}) = \frac{1}{2J_\mathrm{i}+1}|\langle J_\mathrm{f}||\mathscr{M}(\sigma l)||J_\mathrm{i}\rangle|^2, \tag{6.28}$$

which in turn is connected to the partial decay width

$$\Gamma\,(\sigma l; J_\mathrm{i}{\rightarrow}J_\mathrm{f}) = \frac{8\pi\alpha\hbar c}{e^2}\frac{l+1}{l\,[(2l+1)!!]^2}\left(\frac{E_\gamma}{\hbar c}\right)^{2l+1} B\,(\sigma l; J_\mathrm{i}{\rightarrow}J_\mathrm{f})\,. \tag{6.29}$$

Hereby, E_γ denotes the energy difference between the initial and final state, and with that, the energy of the emitted γ ray. This partial decay width might be modified by an additional factor $(1+\alpha)$, due to internal conversion, for which, instead of the γ ray, an atomic electron is ejected [BW12]. The internal conversion coefficient α is thereby the ratio of the probabilities for a γ decay and such an electron emission. The internal conversion coefficient scales with the overlap of the electrons wave function with the nucleus. As such, it is most probable for tightly bound s-wave electrons and heavy nuclei, and for low energy transitions with high multipole order. For a nucleus as light as ^{21}O and an E2 transition with an energy of over 1 MeV, the contribution from internal conversion is expected to be negligible. Furthermore, for the experimental conditions discussed in this thesis, the internal conversion can be neglected, as the fragments are fully stripped.

As is evident from Equation 6.28, the calculation of the decay width involves the difficulty of requiring the wave functions of the real nucleus, which are not implicitly known. Still, as described by Weisskopf [Wei51], an order of magnitude estimate for electric and magnetic transitions is possible as

$$\Gamma_\mathrm{E} = \frac{2(l+1)}{l[(2l+1)!!]^2}\left(\frac{3}{l+3}\right)^2 e^2\left(\frac{E_\gamma}{\hbar c}\right)^{2l+1} R^{2l} \tag{6.30}$$

$$\Gamma_\mathrm{M} = \frac{20(l+1)}{l[(2l+1)!!]^2}\left(\frac{3}{l+3}\right)^2 e^2\left(\frac{E_\gamma}{\hbar c}\right)^{2l+1} R^{2l}\left(\frac{\hbar}{mcR}\right)^2, \tag{6.31}$$

with the mass m and the radius R of the nucleus.

The lifetime of the initial state is then given by the total decay width as

$$\tau = \frac{\hbar}{\Gamma_{\text{total}}}. \tag{6.32}$$

The total decay width is thereby the sum of all partial decay widths, i.e., for all possible final states and transitions. The relevant transitions can often be reduced to one or two contributors, since the size of the partial decay width is reduced by a factor of 1000 for every multipole order l. Similarly, electric transitions are in general about two orders of magnitude stronger than magnetic transitions of equal multipole order. With this, the most relevant transitions are the lowest order electric or magnetic transition, or the combination of these two. The possible transitions are given by the selection rules for the angular momentum

$$|J_\text{i} - J_\text{f}| \leq l \leq J_\text{i} + J_\text{f} \tag{6.33}$$

and the parity

$$\text{(electric)} \quad \pi_\text{f} = (-1)^l \times \pi_\text{i}, \tag{6.34}$$

$$\text{(magnetic)} \quad \pi_\text{f} = (-1)^{l+1} \times \pi_\text{i}. \tag{6.35}$$

While the lifetime of the initial state is given by the total decay width, the probability to decay to a specific final state is given by the respective partial decay width. As such, the branching ratio is given by

$$BR\left(J_\text{i} \rightarrow J_\text{f}\right) = \frac{\Gamma\left(J_\text{i} \rightarrow J_\text{f}\right)}{\Gamma_{\text{total}}}. \tag{6.36}$$

With all this, the measurement of decay widths, lifetimes, and branching ratios allows to directly access the reduced electromagnetic transition strengths. A large number of experimental methods has been developed for this kind of measurements with a wide range of sensitivity, as can be seen in Figure 6.5. The methods are categorized into indirect methods, measuring the decay width Γ, and direct methods, measuring the lifetime τ. Indirect measurements like (e,e') scattering, thereby, often measure the time reversed process of the decay, which is related to the already discussed reduced electromagnetic transition strength by

$$B\left(\sigma l; J_\text{f} \rightarrow J_\text{i}\right) = \frac{2J_\text{i} + 1}{2J_\text{f} + 1} B\left(\sigma l; J_\text{i} \rightarrow J_\text{f}\right). \tag{6.37}$$

Recoil Distance Method

To measure the expected lifetime of about 100 ps, predicted by, e.g., USDB shell model calculations, the recoil distance method (RDM) was used. Hereby the isotope of interest is produced in flight and the Doppler shift of the detected γ rays is used to determine the lifetime. The detected energy is shifted due to the Doppler effect as

$$E_\text{lab} = \frac{E_\text{cm}}{\gamma\left(1 - \beta \cos\theta_\text{lab}\right)}. \tag{6.38}$$

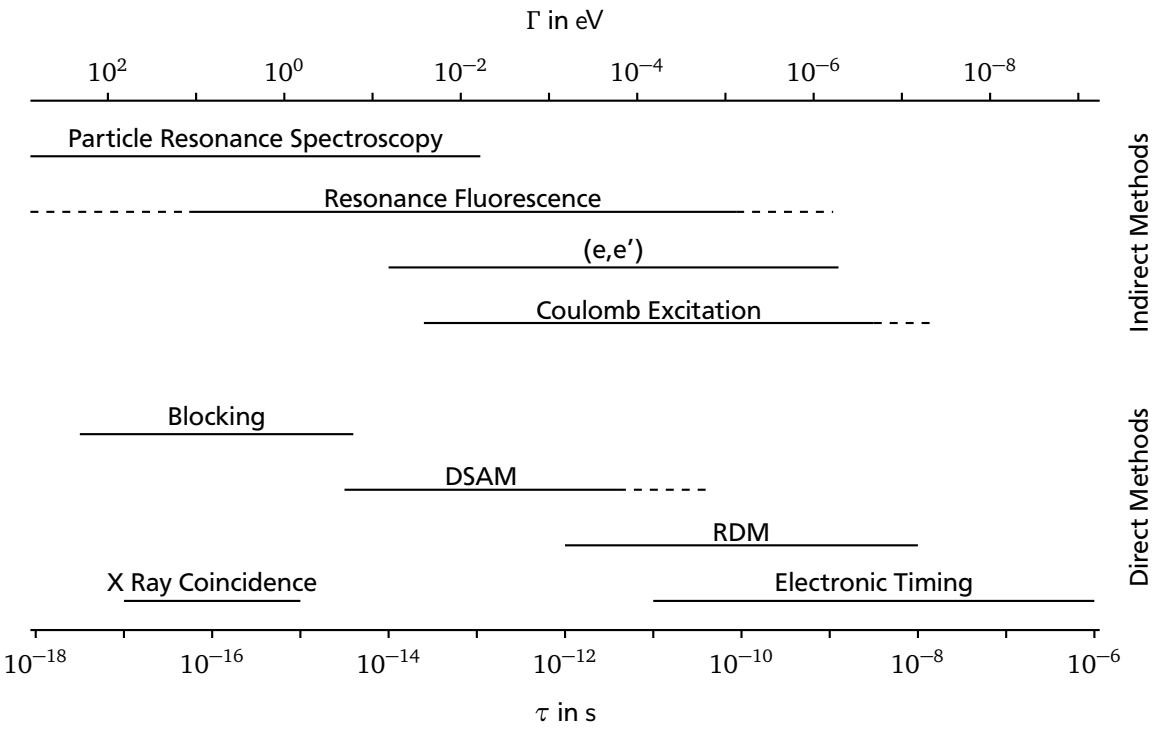

Figure 6.5: Sensitive regions for different lifetime measurement methods. The techniques are divided into methods which directly measure the lifetime τ and methods which determine it indirectly via the decay width Γ. The graph has been adopted from [NSS79].

For a given detection angle θ_{lab}, the detected energy E_{lab} is thus defined by the centre-of-mass energy E_{cm} of the γ ray and the velocity β of the projectile. Typically, an RDM setup consists of a target and one or two degraders, surrounded by a γ-ray detector. Figure 6.6 shows a sketch of the measurement principle for the case of a single degrader, as it was used in the experiment in this thesis.

For a sufficiently thin target and degrader, this setup produces two regions with distinct kinetic energies. The first region is located between the target and the degrader and corresponds to a higher kinetic energy of the particle of interest. The second region is located after the degrader and relates to a lower kinetic energy due to the energy loss in the degrader. Therefore, the resulting energy spectrum contains two peaks, namely the Doppler shifted peak from the high energy region (fast peak) and the Doppler shifted peak from the low energy region (slow peak). The energy difference of these two peaks is a result of the energy loss within the degrader and depends on the angle at which the γ rays are detected. The intensity ratio of the two peaks is directly linked to the number of decays taking place in the two energy regions. Since, for a known projectile velocity, the two energy regions correspond to two time windows, the intensity ratio is also directly linked to the lifetime of the decay. As a result, the lifetime of the state can be directly compared to the time of flight between the target and the degrader.

In a real experiment, however, the state of interest is not only produced in the target, but also in the degrader. If the reaction takes place in the degrader, the resulting γ ray can only be observed in the slow peak and thus systematically shifts the result towards longer lifetimes. The direct way to account for this is to measure the degrader reaction ratio (DRR) directly by selecting a long enough distance between target and degrader, such that all states of interest produced in the target have decayed upon reaching the degrader. The remaining slow peak is

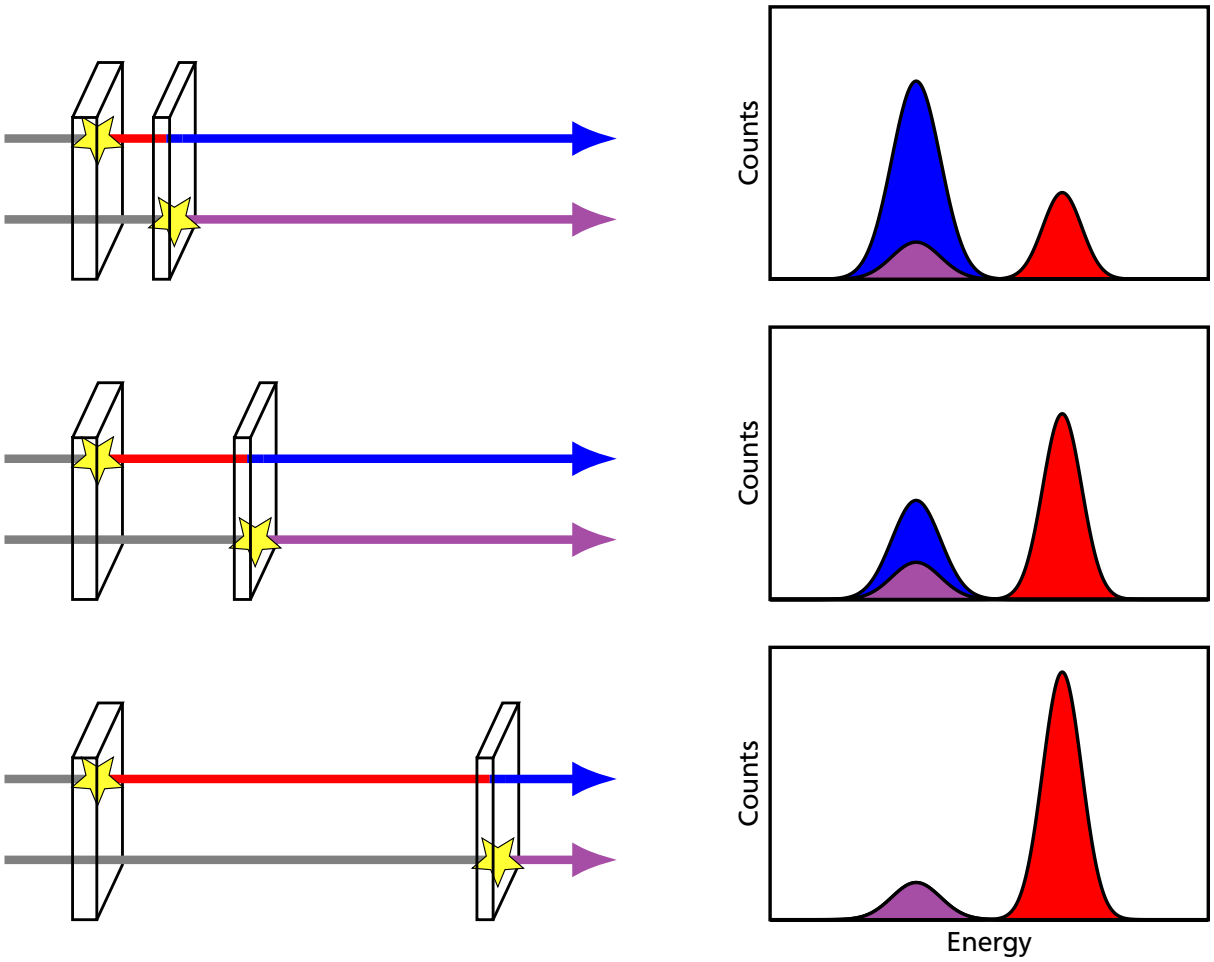

Figure 6.6: Illustration of the concept of the RDM. The incoming beam (gray) enters the setup from the left. The reaction (yellow star) producing the state of interest can occur in the target or in the degrader. If the deexcitation takes place before the degrader, the kinetic energy of the fragment is large and therefore the Doppler shift is large, producing the fast peak (red). After the degrader the kinetic energy is lower and γ rays from this region will be seen with a smaller Doppler shift, producing the slow peak (blue). If the state of interest is produced in the degrader, any deexcitation will take place in the region of small kinetic energy and thus contribute to the slow peak (purple). Changing the distance between the target and the degrader will change the ratio of the fast and slow component accordingly. Measuring at a sufficiently large distance allows to directly measure the DRR.

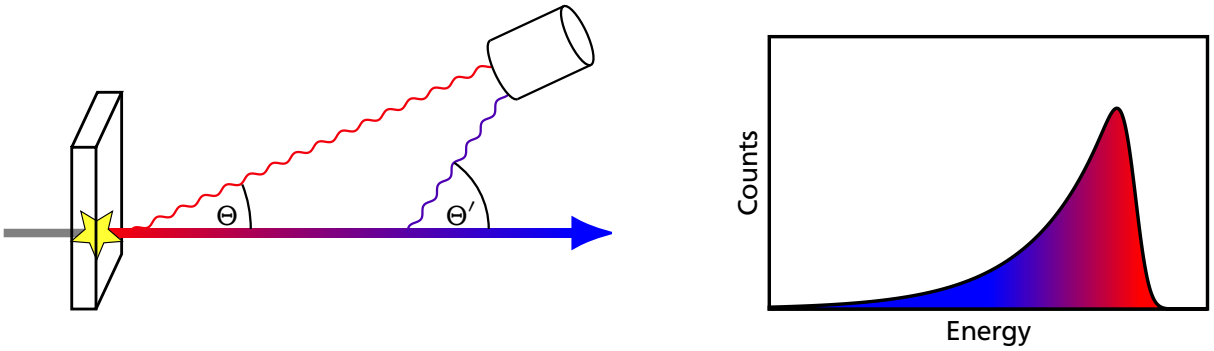

Figure 6.7: Illustration of the peak shape due to the change of the detection angle. Since the decay position is unknown, the target position is used to determine the detection angle for the Doppler correction. A γ ray produced close to the target will therefore have a detection angle which is close to the emission angle. Further away from the target the emission angle will be significantly larger than the detection angle. Because of this, the Doppler correction will over-correct the detected energies to lower energies. In combination with the exponential decay of the excited state, this produces a tail towards low energies.

then produced only by reactions in the degrader. However, in the experiment analysed in this thesis, the setup did not allow for a large enough target-degrader distance to measure the DRR directly.

Already during the first measurement with the target only, the peak of interest was seen with a strong tail towards lower energies. This tail is a result of the change of the detection angle due to the distance the fragment travels before the decay, as illustrated in Figure 6.7. Since the Doppler correction is performed assuming that the γ ray originates from the target position, those γ rays which are emitted significantly behind the target are over-corrected. Due to the exponential decay along the flight path, decays further downstream are less common, which then results in the observed peak shape with a low energy tail [DRG10, DPBD12]. Therefore, the shape of this tail is linked to the lifetime and, compared to the expectation, indicates a rather long lifetime in the order of 500 ps. The lifetime information from the measurement with the target only is thereby independent of the DRR.

On the other hand, if the lifetime is much shorter, the peak will not exhibit a significant deviation from a Gaussian shape. Nonetheless, the lifetime can leave a signature and result in a centroid shift of the observed peak. While the centroid shift method [Bay50, BHK55] was developed in the context of electronic timing measurements, the concept is applicable to other measurements as well. This centroid shift is a consequence of the convolution of a Gaussian energy resolution with an exponential signal from the decay, resulting in an exponentially modified Gaussian. The exponential signal can thereby be a result of the change in detection angle, as discussed above, but also, e.g., the energy loss in the target. On average, the longer the lifetime, the more energy the fragment will have lost, before the γ ray is emitted. This is a typical feature exploited in doppler-shift attenuation method (DSAM) measurements, where the line shape due to the energy loss is used for the lifetime measurement. As such, if the energy of a transition is well known, the lifetime can be obtained from the observed energy difference, i.e., the centroid shift.

7 Setup and Calibration

This chapter covers the experimental details of the measurement of ^{21}O, performed at the national superconducting cyclotron laboratory (NSCL) at Michigan state university in March/April 2016. At the NSCL two coupled cyclotrons, K500 and K1200, were used to accelerate a ^{48}Ca beam into the A1900 fragment separator (A1900) onto a ^{9}Be production target. In the production target, numerous reactions took place, producing a large variety of fragments, from which the A1900 selected ^{24}F at an energy of 95 AMeV. The so produced ^{24}F beam had a purity of 95% with a momentum spread of about 2%. It was lead into the S3 vault, where the triple plunger for exotic beams (TRIPLEX) held a secondary ^{9}Be target with a thickness of 2 mm (370 mg cm^{-2}) and, if necessary, a ^{181}Ta degrader with a thickness of 0.92 mm (1532 mg cm^{-2}). In the secondary target ^{21}O was produced from the impinging ^{24}F. Around the target position the gamma-ray energy tracking in-beam nuclear array (GRETINA) was mounted to detect the emitted γ rays. After passing through the target and the degrader, the beam and the reaction products entered the S800 spectrograph (S800), where they were identified.

The experiment started with the first setting using only the target (TO$_1$). For this first night the achieved beam intensity of ≈200 nA for ^{24}F was significantly below the expectations. To improve on this, the beam was retuned the next morning. Reviewing the data recorded over night did not show the peak of interest at 1221.5 keV, even though the other transitions of ^{21}O where clearly visible. Based on this discrepancy, it was decided to continue taking data with the second setting using only the target (TO$_2$). The beam intensity was now significantly improved to ≈900 nA. With this data the peak of interest was visible, though it exhibited a long tail to lower energies. This broad shape explains why the peak was not visible with the low statistics in TO$_1$. In addition, this hints towards a significantly longer lifetime than the expected 100 ps. First simulations estimated the lifetime in the order of 500 ps.

The next morning the ^{181}Ta degrader was installed in the TRIPLEX. Because of the new fragment velocities the settings of the S800 were adjusted to maximize the ^{21}O yield and the data with the first setting with a degrader separation of 25 mm (DS25$_1$) was recorded. After this, the target was moved upstream by 20 mm and with this setup data was recorded with the degrader separation of 45 mm (DS45). Finally, the target was moved back by 20 mm to the middle position, and second setting with a degrader separation of 25 mm (DS25$_2$) was recorded. With this, the measured counts for ^{21}O are approximately equal for the combined measurements TO$_{1,2}$, DS25$_{1,2}$, and DS45.

GrROOT was used to unpack the experiment data for the offline data analysis, while the remaining analysis is done with ROOT directly.

The following sections 7.1 to 7.4 give an introduction to the different components of the experimental setup and their calibrations. Section 7.5 elaborates on the Doppler correction, after which Section 7.6 summarizes the final spectra obtained from the measurement.

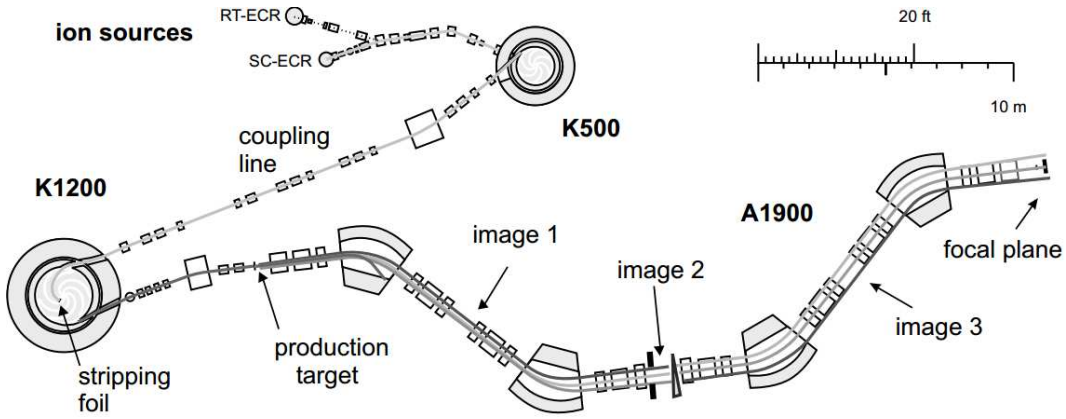

Figure 7.1: Sketch of the NSCL facility with its cyclotrons and the A1900. [MSS03]

7.1 A1900 Fragment Separator

The purpose of the A1900 [MSS03] is to select and deliver specific isotopes to the experimental halls. To achieve this, the incoming primary beam is lead onto a production target, where nuclear reactions produce a large spectrum of fragments. Figure 7.1 shows a sketch of the A1900 and the accelerator. Behind the production target a set of superconducting magnets is used to gather and select the produced fragments. A first pair of dipole magnets separates the fragments according to their magnetic rigidity

$$B\rho = \frac{mv}{q}, \tag{7.1}$$

with their bending radius ρ in the magnetic field B of the magnets. As can be seen, this separates the beam according to the momentum to charge ratio of the fragments. Since the fragments are fully stripped for this experiment, the charge is equal to the atomic number of the fragment.

The next required step is to disentangle the momentum and charge of the fragment. By placing a wedge in the beam line at the image 2 position, the fragments are slowed down according to the Bethe formula [Dem04]

$$-\frac{\mathrm{d}E}{\mathrm{d}x} = \frac{Z^2 e^4 n_\mathrm{e}}{4\pi\epsilon_0^2 v^2 m_\mathrm{e}}\left[\ln\frac{2m_\mathrm{e}v^2}{\langle E_\mathrm{b}\rangle} - \ln\left(1-\beta^2\right) - \beta^2\right]. \tag{7.2}$$

With this, the energy loss of the fragments is proportional to Z^2, which allows to separate the fragments according to their charge, and thus, atomic number. The shape of the wedge is thereby chosen such that fragments with a larger momentum encounter more material and are thus slowed down more, thus, improving the momentum spread of the beam. After the wedge, the beam is refocussed with the second pair of dipoles. Setting these dipoles to the expected rigidity for the isotope of interest after the wedge allows to deliver a secondary beam containing a specific isotope. In general this isotope is accompanied by other isotopes with similar rigidities. To allow for an event by event identification, the focal plane of the A1900 contains the extended focal plane scintillator (XFP), which is used for time of flight (TOF) measurements from the secondary beam. For the experiment in this thesis, the A1900 realized a secondary ^{24}F beam with an energy of approximately 95 AMeV and a purity of approximately 95%, which was delivered to the experimental setup in the S3 vault.

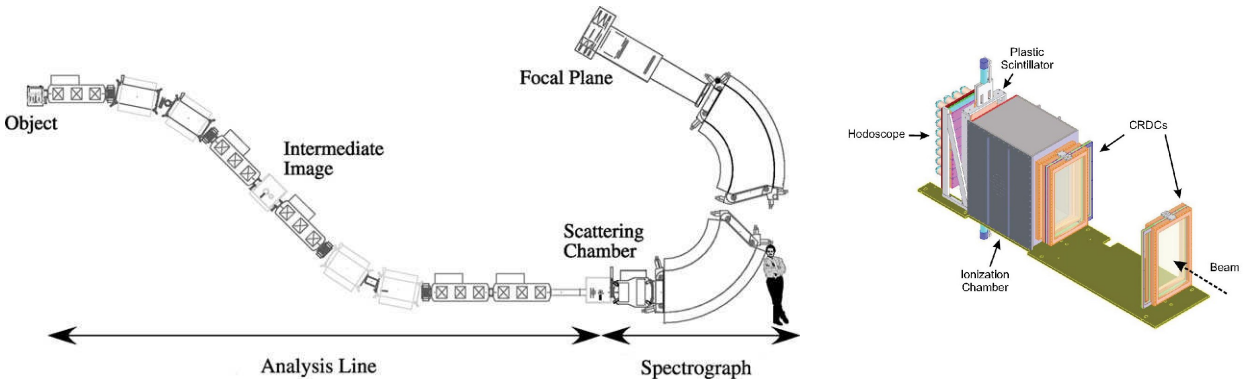

Figure 7.2: Sketch of the S800 (left) and its focal plane detectors (right). [BCS03]

7.2 S800 Spectrograph

The S800 [BCS03] is a large acceptance spectrograph, used to identify and track the fragments, which are produced in the secondary target. It consists of two parts, the analysis line and the spectrograph, as depicted in Figure 7.2.

The analysis line starts at the object position and continues down to the target station, where the scattering chamber is located. In principle it provides the possibility to use tracking detectors at the intermediate image station to track the incoming fragments, while minimizing or even rejecting the background from reactions in these tracking detectors. However, these detectors were not used in this experiment. The analysis line can be operated in two different optical modes. In focus mode, the analysis line is achromatic, which allows for the largest momentum acceptance of ±2%, but the energy resolution is reduced to about 10^{-4}. In dispersion matching mode, the whole S800 is tuned such that it is achromatic. This reduces the momentum acceptance to ±0.5%, while allowing for an energy resolution of up to 2×10^{-5}.

The spectrograph can be rotated from 0° to 60° and provides an angular coverage of 20 msr and a momentum acceptance of 5%. The key components of the spectrograph are the dipole magnets and the focal plane detectors, which, in combination, allow to measure the momentum of the fragments. A detailed introduction to each of the focal plane detectors is given in the following subsections. In addition to the information provided from the focal plane detectors, the momentum tracking and the correction for aberrations relies on the ion optics code COSY Infinity [BJN93].

In the end, the S800 provides an event by event tracking of the detected fragments. This includes the deviation of the fragment momentum from the nominal momentum, which translates to the velocity of the fragment. Furthermore, the fragment can be tracked back to the target, providing information about the position y_{ta} and angle α_{ta} in the non-dispersive plane. However, the position x_{ta} and angle β_{ta} in the dispersive plane cannot be determined.

7.2.1 Timing Scintillators

To measure the TOF, the S800 has a plastic scintillator at the object station (OBJ) and at the focal plane station (E1). The scintillators have thicknesses ranging from 100 μm to around 5 mm, depending on the charge of the beam. Charged particles passing through these scintillators will produce scintillation light, which will be detected with photomultipliers. The achievable

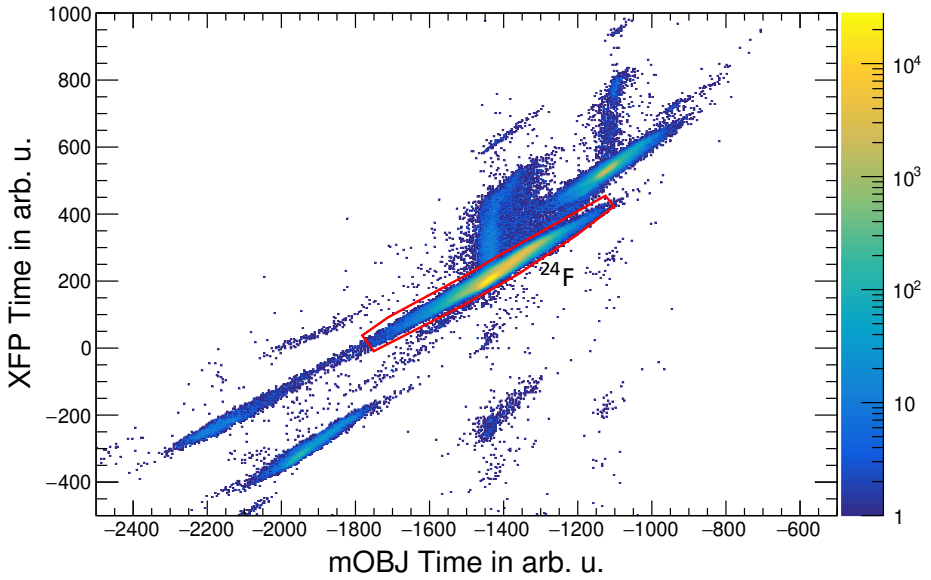

Figure 7.3: Incoming PID plot for TO_2 data in coincidence with a detected γ ray in GRETINA. The TOF from XFP to E1 is plotted over the TOF from OBJ to E1. The incoming cut used for ^{24}F is shown in red.

time resolution is about 100 ps for a point-like beam, while degrading down to 1 ns in case of a full illumination of the focal plane, though part of this can be recovered with the tracking information.

E1 provides the main trigger for the data aquisition (DAQ) of the S800 and the additional detector systems. Together with the timing signal from the A1900's focal plane and the Radio Frequency (RF) of the cyclotrons, various TOFs can be calculated. These TOFs are used for an event by event particle identification (PID) of the incoming and outgoing fragments. For the incoming PID, the TOF between XFP and OBJ are used, as shown in Figure 7.3 for TO_2. Hereby, mOBJ denotes the corresponding timing, which has been read out with Mesytec electronics. Fragments with the same TOF are found along diagonal lines in this plot. Especially in this case, where the purity of the secondary beam is very high, this provides a sufficient PID of the incoming ^{24}F.

For the outgoing PID the TOF between OBJ and E1 is used. However, depending on the reaction in the target and the thereby induced change in momentum, the flight path through the S800's dipole magnets changes significantly. Therefore, the outgoing TOF has to be corrected for the trajectory of the outgoing fragment. The top row in Figure 7.4 shows the correlations between the TOF and the position on the S800 focal plane X_{FP}, as well as the incident angle A_{FP} for TO_2. For both coordinates, one can see that larger values lead to larger TOFs. To correct for this, a linear correlation factor is applied to the TOF according to

$$\mathrm{TOF}_{\mathrm{corr}} = \mathrm{TOF} + C_{\mathrm{A}} \times A_{\mathrm{FP}} + C_{\mathrm{X}} \times X_{\mathrm{FP}}. \tag{7.3}$$

The factors C_{A} and C_{X} are thereby chosen such that they eliminate the correlation, resulting in $C_{\mathrm{A}} = 1.61\,\mathrm{ch\,mrad^{-1}}$ and $C_{\mathrm{X}} = 0.1566\,\mathrm{ch\,mm^{-1}}$. The resulting corrected TOF no longer shows a correlation, as can be seen in the bottom row of Figure 7.4.

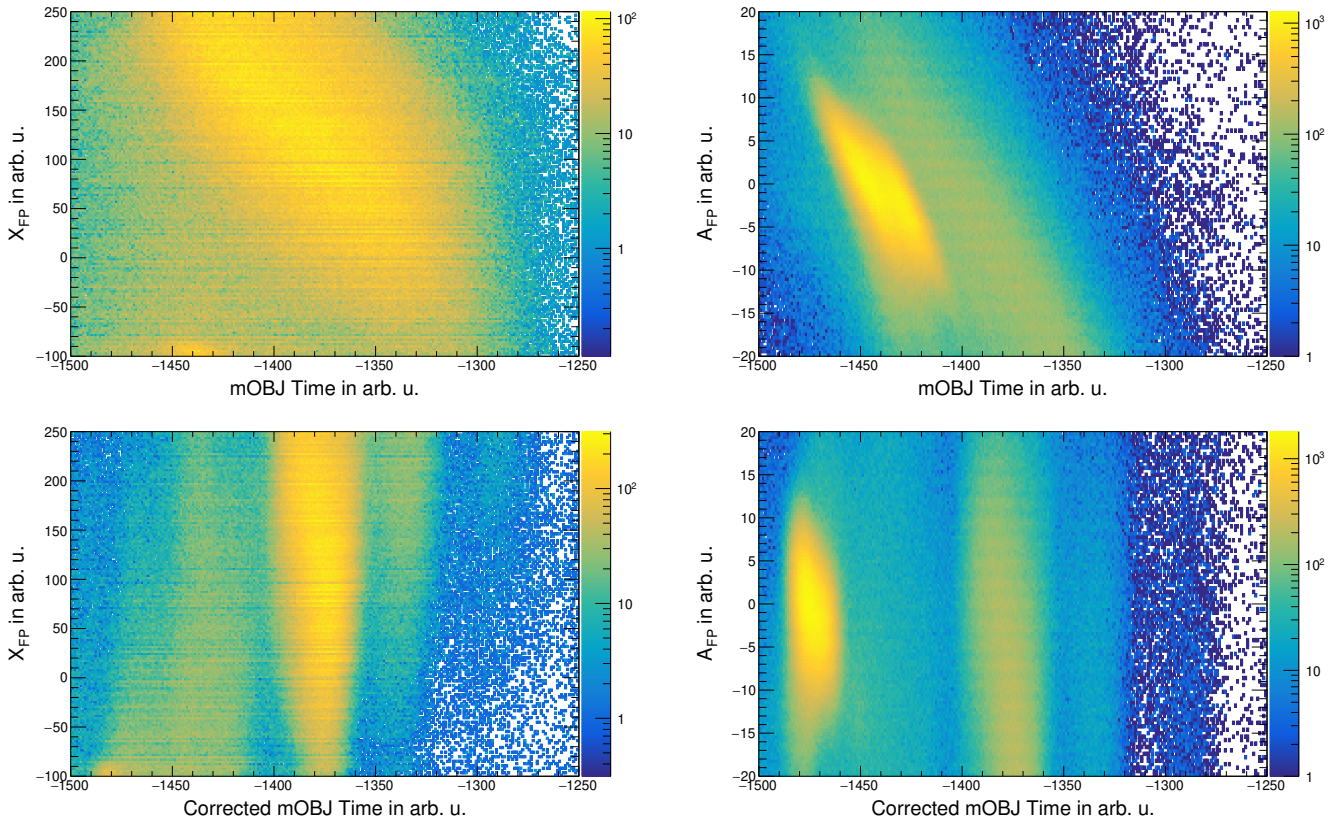

Figure 7.4: TOF correlations with the dispersive position X_{FP} and incident angle A_{FP} at the S800 focal plane. The top row shows the uncorrected data with a clear correlation for both, position and angle. The bottom row shows the data after applying the correction.

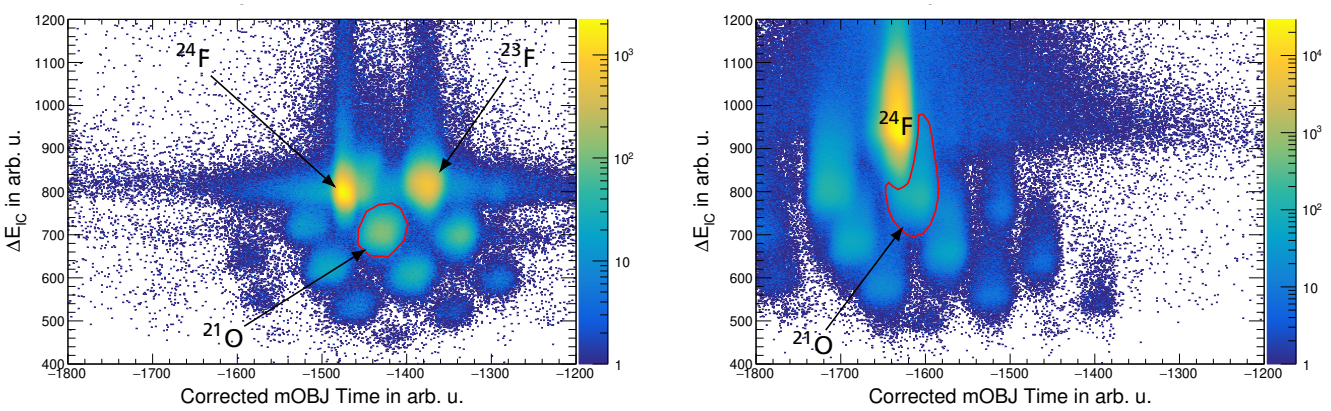

Figure 7.5: Outgoing PID plot for TO_2 (left) and DS45 (right). The energy loss in the IC is plotted against the TOF from OBJ to E1 for incoming ^{24}F coincident with a γ ray in GRETINA. The cuts used to select ^{21}O are shown in red. For TO_2 the PID shows fairly spherical and well separated accumulations. For DS45, the energy loss in the IC is washed out towards higher energy loss. This is a consequence of the increased beam rate, leading to pileup in the IC. Due to a change in the settings of the S800, ^{23}F is no longer in the acceptance for the runs with the degrader.

7.2.2 Ionization Chamber

An ionization chamber (IC) in front of the scintillators is used to measure the charge of the fragments. It is built from a set of 16 gas filled parallel-plate ion chambers. Fragments passing through the IC ionize the gas. The produced electrons and ions are collected at the anodes and cathodes, respectively. The number of electrons produced is thereby proportional to the energy deposited in the IC, which, according to the Bethe formula (c.f. 7.2), is proportional to the square of the charge Z of the fragment. Thus, the energy loss in the IC provides a direct measurement of the fragment's charge, and thus, atomic number. For an optimal performance, this energy loss has to be corrected for the different flight paths through the IC, depending on the trajectory of the fragment.

Together with the TOF measurement discussed before, this allows to identify the outgoing fragments according to their mass and charge, as shown in Figure 7.5. For TO_1 the outgoing PID shows fairly symmetric and well separated accumulations of counts. This allows for a straight forward identification of the isotope of interest, ^{21}O, and its separation from the unreacted beam, ^{24}F. On the other hand, due to the higher rates accepted during the runs with the degrader, the IC experienced a significant amount of pileup for these runs. As can be seen for DS45, this pileup smears out the PID and the accumulation of counts of ^{21}O extends into the unreacted beam. In these cases, a clear separation of the outgoing fragments is no longer possible and the shape of the graphical cut reflects the attempt of maximizing the yield of ^{21}O while minimizing the background. Furthermore, one can see that ^{23}F was no longer recorded with the settings including the degrader.

7.2.3 Cathode-Readout Drift Chamber

The fragment trajectory at the focal plane of the S800 is measured with two cathode-readout drift chambers (sCRDCs), which are sketched in Figure 7.6. This trajectory can then be used to track the fragment through the spectrograph and determine the fragment trajectory at the target position and to determine the deviation of the fragments momentum from the nominal momentum. To obtain the trajectory at the focal plane two position measurements are performed, for which the CRDCs are used. The first CRDC is located at the nominal optical focal plane of the spectrograph, the second one is located 1 m further downstream. Each CRDC is basically a gas filled chamber with an anode wire running along the edge of the chamber. The anode wire runs through 224 cathode pads, which have a pitch of 2.54 mm and allow for a position dependent charge detection. The gas in the CRDCs gets ionized by a passing fragment and the produced electrons are collected at the anode wire. The cathode pads are built around the anode wire such that the electrons induce a positive charge in the pads, which is read out. The position in the x direction is then determined by the pad with the largest signal, while the y direction is determined by the electron drift time. The drift time is thereby measured with respect to the trigger provided by E1.

To allow for a reliable position determination in the x direction, the gains of the different pads have to be matched. Figure 7.7 shows the effect of the gains of the pads for outgoing ^{21}O and ^{24}F isotopes for TO_2. Without the gain matching one can see significant differences between the recorded amplitudes of the pads. The gains of the pads have to be adjusted such that the maximum amplitudes for all pads are equal for all isotopes with a given charges. Ideally, this requires multiple isotopes with different charges, illuminating the whole area of the CRDCs. Especially in the case of the degrader runs, however, only two isotopes with sufficient statistics are available, ^{24}F and ^{21}O, of which only ^{21}O uniformly illuminates most of the pads. As a result, the focus for the gain matching was put on the isotope of interest, which is why the gain matching exhibits some discontinuities, especially for the unreacted beam ^{24}F.

For the calibration of the y position, two masks can be placed in front of the CRDCs. Holes and slits in the masks allow particles to pass through the masks into the CRDC and thus an image of the mask is recorded by the CRDCs. Figure 7.8 shows a sketch of the layout of the two masks and the two recorded images. The position is then calibrated with

$$y_{\text{corr}} = y \times \text{slope} + \text{offset}. \tag{7.4}$$

Table 7.1 summarizes the resulting calibration parameters for the y position.

As can be seen, these parameters have slightly changed over the course of the experiment. In fact, a slow drift in the reconstructed beam position on the target was observed over longer periods of time, as shown in Figure 7.9. This was caused by a drift in the CRDCs' position determination. Possible causes for such a drift are, e.g., changes in temperature or gas pressure in the CRDCs over time. It has been corrected for, by assuming that the position of the unreacted beam on the target stayed constant during the experiment. By fitting the position of the unreacted beam within a given time interval, a correction factor is determined. Afterwards, it is applied to the measured position in the CRDCs for this time interval. With this correction the signals in the CRDCs, and consequently also the reconstructed position on the target, stay constant over time.

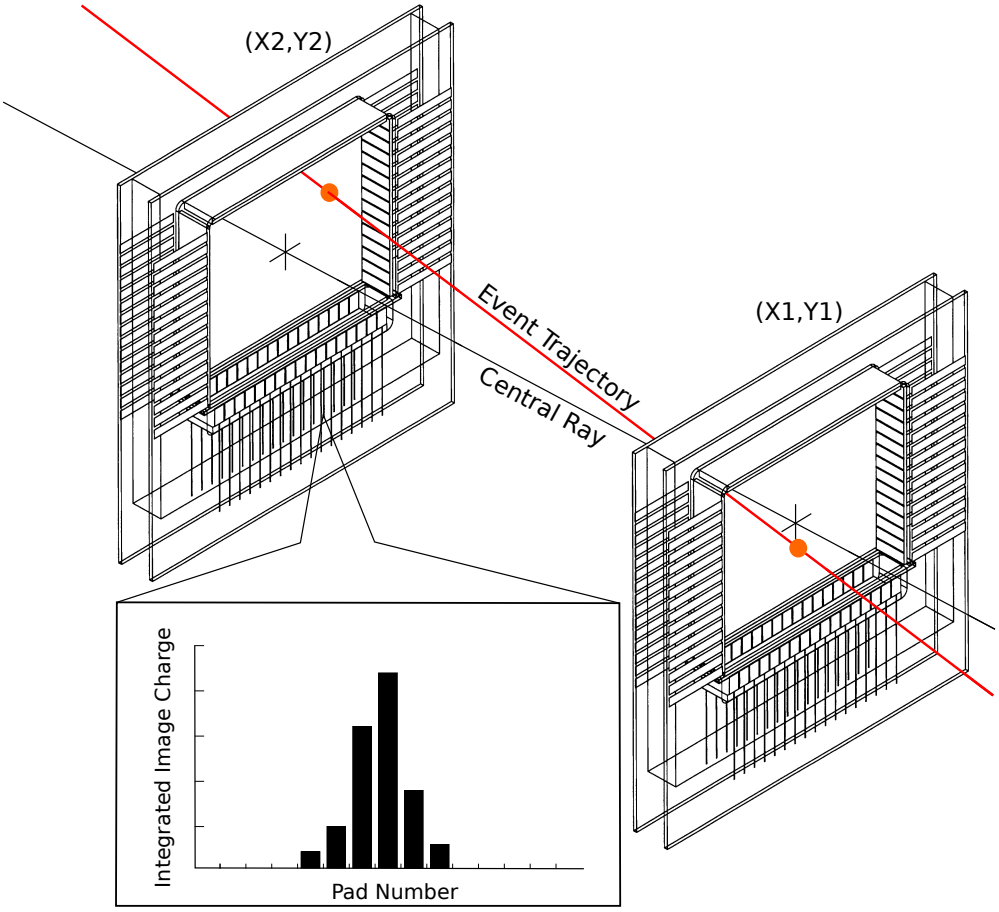

Figure 7.6: Sketch of the CRDCs at the focal plane of the S800. Fragments passing through the gas chamber produce electrons, which are detected with cathode pads. The pad with the largest signal provides the x position, while the drift time of the electrons gives the y position. The two measured positions are used to determine the trajectory of the particle at the focal plane of the S800. The picture is adopted from [S8018].

Table 7.1: Calibration parameters for the position measurements of the CRDCs from mask measurements.

	slope in mm ch^{-1}		offset in mm	
	$CRDC_1$	$CRDC_2$	$CRDC_1$	$CRDC_2$
$TO_{1,2}$	−0.1683	0.1707	97.84	−103.46
$DS25_1$	−0.1814	0.1814	100.08	−106.36
$DS25_2$	−0.1696	0.1673	105.86	−110.34
DS45	−0.1767	0.1739	103.27	−106.88

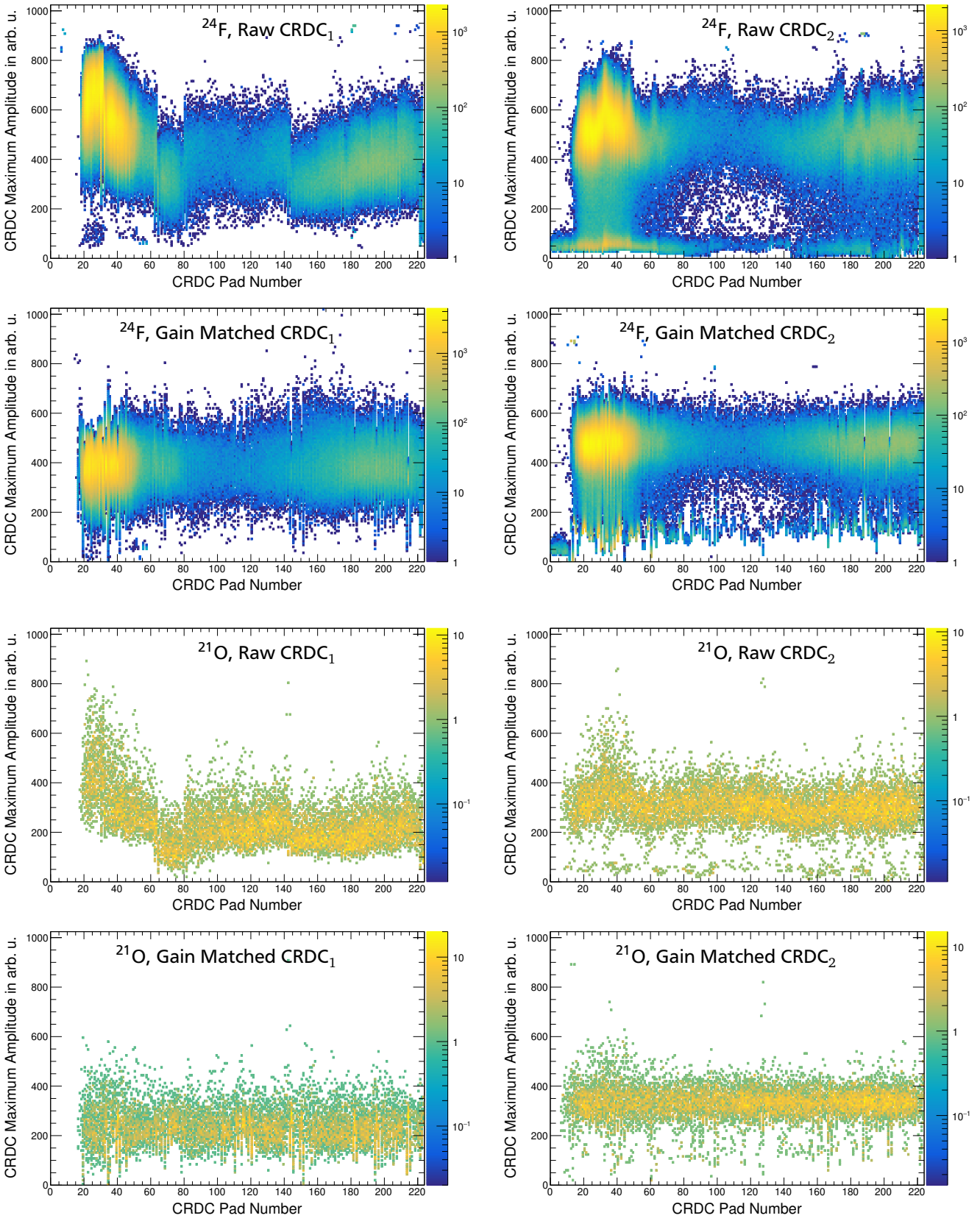

Figure 7.7: Gain matching of the CRDCs. The maximum amplitude recorded in an event is plotted over the corresponding pad number for outgoing ^{24}F and ^{21}O, each with and without the gain matching.

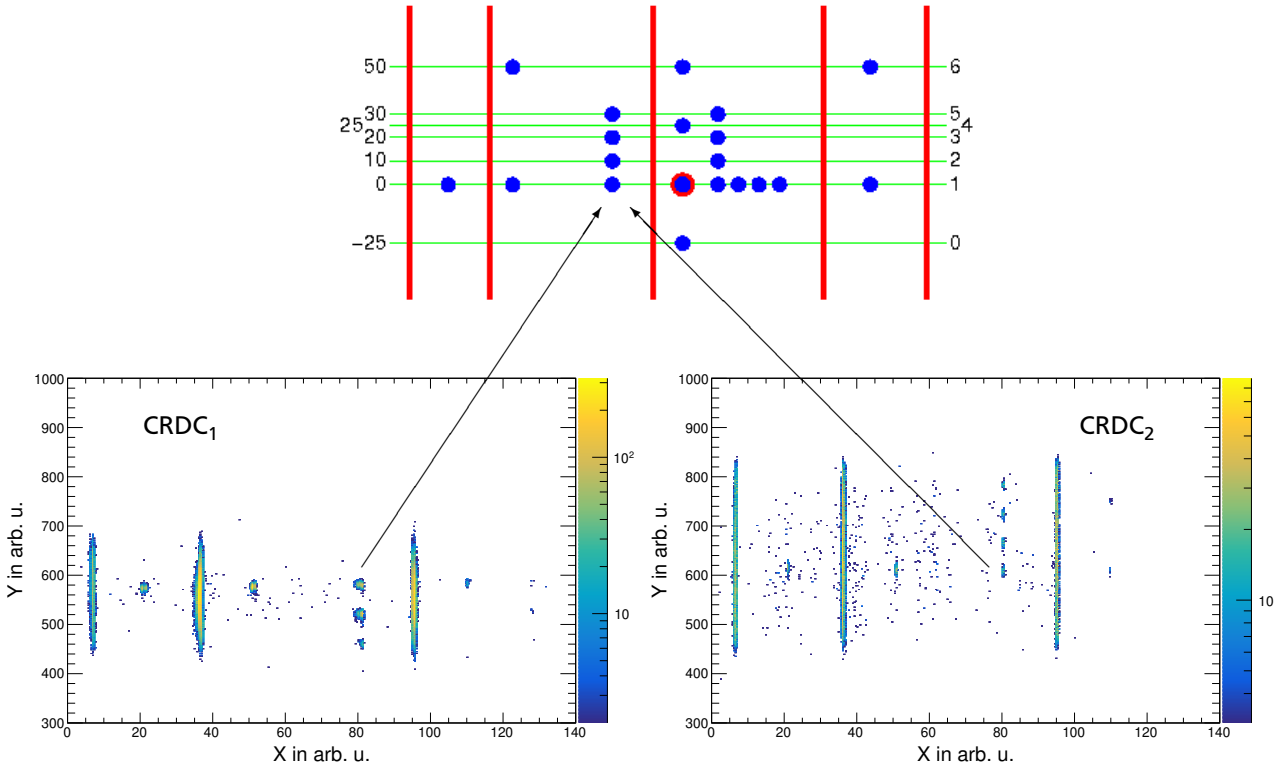

Figure 7.8: Mask calibration of the CRDCs. The top shows a sketch of the masks used for the calibration. The red slits and blue holes allow particles to pass through the mask and thus produce an image in the CRDCs. The bottom row shows the recorded images for both CRDCs. The calibration parameters are then determined by matching the recorded pattern with the known geometry of the masks.

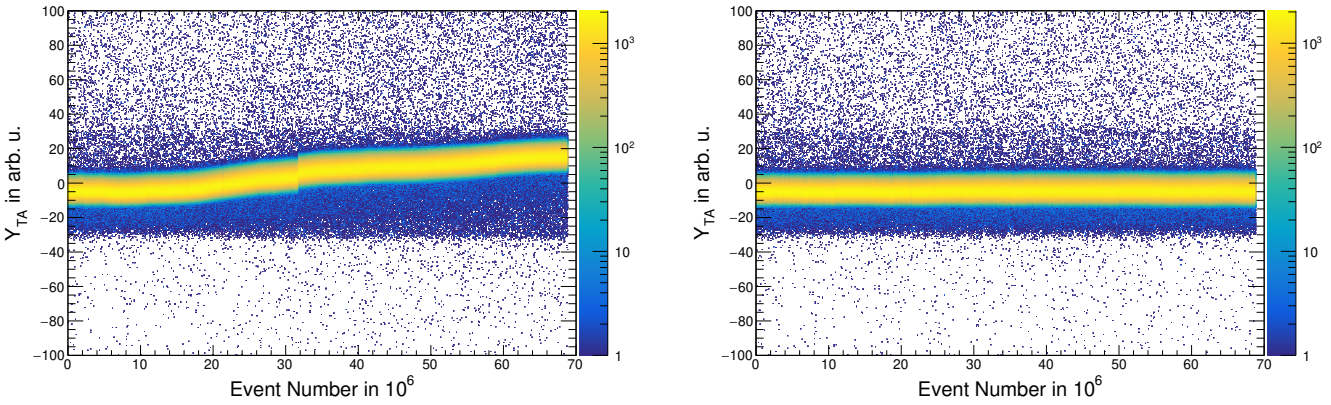

Figure 7.9: Reconstructed beam position on the target plotted over the event number, and thus, over time. The left figure shows the reconstructed y position on the target, without a correction for the drift in the CRDCs, over the course of approximately 24 hours. The right figure shows the same after applying the correction.

7.3 GRETINA

Since the goal of the experiment is the determination of the lifetime of an excited state in ^{21}O, the detection of the γ rays produced by the deexcitation of this excited state is critical. For the detection of these γ rays, GRETINA [LCC04, PLM13, WBB17] is used, which is a Compton tracking array (CTA) built from HPGe detectors. The basics of HPGe detectors and CTAs are covered in Section 2.1 and Section 2.2.

For the experiment presented in this thesis, nine GRETINA detectors were available, each consisting of four HPGe crystals. With these detectors, GRETINA covers approximately 1.2π sr of solid angle. GRETINA is approximately centred around the pivot point of the S800 and the distance of the detector surface was about 20 cm away from the nominal target position. Figure 7.10 shows a picture of GRETINA surrounding the beam pipe. The actual target position is shifted upstream by 13 cm, as is explained in Section 7.4. With respect to the beam axis and shifted target position, four detectors are placed at an angle of about 40° and five detectors at 60°. Lead plates are taped onto the front faces of the detectors as shielding, to reduce the rate due to low energy γ rays produced during the experiment.

Measurements with a ^{152}Eu and a ^{56}Co source were performed with various positions and arrangements of the sources for energy and efficiency calibrations. Figure 7.11 shows two of the measured spectra from these source measurements. With this, the energy calibration of GRETINA is done, resulting in a precision of mostly better than 0.2%, as can be seen in Figure 7.12. The efficiency calibration, however, is only partly possible. Since the scalars were not recorded reliably during the experiment, only the relative efficiency is accessible. As such, especially the comparison to simulation is of importance. Therefore, the efficiency calibration is further discussed in Section 8.1.

One of the goals of the experiment is to determine the branching ratio of the $3/2^+ \rightarrow 1/2^+$ transition at 900.5 keV. However, this transition lies close in energy to the $5/2^+ \rightarrow 3/2^+$ transition at 876 keV, which is significantly more intense. As such, it is important to optimize the energy resolution to be able to separate these two transitions. Since the resolution is dominated by the Doppler correction, c.f. Section 7.5, the detection angle is crucial for improving the resolution. Therefore, the tracking capabilities of GRETINA are used to determine the first interaction point of the detected γ rays in the detector. The effect is most significant for the intensity of the high energy transitions at 3 MeV, but also at low energies it improves the angular resolution for the Doppler correction and increases the overall peak-to-background ratio. A comparison of the resulting γ-ray spectra with and without the tracking for TO_2 is shown in Figure 7.13 and summarized in Table 7.2. With these resolutions, the separation between the two transitions is above 3σ for TO_2, which is sufficient to separate the two peaks. For the settings with the degrader the resolution does not allow to clearly separate the two peaks, however, the shape of the peak still allows to infer the different contributions.

7.4 TRIPLEX Plunger Setup

For the accurate and precise positioning of the target and degrader, the TRIPLEX [IDB16] was used. It has mounting structures for up to three foils, two of which are movable while the position of the mounting structure in the middle is fixed. Since only two foils were used in this experiment, the ^{9}Be target and the ^{181}Ta degrader, they were mounted on the two movable

Table 7.2: Resolution and peak-to-background ratio with and without γ-ray tracking for TO_2 for different γ-ray transitions.

Peak Energy	876 keV		1844 keV		2122 keV	
	σ in keV	P/B	σ in keV	P/B	σ in keV	P/B
Non-Tracked	8.0 ± 0.9	0.83 ± 0.07	14.2 ± 1.7	0.65 ± 0.06	15.6 ± 1.0	1.60 ± 0.09
Tracked	7.1 ± 0.6	1.46 ± 0.09	11.8 ± 0.8	1.40 ± 0.09	13.8 ± 0.5	3.25 ± 0.12

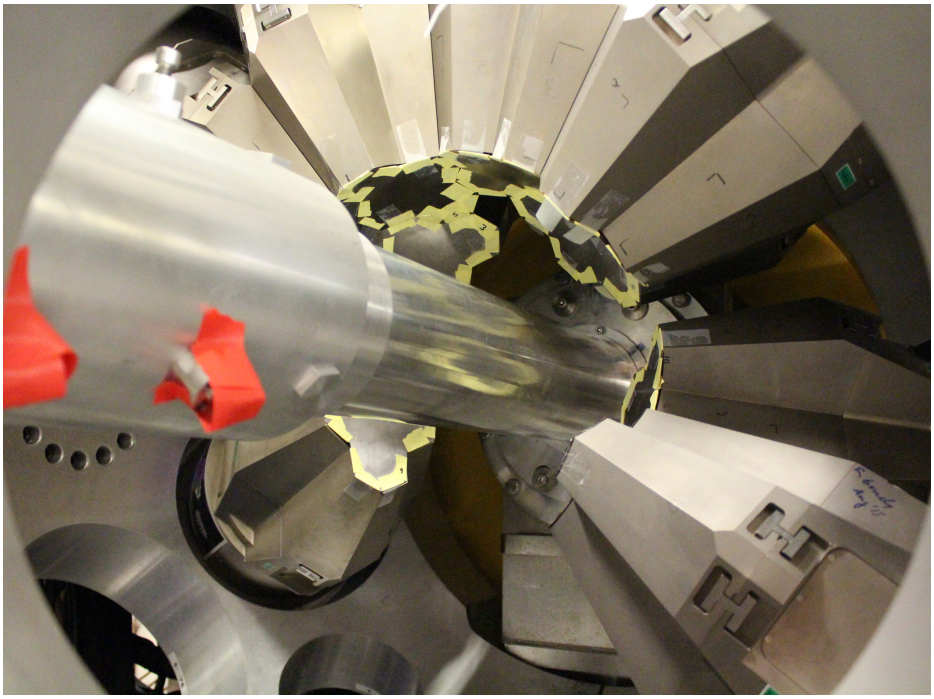

Figure 7.10: Picture from the experiment of GRETINA surrounding the beam pipe. Lead plates are taped to the front of the detectors with yellow tape.

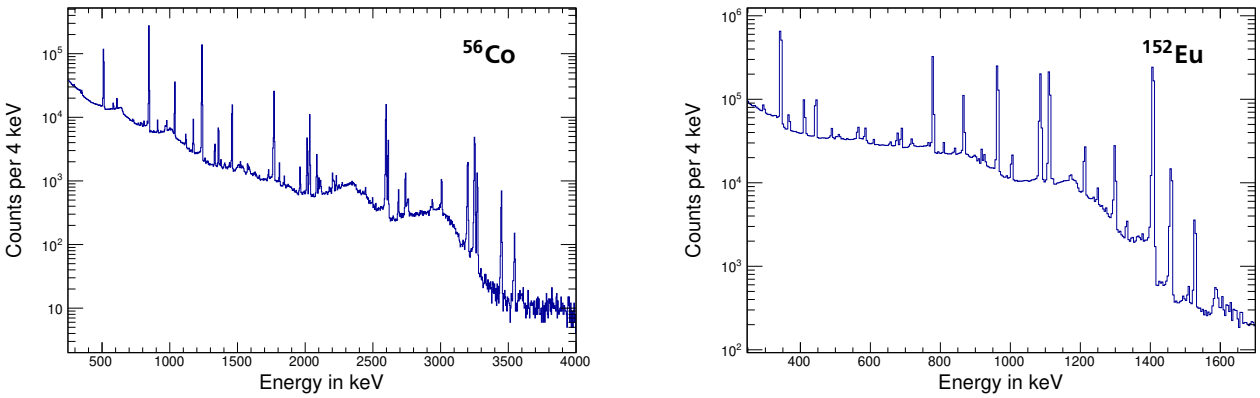

Figure 7.11: Calibration measurements for GRETINA with a ^{56}Co (left) and a ^{152}Eu (right) source.

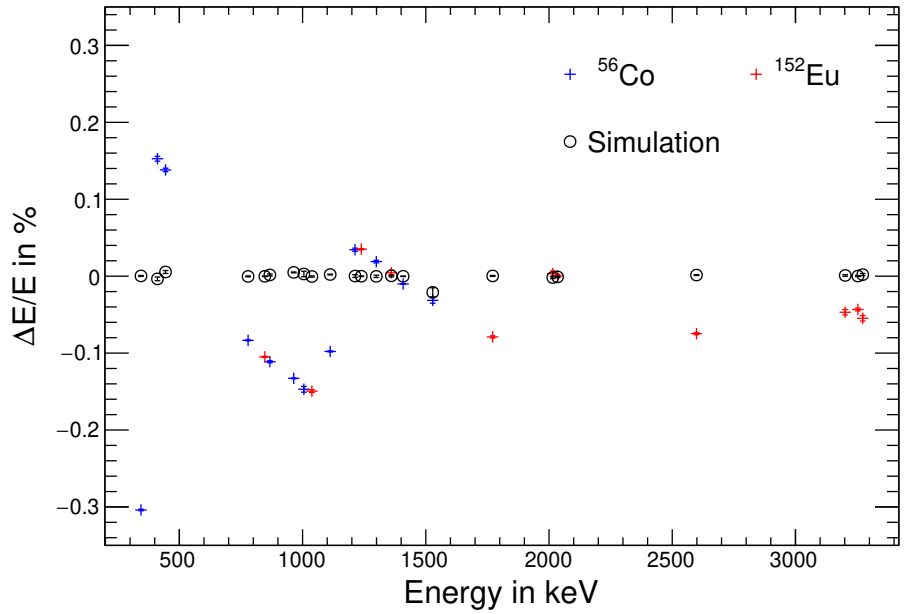

Figure 7.12: Energy calibration of GRETINA with ^{56}Co and ^{152}Eu. The relative deviation of the measured energy from the expected energy is plotted over the expected energy. For most of the data the measured energy is within 0.2 % of the expected energy.

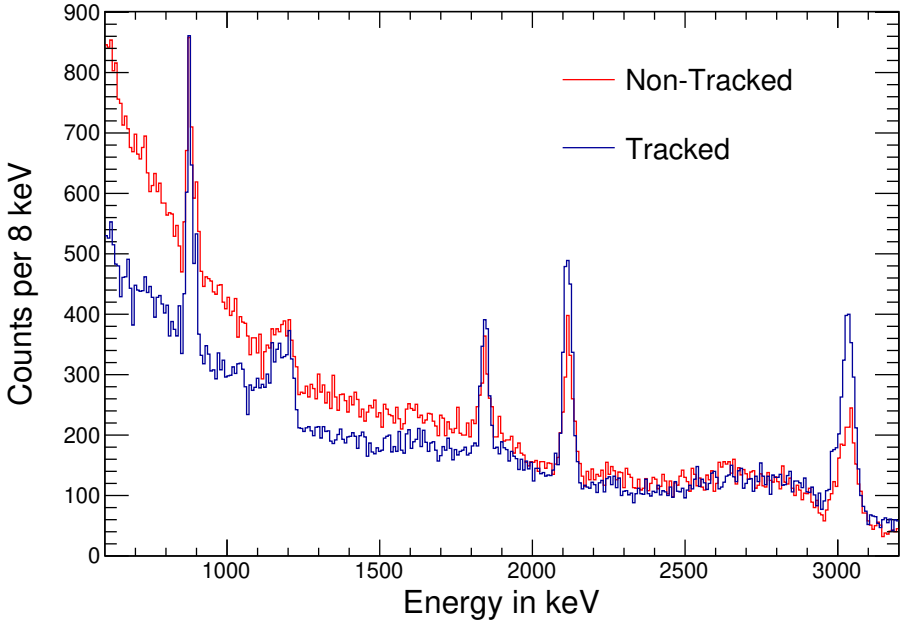

Figure 7.13: Comparison of non-tracked and tracked spectra for ^{21}O and TO_2. The resolution is slightly improved in the tracked spectrum. The peak-to-background ratio is also improved, especially for large energies.

structures. This way the degrader could be moved up to 25 mm downstream from the central position, which is the nominal position of the target. Furthermore, the target could be moved upstream by 20 mm, giving a total target-degrader separation of 45 mm. While by design the movable range of the target is also 25 mm, technical problems with the linear actuator could have led to the target getting stuck if moved beyond 20 mm. Since it was planned to return to a target-degrader separation of 25 mm after the 45 mm measurement, a stuck target would have involved venting the target chamber, opening the beam line, and repairing the TRIPLEX. As such, the potential loss of multiple hours of beam time outweighed any possible gain from the increased separation.

The distances by which the foils are moved can be measured via linear encoders. Since this only provides a relative measure of the movement, the system is calibrated with a capacitance measurement to determine the absolute distance between the foils at small distances.

Finally, the TRIPLEX is moved 13 cm upstream from the nominal target position of the S800. This configuration enhances the sensitivity of the RDM setup, since the GRETINA detectors are moved further towards forward angles. This increases the influence of the Doppler shift, and thus, the separation of the slow and fast peaks in the energy spectrum.

7.5 Doppler Correction

In this experiment, the γ rays are emitted while the fragments are in flight. As such, the detected γ rays are Doppler shifted according to their emission angle Θ and the velocity of the emitting fragment. To determine the energy of the detected γ rays in the rest frame of the fragment and with this, the energy of the corresponding transition, the detected energies need to be Doppler corrected. For this, it is required to know the momentum and the position of the fragments at the time of decay, where the momentum can be expressed by the fragment's velocity β and its direction of movement.

The position at the time of the decay, of course, cannot be determined with the given setup. Instead, it has to be assumed to have taken place at either the target or the degrader. Focussing the Doppler correction on the target will result in a better resolution for the peaks originating from the target and vice versa. Especially for experiments with short lifetimes and therefore small slow components, it can be critical to focus on the degrader to enhance the slow component. However, in this experiment, the lifetime is such that the slow and fast component are of comparable size. Since none but the first excited state exhibit a significant lifetime, no slow components other than those caused by reactions in the degrader are expected for the remaining transitions. Therefore, focussing on the target even for the measurements with the degrader, allows to use all peaks to determine the parameters for the Doppler correction.

The beam energy provided by the A1900 allows for a good estimation of β. However, the acceptance of the S800 can significantly influence the average detected β, as can be seen in Figure 8.3. The S800 itself measures deviations from the nominal momentum, which then allows to correct the fragment's momentum on an event by event basis. To determine the nominal momentum, the high position sensitivity and energy resolution of GRETINA is used to directly determine the beam's β, together with y_{ta} and α_{ta}. Given the correct beam parameters, the Doppler corrected energy is independent of the angle under which the γ ray was detected, while the energy resolution is minimal, and the energies of the peaks match the expected rest frame energies. If β is wrong, it results in a clear correlation between the Doppler corrected energy and the detection angle Θ. Similarly, if y_{ta} or α_{ta} are incorrect, a distinct correlation is

Table 7.3: Beam parameters determined by eliminating correlations and optimizing the resolution of the Doppler correction.

	β	α_{ta} in mrad	y_{ta} in mm
TO_1	0.4163	−6.2	3.1
TO_2	0.4102	−6.3	6.1
$DS25_{1,2}$ DS45	0.4153	−11.0	3.3

visible between the energy and the angle Φ. Figure 7.14 illustrates these correlations for the aforementioned cases, as well as the results after the determination of the beam parameters for TO_2, which no longer show any correlation.

The only reliably known energy is the energy of the first excited state, which, due to its lifetime, does not provide a significant constraint. Instead, the energy difference of the two peaks at 2122 keV and 900.5 keV is used as a point of reference, though, the potential lifetime of the respective state will lead to a systematic uncertainty. The resulting parameters after eliminating the correlations and optimizing the resolution are summarized in Table 7.3. While the beam was retuned after TO_1 and the settings for the S800 were significantly changed after TO_2, the setup stayed basically unchanged for the remaining measurements with the degrader. Therefore only one set of parameters is used for the measurements with degrader.

In principle, an additional degree of freedom is given by the position of the target along the beam axis. By adjusting the target position and β accordingly, it is possible to also remove the correlations and, as a result, shift all detected energies by a common factor. However, the level scheme limits such shifts, as the energies of the different transitions have to add up consistently. Furthermore, the required shifts in the target position of $\approx$5 mm to mitigate some of the systematic offsets in the measured energies, further discussed in Section 7.6, are unreasonable. Similarly, the modified β becomes incompatible with the beam energy delivered by the A1900 and the expected energy loss in the target. In addition, it would also shift the low energy transitions to higher energies, and as such introduce a new discrepancy.

7.6 Resulting γ-Ray Spectra

With the fully characterized setup, the resulting spectra are presented in the following. The Doppler corrected γ-ray spectra of ^{21}O are shown in Figure 7.15, with the Doppler correction being focussed on the target for all settings. The settings with the degrader contain a significantly increased background compared to the settings without the degrader, due to the additional material in the beam. Furthermore, the energy resolution is worse for the settings with the degrader, since the precision of the S800 to determine the momentum of the ^{21}O at the target position is reduced by the straggling in the degrader. Therefore, the Doppler correction is less precise, which increases the energy resolution. Figure 7.16 shows a detailed view of the peaks of interest for TO_2, which provides the best resolution and statistics, with a clear separation of the two peaks at 900 keV and the distinct, long tail to lower energies of the peak at 1221.5 keV. The observed intensities and line shapes in these spectra will be the basis for the later analysis, for which, especially in the context of the line shapes, the details of the background are relevant.

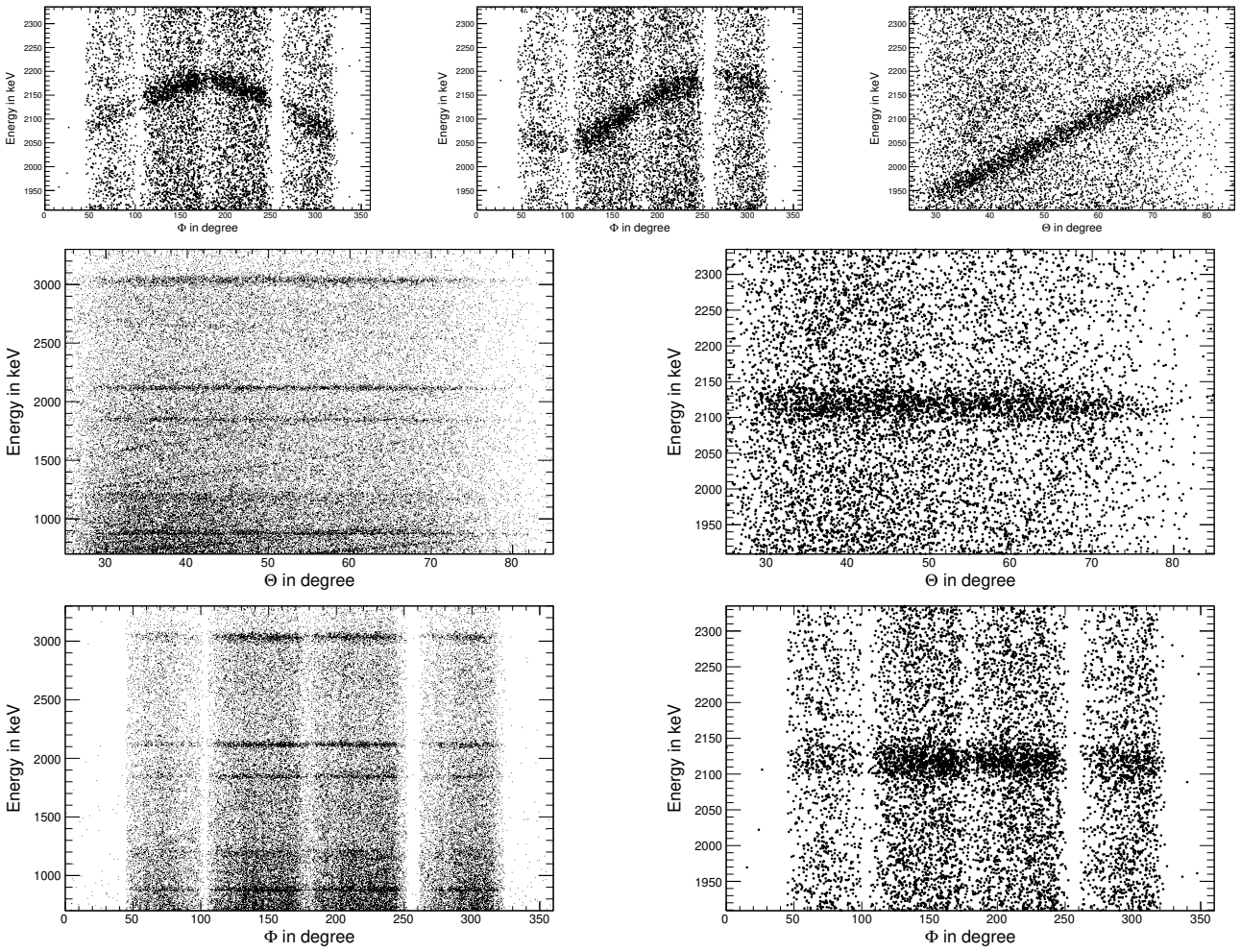

Figure 7.14: The Doppler corrected energies for the outgoing ^{21}O fragments, plotted against the angles Θ and Φ under which the γ rays have been detected for TO_2. The top row illustrates the correlations if the beam parameters α_{ta}, y_{ta}, and β are not set correctly (from left to right). The remaining figures show the results with the correct parameters for the full energy range (left) and a zoom onto the 2122 keV transition (right).

Thus, to further characterize the background, Figure 7.17 shows the measured γ-ray spectra in the laboratory frame with a cut on ^{21}O. The peaks visible in the background spectra are primarily produced by neutron induced reactions, foremost by inelastic scattering on germanium and aluminium. The neutrons are produced by reactions of the ^{24}F beam in the target and degrader, for example by the reaction of interest, producing ^{21}O. Aluminium is ever-present in the experimental setup, e.g., in the beam pipe, holding structures, or casings. germanium in turn is the detector material itself, which leads to the peculiar sawtooth-shape of the corresponding peaks, since not only the energy of the transition is measured, but also the kinetic energy of the recoiling germanium [FMP96]. In the Doppler corrected spectra, however, these peaks are completely smeared out, masking all such features, leaving only a very broad structure in the background. Nonetheless, these peaks need to be included in the simulations to correctly reproduce the shape of the background.

The energies of the observed transitions and states are listed in Table 7.4. The statistical uncertainties are obtained from Gaussian fits to the recorded TO_2 spectrum. The uncertainty of the energy of the first excited state ($1/2^+$) of 2.2 keV translates into a systematic uncertainty (sys_E) for all other states, since this energy has been used as a reference energy for the Doppler correction. Similarly, any potential lifetime, and thus centroid shift, of the second excited state ($3/2^+$) leads to a systematic uncertainty (sys_τ) in the determined energies, since its transitions were used for optimizing the Doppler correction. Furthermore, this uncertainty (sys_τ) includes the influence of the potential lifetimes of each respective state. The energies of the higher lying transitions thereby show a systematic deviation between 10 keV and 40 keV from the values reported before [SAD04]. Despite an extensive search for possible causes of a systematic error in the γ-ray energy, no problems were found. Neither the calibration of GRETINA, nor the Doppler correction by modifying the target position or beam properties, can account for the observed differences. As a consequence, the measured energies are taken as accurate, resulting in the level scheme as discussed in Section 6.2. It is hereby noted that a potential systematic error in the energy, as described above, does not influence the results of the lifetime and branching ratio measurements, since this systematic error would be included in the simulations as well.

Lastly, the γ-γ coincidences in Figure 7.18 allow to confirm the assumed level scheme of ^{21}O, as discussed in Section 6.2. However, due to the low solid angle coverage of GRETINA and thus the low 2γ efficiency, only the most prominent coincidences can be detected, which have already been observed [SAD04]. One can clearly see the coincidence of the 1844 and 3037 keV transitions and that it is, indeed, the higher lying of the two 3 MeV states which is populated by the 1844 keV transition. Another coincidence can be seen between the 876 and 2122 keV transitions. On the other hand, gating on 900 keV shows no significant structures, even though it is assumed to be in coincidence with the 1221.5 keV transition. However, this missing coincidence is explained by the low 2γ efficiency of the setup and the broad width of the 1221.5 keV peak. Since no other transition fits the measured energy, the assignment to the transition from the $3/2^+$ state to the $1/2^+$ state is the only conclusion. No transition of significant strength with an energy of 915 keV from the state at 3037 keV ($7/2^+$) to the state at 2122 keV ($3/2^+$) is observed (c.f. Figure 7.16), giving rise to the spin-parity assignment of the two 3 MeV states, as discussed in Section 6.2. Similarly, no significant transition with an energy of 1776.5 keV between the states at 2998 keV ($5/2^+$) and 1221.5 keV ($1/2^+$) is observed. Yet, this potential transition is included in the later analysis, since it influences the obtained branching ratios.

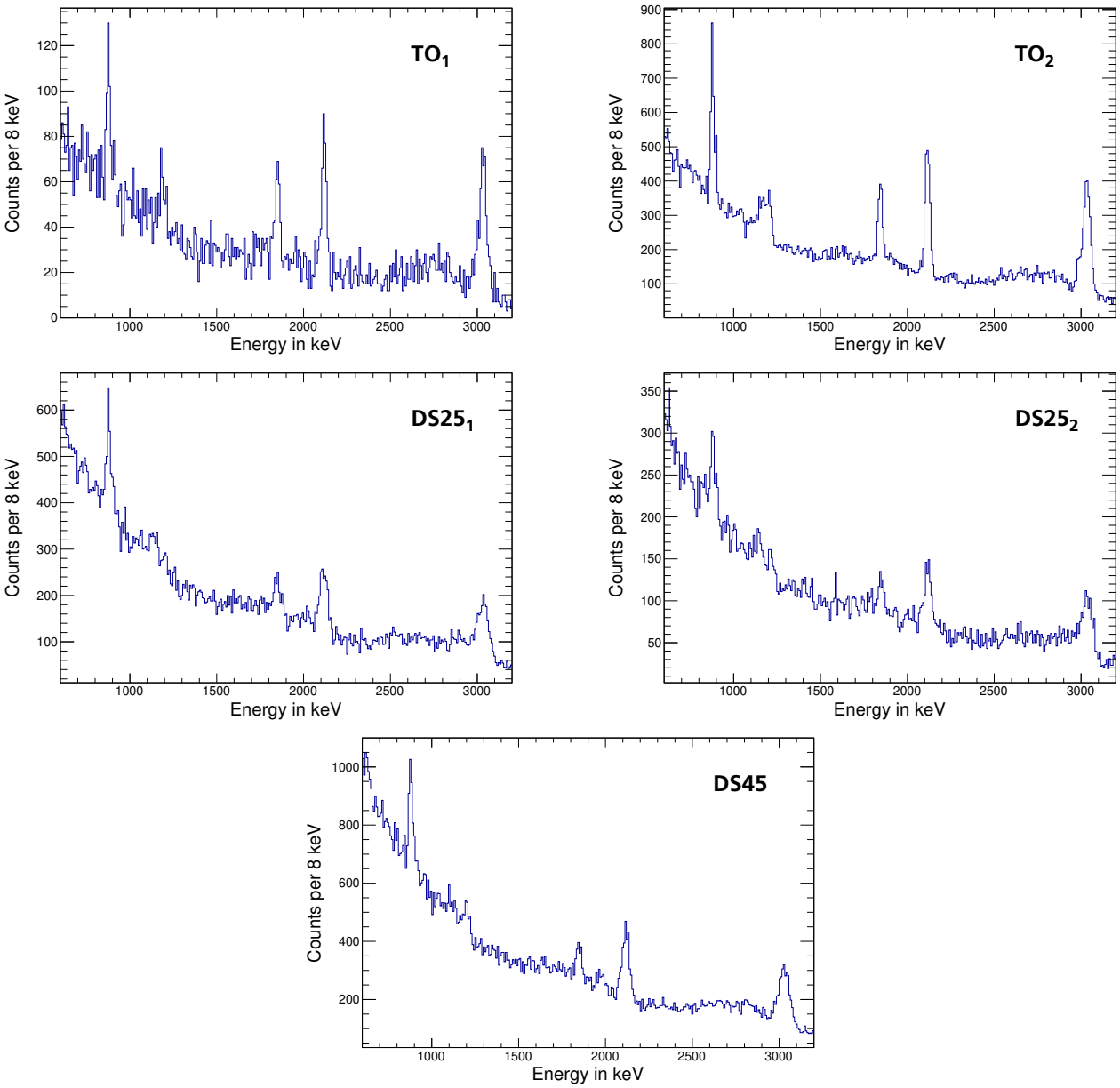

Figure 7.15: Measured, Doppler corrected γ-ray spectra of ^{21}O. The Doppler correction being focussed on the target. The settings with the degrader contain a significantly increased background due to the additional material in the beam. Also, the energy resolution is worse for the settings with the degrader, since the energy and angular straggling in the degrader reduce the precision of the S800.

Table 7.4: Summary of the measured energies of the peaks and states of ^{21}O. The statistical uncertainties are obtained from Gaussian fits to the TO_2 spectrum. The systematic uncertainties are a result of the uncertainty of the energy of the first excited state (sys_E), which is used as a reference energy, and the uncertainties due to the potential lifetimes (sys_τ) of the second excited state and the respective state itself.

Peaks in keV	
E	stat
876	± 1
900.5	± 1.0
1221.5	± 2.2
1844	± 1
2122	± 1
2998	± 5
3037	± 2

States in keV				
J^π	E	stat	sys_E	sys_τ
$1/2^+$	1221.5	± 2.2		
$3/2^+$	2122	± 0.6	± 4.0	± 5.0
$5/2^+$	2998	± 0.8	± 5.5	$^{+\ 22.5}_{-\ 7.5}$
$7/2^+$	3037	± 1.1	± 5.5	$^{+\ 22.5}_{-\ 7.5}$
$9/2^+$	4881	± 1.5	± 8.8	$^{+\ 36.2}_{-\ 12.2}$

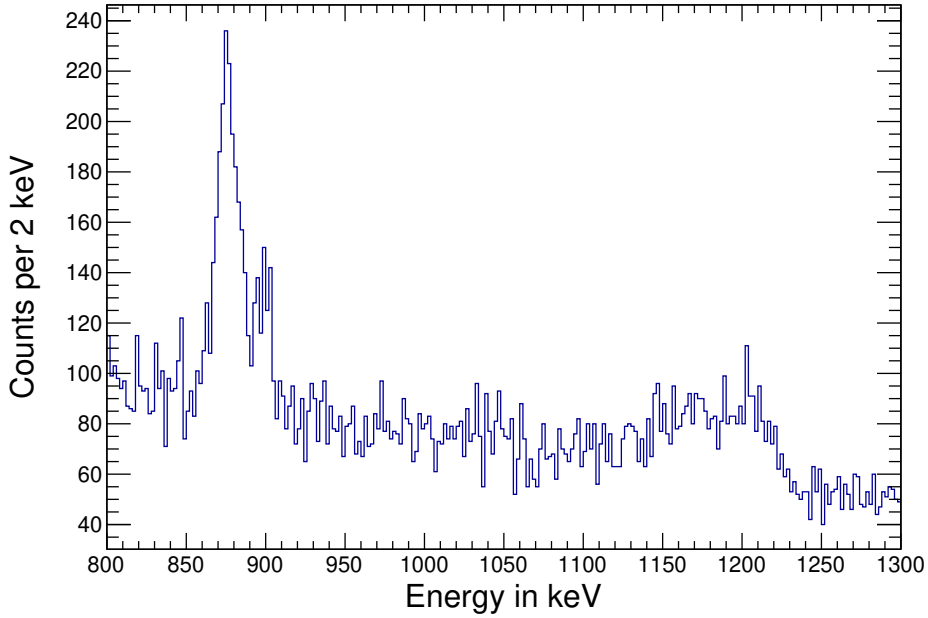

Figure 7.16: Measured, Doppler corrected γ-ray spectrum of ^{21}O for TO_2. The Doppler corrected energy is shown in the range of the peaks of interest.

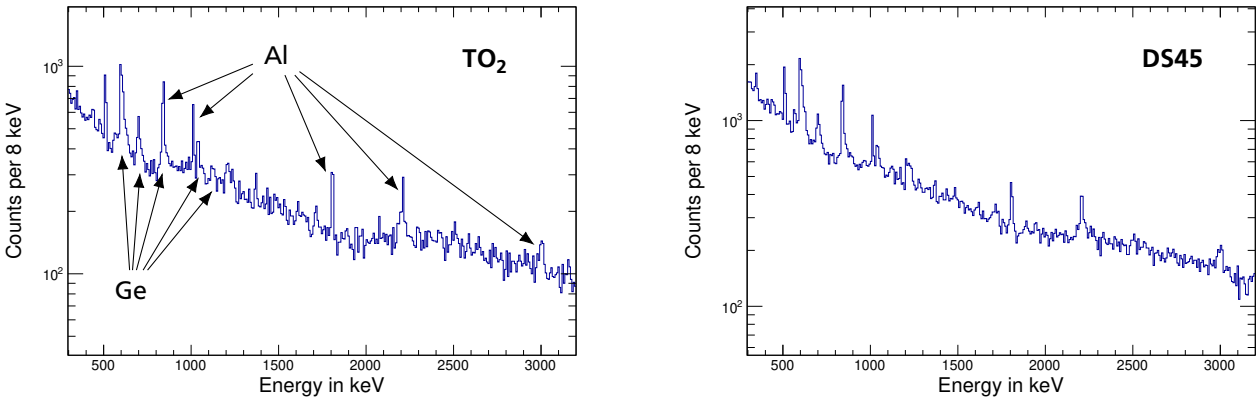

Figure 7.17: Background spectra of ^{21}O in the laboratory frame for TO_2 and DS45. They show the detected γ-ray energy without a Doppler correction. The peaks are mostly produced by neutron induced reactions on germanium and aluminium. The difference between runs with and without the degrader is negligible.

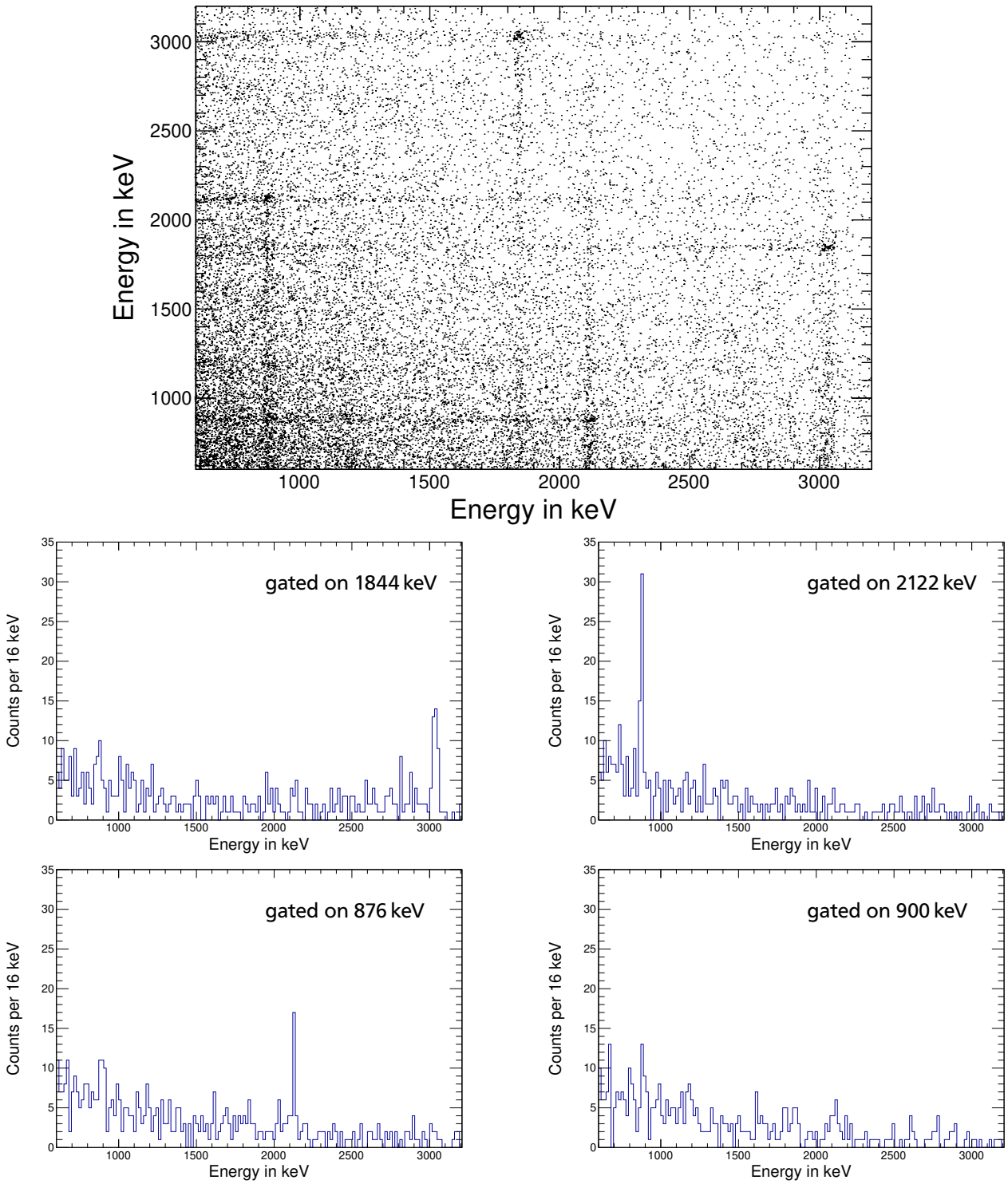

Figure 7.18: γ-γ coincidences in ^{21}O for TO_2 The top shows the γ-γ coincidence matrix. Below, the γ-ray spectra are shown for gates on the different transitions. They show clear coincidences between the 876 and 2122 keV transitions, as well as the 1844 and 3037 keV transitions. Gating on 900 keV does not show a significant coincidence, though, this is not unexpected, due to the broad width of the 1221.5 keV transition and the low statistics.

8 Analysis and Results

To determine the lifetime and branching ratios, the measured data is compared to simulations of the experimental setup. These simulations are done with an adjusted version of G4Lifetime [AEM09], which is based on Geant4. This simulation includes the geometry of GRETINA as it was used at NSCL, as well as routines to properly handle the incoming beam properties and the acceptance of the S800. However, the S800 itself is not included in the simulations. Figure 8.1 shows an image of the simulated geometry for an exemplary event with a single γ ray being emitted from a fragment while it is between the target and the degrader. The simulation can be provided with a set of transitions and lifetimes. From this it produces an output file containing the detected interactions. This output is then converted and further processed with GrROOT equivalent to the measurement data. As such, all routines used, e.g., to cluster and track the γ-ray interactions are the same for both data sets.

With this, a wide range of degrader reaction ratios and lifetimes are simulated for all relevant transitions. The resulting spectra are superimposed and normalized via fit to the measured data. Before these results are presented in Section 8.3, the simulated γ-ray efficiency and energy resolution is discussed in Section 8.1 and Section 8.2, respectively. Finally, the results for the lifetime and branching ratio are discussed and compared to the theoretical predictions in Section 8.4.

8.1 Detection Efficiency for γ-Rays

To be able to determine the correct branching ratios by comparison of the simulations to the measurement, it is important to ensure that the simulated relative efficiency matches the one of the measurement. To verify this, the two calibration sources for GRETINA, c.f. Section 7.3 and Figure 7.11, have been simulated and the measured intensities are compared to the simulations. The intensities are normalized to the 847 keV transition for the ^{56}Co source and the 867 keV transition for the ^{152}Eu source. Since these two transitions are very close in energy, this effectively also normalizes the intensities of the two sources to each other.

Figure 8.2 shows two examples of the resulting relative efficiency, one for a crystal with good agreement between simulation and measurement and one for a crystal with bad agreement. As can be seen for the crystal with good agreement, the relative efficiency of the measurement is very well reproduced by the simulation. This is especially visible by looking at the ratio of the two efficiencies, which is in agreement with 1 throughout the whole energy range. For the crystal with bad agreement, the deviation of the relative intensities is mostly occurring at energies below 800 keV. For higher energies the simulation is still in good agreement. This is indeed representative for all crystals, which show in general a very good agreement, with deviations only occurring at low energies. Since the lowest peak of interest is above 800 keV, which is then Doppler shifted towards even higher energies, this mismatch in the simulated efficiencies at low energies is not affecting the results.

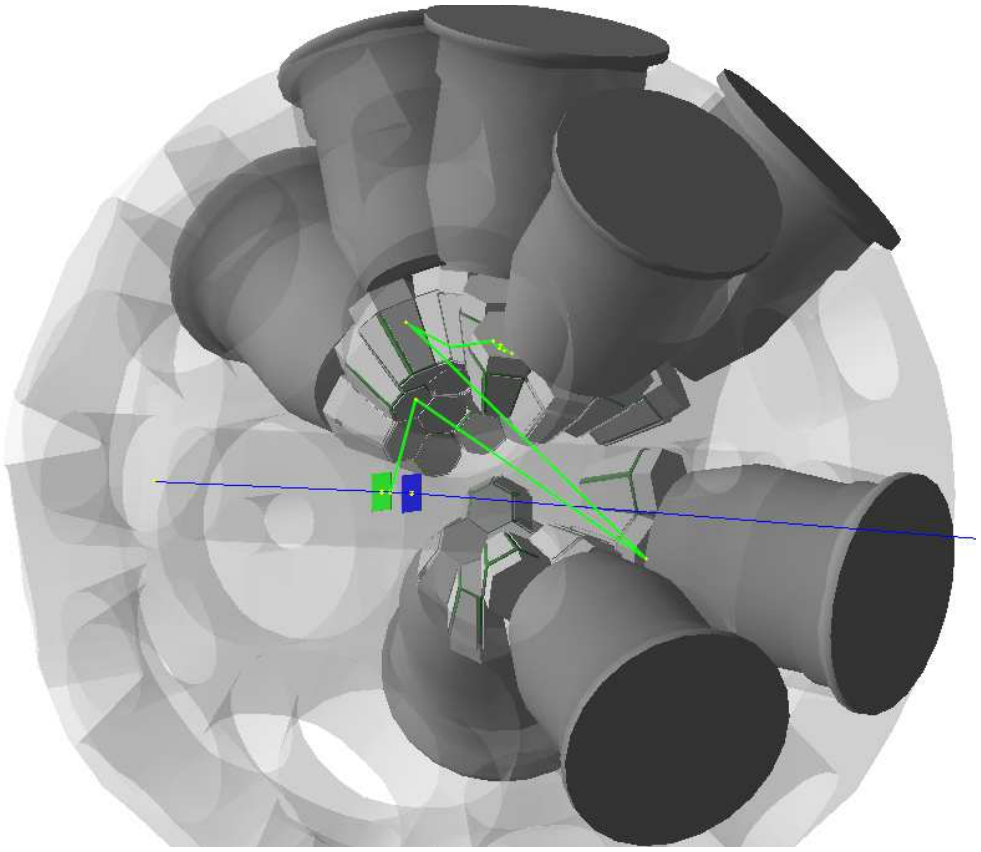

Figure 8.1: Simulated geometry of GRETINA for a single event with a single γ ray (green line) emitted from between the target (green) and the degrader (blue). The ^{24}F beam enters from the left, is converted to ^{21}O in the target and then leaves to the right. The γ ray (green line) is emitted between the target and the degrader and scatters multiple times throughout the setup.

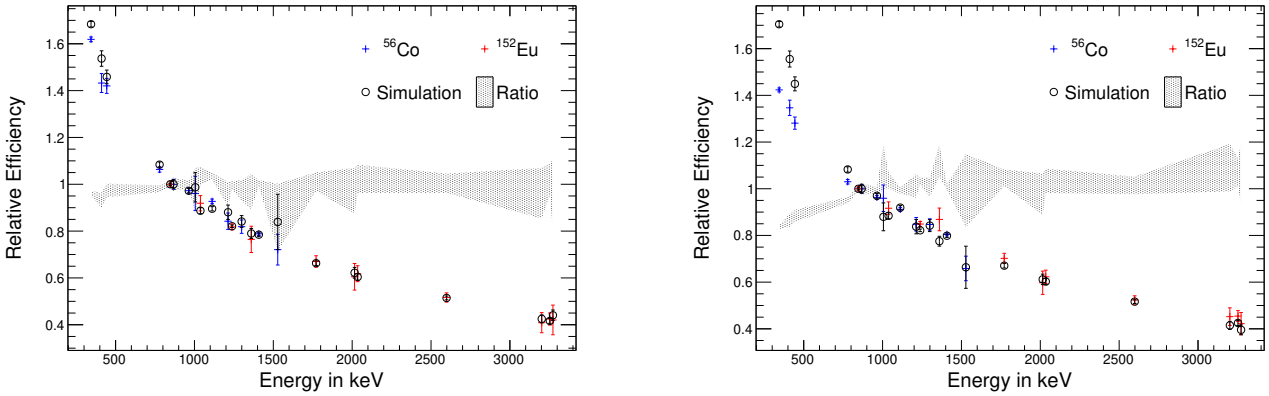

Figure 8.2: Comparison of the relative efficiencies of two source measurements and simulations for two crystals of GRETINA, one with good agreement (left) and one with bad agreement (right). The dotted confidence band shows the ratio of simulated and measured relative efficiency. The two sources are ^{56}Co and ^{152}Eu. The intensities are normalized to the 847 keV transition for the ^{56}Co source and the 867 keV transition for the ^{152}Eu source. The simulated relative efficiency mostly matches the measurement very well, with systematic deviations only occurring at energies below 800 keV.

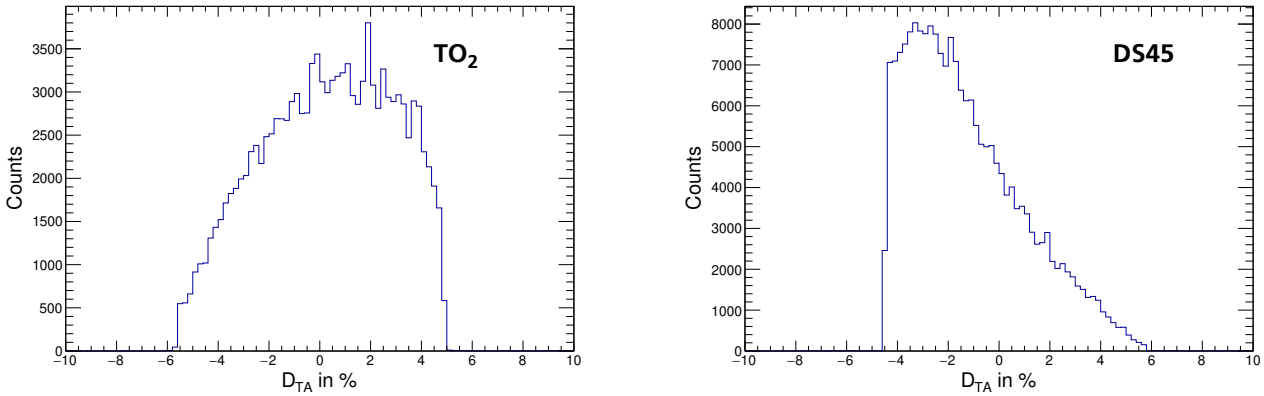

Figure 8.3: Momentum distributions of ^{21}O in the S800 for TO_2 (left) and DS45 (right). D_{TA} shows the relative deviation of the measured rigidity from the mean rigidity set for the S800. As can be seen, the S800 is cutting on a different part of the momentum distribution of ^{21}O for the settings with and without degrader.

8.2 Energy Resolution

To reproduce the measurement as precisely as possible, the simulations include the momentum spread of the incoming beam and the detector response of GRETINA. The acceptance of the S800 is also included, especially the asymmetry of the momentum acceptance visible in Figure 8.3. It shows that the S800 is cutting on a very different part of the momentum distribution of ^{21}O for $TO_{1,2}$ than for $DS25_{1,2}$ and DS45. The simulations have therefore been adjusted to incorporate this information as it was measured in the experiment.

However, some parameters are not accessible and, as such, cannot be explicitly included in the simulation. This is for example the case for the position or angle of the beam on the target in the dispersive plane. Since the dispersive properties of the S800 are used to measure the momentum, the position and angle information at the target cannot be determined. Similarly, imperfections and non-uniformities of the target and degrader, or time dependent variations of, e.g., the beam energy, are not accounted for. Therefore, the simulated spectra are modified with an additional resolution. For this, it is assumed that all remaining effects lead to a Gaussian resolution in the γ-ray energy. Both, the simulated and the measured resolutions, are determined by fitting Gaussian functions to the peaks which have no significant lifetime and thus a Gaussian shape. The simulated spectra are then folded with a Gaussian function of appropriate, energy dependent width, to match the measured resolutions. The width of the Gaussian is thereby taken as a linear function of the energy

$$\sigma = \eta + \alpha \times E, \tag{8.1}$$

with the constants for each setting as listed in Table 8.1.

8.3 Results

With the Geant4 simulations reliably reproducing the measurement, the next step is to compare the simulated spectra to the measured ones to determine the DRR, branching ratios, and lifetimes. The energies of the transitions have been determined from the measurement by fits

Table 8.1: Parameters of the Gaussian resolution applied to the simulations to match the energy resolution of the measurement.

	$TO_{1,2}$	$DS25_1$	$DS25_2$	DS45
η in keV	2.0	0.5	0.0	0.5
α in keV MeV^{-1}	2.0	7.0	7.3	7.7

to the different peaks and confirmed with corresponding simulations. With these energies, the simulations are done for every relevant transition chain, as listed in Table 8.3. Each of the simulations contains 10^7 events. The simulations include the 1776.5 keV transition from the $5/2^+$ to the $1/2^+$ state, even though the transition is not directly visible in the measured spectra. However, even a small contribution from the transition influences the results for some of the branching ratios and thus it is included.

The five experimental settings $TO_{1,2}$, $DS25_{1,2}$, and DS45 are treated separately, each being compared to their respective simulations. The simulated total spectra S_{tot}, which will be compared to the measured data, are obtained by

$$S_{\text{tot},j} = BG_{\text{lab},j} + BG_{\text{exp},j} + n_j \times \sum_{i=1}^{9} r_i S_{i,j}. \tag{8.2}$$

For each of the settings j, the respective simulated laboratory background BG_{lab} is added to a double exponential background BG_{exp}. The strengths of the different peaks in the laboratory background are thereby obtained directly from the measured laboratory frame energy spectra (c.f. Figure 7.17) and are, therefore, fixed for the comparison with the Doppler corrected spectra. The double exponential background is the sum of two exponential functions with two fit parameters each for every setting. Furthermore, the simulated spectra $S_{i,j}$ for all transition chains i are summed up, each scaled by a factor r_i. This sum is then scaled with a factor n_j for every setting and added to the background spectra, giving the total sum spectrum. This results in a total of five parameters for every setting and additional nine parameters for the scaling of the simulations, which are the same for all settings.

The total sum spectra are then fitted to the measured data for all settings simultaneously in the range between 600 keV and 6 MeV. But, not all of the mentioned parameters are independent. The factors r_i describe the relative strength of the different transition chains. Thus, one of these parameters has to be fixed. Since the 1844 keV transition is well separated in the spectra and only occurs in a single chain, the corresponding parameter r_9 is fixed to 1. In addition, r_6 is not independent, but can be expressed by $r_6 = \frac{r_3 r_5}{r_2}$. This leaves seven fit parameters, r_i, shared between all settings and another five parameters, n_j for every setting, giving a total of 32 fit parameters.

The simulations are then performed for a wide range of different lifetimes and DRRs and fitted to the measured data. After the fit has converged, the Neyman χ^2 estimator [BC84] is calculated over a given range of the spectra according to

$$\chi^2 = \sum_i \frac{(m_i - s_i)}{m_i}, \tag{8.3}$$

Table 8.2: DRRs for all regions separately, determined from the corresponding χ^2 distributions. Within their uncertainties they all agree with the combined result of 22.6% and as such agree with the assumption that they are all equal.

Region in keV	$720-850$	$1650-1800$	$1900-2070$	$2740-2950$	all
DRR in %	$18.5^{+4.1}_{-3.9}$	$27.7^{+7.2}_{-6.7}$	$23.2^{+3.2}_{-3.1}$	$21.1^{+2.4}_{-2.3}$	$22.6^{+1.8}_{-1.8}$

where m_i is the content of bin i of the measured spectrum and s_i the respective content of the simulated bin. The result is then obtained by minimizing this χ^2. However, before it is possible to determine the lifetimes or branching ratios, the DRR needs to be known.

8.3.1 Degrader Reaction Ratio

Reactions in the degrader – instead of the target – lead to a signature in the γ-ray spectra just like a lifetime longer than the actual lifetime would, as discussed in Section 6.5. Therefore, the reactions in the degrader need to be included in the simulations, for which the value of the DRR needs to be known. However, the separation between the target and degrader could not be increased enough to directly measure the DRR for the first excited state of ^{21}O.

Instead, the DRR is determined from the higher lying states, which have sufficiently short lifetimes, such that both, the 25 mm and the 45 mm data can be used. This builds upon the assumption that the ratio with which the different excited states are populated is the same for reactions in the target and in the degrader. Since the reaction producing ^{21}O is a multi-nucleon removal – for example a proton knockout followed by two neutron evaporations – the population of the states is expected to be stochastic, and thus, independent of the target material. Therefore, four regions of the spectra, corresponding to the slow components of the 876 keV, 1844 keV, 2122 keV, and the two 3000 keV transitions, are compared to the simulations.

In principle, when determined this way, the DRR is independent of the lifetime of the first excited state used for the simulations. However, large differences in the simulated lifetime might lead to small changes in the overall shape of the background, and thus, still influence the result. To minimize this possibility, the lifetime is simulated with $\tau_{1/2^+}$=400 ps, which was obtained from preliminary fits to $\mathrm{TO}_{1,2}$, since this data is independent of the DRR.

To determine the DRR, simulations for a wide range of DRR values are fitted to the measured data. Hereby, the slow components of the peaks are not included in the fit range, since the fast components are sufficient to normalize the respective simulations. This retains the sensitivity to the DRR in the region of interest. The χ^2 estimator is then calculated over a range covering only the slow component of the peaks. The resulting χ^2 values are plotted in Figure 8.4 for the sum over all four regions. A fourth order polynomial function is fitted to the data, for which the minimum is found to be at 22.6%. The confidence interval is given by the χ^2_{min}+1 range [PG16, 524-532], which is determined to 1.8% in both directions from the polynomial fit. With this the DRR is (22.6 ± 1.8)%.

Table 8.2 shows the results of the χ^2 minimization for each of the regions separately. As can be seen, the results are all in agreement with a DRR of 22.6% within their uncertainties and as such do not challenge the assumption of them being equal. The corresponding χ^2 plots for each transition separately can be found in Figure B.1.

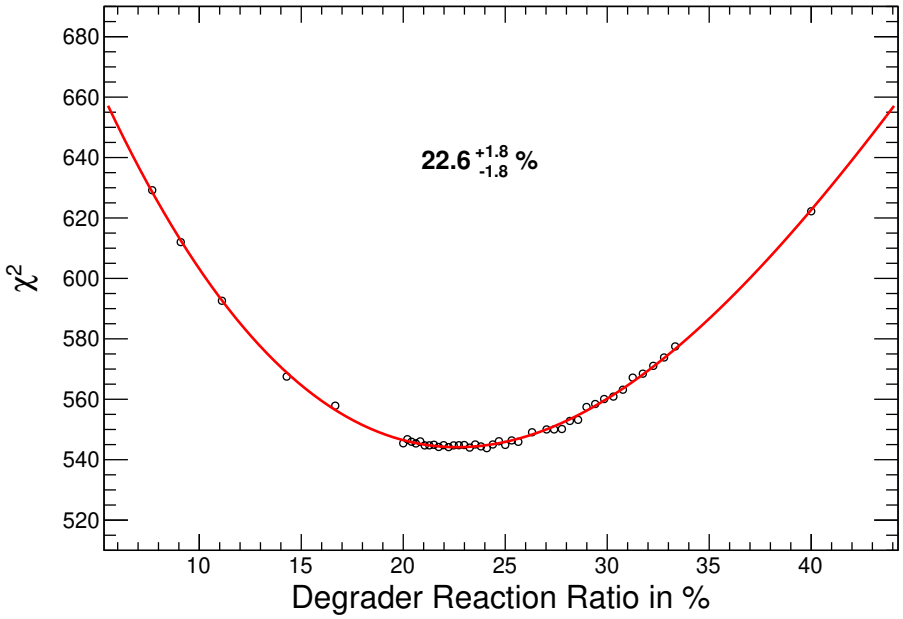

Figure 8.4: χ^2 distribution for the DRR summed over all four regions. A fourth order polynomial is fitted to the data. The minimum of the polynomial is found to be 22.6 % and the $\chi^2_{\text{min}}+1$ interval is 1.8 % in both directions.

8.3.2 Lifetimes

Similar to the DRR, the lifetime $\tau_{1/2^+}$ is determined by a χ^2 minimization. A large number of simulations are performed for a DRR of 22.6% and lifetimes ranging from 0 ps to 1000 ps. These are fitted to the measured data and the χ^2 estimator is calculated over the region from 1050 keV. to 1260 keV. The resulting χ^2 distribution is shown in Figure 8.5 for both, the full range and a zoom on the minimum. The distribution is fitted with a polylogarithmic function of fourth order, given by

$$f(\tau) = \sum_{i=0}^{4} p_i \, (\ln \tau)^i \, . \tag{8.4}$$

The minimum is found at 420 ps and the $\chi^2_{\text{min}}+1$ interval gives uncertainties of $+35$ ps and -32 ps. Figure B.2 shows the respective χ^2 distributions for the different settings separately. The resulting γ-ray energy spectra for TO_2 and DS45 with this lifetime $\tau_{1/2^+}$=420 ps are illustrated in Figure 8.6. The γ-ray energy spectra for all settings can be found in Figure B.4. The simulations for each transition chain are drawn in various colours, together with the laboratory frame background on top of the exponential background. The sum of all simulations and the background reproduce the measured data very well over the whole energy range.

In addition to the statistical uncertainties, a few systematic uncertainties need to be evaluated. First and foremost, the DRR is a key factor for the determination of the lifetime. To access the systematic uncertainties originating from the DRR, the analysis is repeated for simulations with different DRRs, especially for values with $\pm 1\sigma$. The resulting lifetimes are 426 ps and 415 ps for DRRs of 20.8% and 24.4%, respectively.

Furthermore, due to the centroid shift (c.f. Figure 6.5), the simulated energy of the transition of interest influences the resulting lifetime. Thus, the simulations are repeated for different

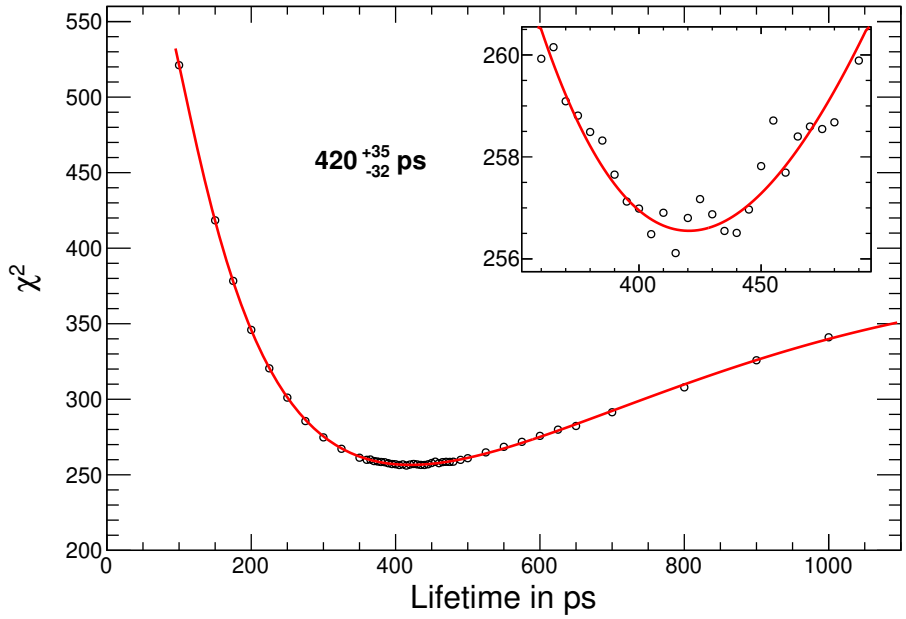

Figure 8.5: χ^2 distribution for $\tau_{1/2^+}$ with a feeding lifetime of $\tau_{3/2^+}$=7.5 ps and a DRR of 22.6 %. The inlay shows a zoom to the minimum of the distribution. The data is fitted with a polylogarithmic function of fourth order. The minimum of this function is found at 420 ps and the $\chi^2_{\text{min}}+1$ interval gives the statistical uncertainties of +35 ps and −32 ps.

transition energies. Taking an uncertainty of ±2.2keV, as discussed in Section 6.2, the resulting systematic uncertainties are +28 ps and −7 ps.

Finally, the feeding contribution has to be estimated. Since the 900.5 keV transition is the only observed transition populating the $1/2^+$ state, the lifetime of the $3/2^+$ state needs to be investigated. The peak shape of the 2122 keV transition – or rather the lack thereof – already tells that the lifetime $\tau_{3/2^+}$ has to be significantly shorter than $\tau_{1/2^+}$=420 ps. In fact, the first onset of a non-Gaussian shape starts at a lifetime of around 50 ps, which gives a first limit of $\tau_{3/2^+}$<50 ps. But the centroid shift provides an even stronger constraint.

The $3/2^+$ state decays either directly to the ground state (2122 keV) or via a cascade over the $1/2^+$ state (900.5 keV and 1221.5 keV). Because of the significantly longer lifetime $\tau_{1/2^+}$, the centroid shift due to $\tau_{3/2^+}$ only affects the 900.5 keV and 2122 keV transitions. Therefore, the centroid shift can be used to determine the lifetime $\tau_{3/2^+}$ by matching the three measured energies. With the beam velocity of this experiment the centroid shift is approximately described by

$$\frac{\Delta E}{E} = 0.0071 \times \left(1 - e^{-0.06\,\text{ps}^{-1}\times\tau}\right), \tag{8.5}$$

which has been determined by fit to simulations for various lifetimes (c.f. Figure B.3).

Indeed, to match the energies a lifetime of $\tau_{3/2^+}\approx$7.5 ps is needed. To keep the difference of the observed energies below the combined statistical uncertainties of all three transitions of ±4 keV, the lifetime needs to be between 0 and 28.5 ps, resulting in $\tau_{3/2^+} = 7.5^{+21}_{-7.5}$ ps.

With such a short lifetime $\tau_{3/2^+}$, the influence of the feeding is negligible. Therefore, the final result for the lifetime of the $1/2^+$ state is

$$\tau_{1/2^+} = 420^{+35}_{-32}(\text{stat})^{+6}_{-5}(\text{sys}_{\text{DRR}})^{+28}_{-7}(\text{sys}_{\text{E}}) = 420^{+35}_{-32}(\text{stat})^{+34}_{-12}(\text{sys}).$$

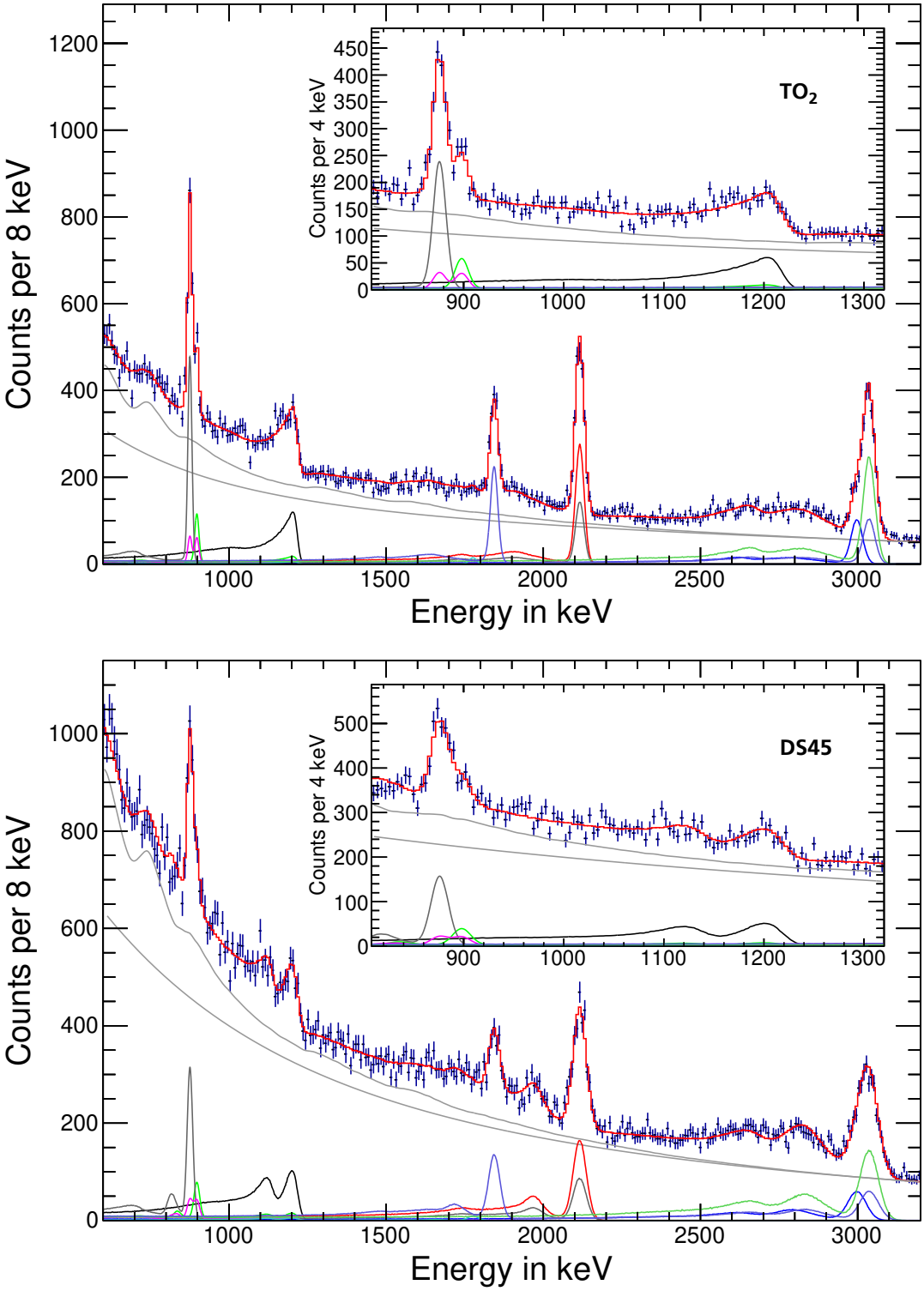

Figure 8.6: Comparison of the ^{21}O spectra with the final simulations for a lifetime $\tau_{1/2^+}$=420 ps, a feeding lifetime $\tau_{3/2^+}$=7.5 ps, and a DRR of 22.6% for TO_2 and DS45. The simulations for the different transition chains are shown in various colours. The laboratory frame background (grey) is shown on top of the double exponential background (grey). The sum of all simulated spectra and the background (red) reproduces the measured data (blue) very well. The inlay shows a zoom onto the region of interest.

Table 8.3: Summary of the simulated transition chains and the corresponding fit parameters. The values and uncertainties are obtained from the fit to the data for $\tau_{1/2^+}$=420 ps, $\tau_{3/2^+}$=7.5 ps, and a DRR of 22.6 %. The values of r_6 and r_9 are not determined by fit, but either determined from other values or fixed to 1.

J^π	$1/2^+$	$3/2^+$		$5/2^+$				$7/2^+$	$9/2^+$
E in keV	1221.5	2122		2998				3037	4881
γ_1	1221.5	2122	900.5	2998	876	876	1776.5	3037	1844
γ_2			1221.5		2122	900.5	1221.5		3037
γ_3						1221.5			

Parameter	r_1	r_2	r_3	r_4	r_5	r_6	r_7	r_8	r_9
value	1.326	1.518	0.202	0.941	0.819	0.063	0.050	2.329	1
uncertainty	0.074	0.070	0.019	0.053	0.040	0.012	0.027	0.124	-

8.3.3 Branching Ratios

With the lifetimes and the DRR known, the final simulations for these values are fitted to the measured data. With these fits, the branching ratios can then be determined from the relative intensities of the different peaks. Table 8.3 lists the results for the fit parameters for each transition chain together with their uncertainties. Since all simulations were done for the same number of events, the branching ratios are given by:

$$\begin{aligned}
BR\left(3/2^+ \to 5/2^+_{\mathrm{gs}}\right) &= \frac{r_2}{r_2 + r_3} &&= (88.3 \pm 1.2)\% \\
BR\left(5/2^+ \to 3/2^+\right) &= \frac{r_5 + r_6}{r_4 + r_5 + r_6 + r_7} &&= (48.3 \pm 1.6)\% \\
BR\left(5/2^+ \to 1/2^+\right) &= \frac{r_7}{r_4 + r_5 + r_6 + r_7} &&= (2.6 \pm 1.4)\% \\
BR\left(5/2^+ \to 5/2^+_{\mathrm{gs}}\right) &= \frac{r_4}{r_4 + r_5 + r_6 + r_7} &&= (49.1 \pm 1.5)\%,
\end{aligned}$$

with $r_6 = \frac{r_3 r_5}{r_2}$. As can be seen, the transition of 1776.5 keV is observed with a significance of less than 2σ. This is not enough to confirm its observation, though, it influences the results for the other branching ratios of the $5/2^+$ state. Within the limits of the uncertainties of the lifetimes and the DRR, no significant systematic dependence of the branching ratios is observed. As such, the uncertainties of the branching ratios are calculated from the uncertainties obtained from the fit parameters r_i and their correlations.

8.4 Comparison to Theory

Finally, the experimental results are compared to various calculations, for which the basics are summarized in Section 6.3 and Section 6.4. The first one is a shell model calculation based on the effective USDB interaction [Bro18]. The second calculation is based on an NN+3N interaction, for which an sd valence-space Hamiltonian was decoupled via IM-SRG [HSM18]. The remaining ones are MR-IM-SRG NCSM calculations [VR18], based on four different interactions, EM(400) [Nav07], EM(500) [EM03], EMN [EMN17], and N^2LO_{SAT} [EJW15]. N^2LO_{SAT} is thereby an interaction derived from chiral EFT, which has in addition been fitted to some medium mass nuclei, namely ^{14}C and ^{22,24,26}O.

A summary of the excitation spectra obtained from these calculations and the measurement is given in Figure 8.7. As can be seen, the NCSM calculation with the N^2LO_{SAT} interaction does not result in a good energy spectrum, with a drastic overestimation of the first and second excited state. For calculations with the EM(400) interaction the energy of the second excited state is slightly underestimated. Going to the more advanced EM(500) and EMN interactions improves the second excited state, but, now overestimating the two states at 3 MeV. In general, though, all three interactions, EM(400), EM(500), and EMN provide very consistent descriptions of the energy spectrum for all excited states. Contrasting this with the bad performance of the N^2LO_{SAT} interaction, this is surprising, as N^2LO_{SAT} is explicitly fitted to data from oxygen isotopes, while the other three interactions are limited to data for $A \leq 4$.

NN+3N(sd) slightly overestimates all but the highest excitation energy, while USDB slightly overestimates the energy of the first excited state. Both calculations provide energy spectra which are a in good agreement with the experimental data. Neither the NN+3N(sd) nor the USDB calculation, however, provide estimates of the uncertainties.

One issue, common among all models, is the difficulty to reproduce the ordering of the $5/2^+$ and the $7/2^+$ excited state, with NN+3N(sd) giving both excitations basically the same energy.

Table 8.4 extends this picture towards the electromagnetic transition rates in ^{21}O. It lists the measured branching ratios, lifetimes, and transition strengths, together with the respective calculated values, using either the experimental transition energies (black) or the calculated energies (grey).

For both versions, USDB significantly overestimates the B(E2) transition strength, and thus, underestimates the $1/2^+$ lifetime. For the NN+3N(sd) calculation, the resulting B(E2) strength is underestimated. However, this is to be expected, based on a systematic underestimation of the B(E2) strength reported in [HHR18], which, although not yet fully understood, is attributed to the IM-SRG. Using the calculated energies instead, brings the calculated lifetimes and branching ratio into very good agreement with the measurement.

An underestimation of the B(E2) strength can also be seen for the NCSM calculations using the EM(400) interaction. Again, using the calculated energies improves the resulting lifetime, but, it significantly deteriorates the branching ratio. However, the large sensitivity of the lifetimes to the transition energy (c.f. Equation 6.29) in combination with the uncertainties of the calculated energies results in very sizeable uncertainties of the calculated lifetime. The more advanced EM(500) and EMN interactions, on the other hand, provide a rather consistent picture, with a good agreement of the B(E2) strength and, thus, do not exhibit the systematic underestimation reported in [HHR18]. A path for explaining the different B(E2) results between the NCSM

Table 8.4: The branching ratio, lifetimes, and transition strengths, calculated using the experimental transition energies (black) and the calculated energies (grey). A discussion of the values is found in the text.

	BR in %	τ in ps		B(E2) in $e^2\text{fm}^4$			B(M1) in μ_N^2	
	$3/2^+ \to 1/2^+$	$1/2^+$	$3/2^+$	$1/2^+ \to 5/2^+_{gs}$	$3/2^+ \to 1/2^+$	$3/2^+ \to 5/2^+_{gs}$	$3/2^+ \to 1/2^+$	$3/2^+ \to 5/2^+_{gs}$
Exp	11.7 ± 1.2	$420^{+35\ +34}_{-32\ -12}$	$7.5^{+21}_{-7.5}$	$0.71^{+0.07\ +0.02}_{-0.06\ -0.06}$				
USDB	20.3	176	2.7	1.69	2.06	3.54	5.6	0.62
	9.7	98	4.0					
NN+3N(sd)	12.7	704	1.9	0.42	0.61	0.55	5.3	2.61
	12.0	481	1.6					
N_2LO_{SAT}	$4.6^{+5.5}_{-2.6}$	$444^{+128}_{-\ 81}$	$1.2^{+0.8}_{-0.3}$	0.67 ± 0.15	0.63 ± 0.05	0.70 ± 0.06	3.0 ± 1.2	4.6 ± 1.9
	$0.3^{+1.7}_{-0.3}$	$8^{+16}_{-\ 5}$	$0.3^{+0.1}_{-0.1}$					
EM(400)	$12.5^{+3.2}_{-2.5}$	804 ± 22	1.0 ± 0.2	0.37 ± 0.01	0.47 ± 0.05	0.55 ± 0.02	9.8 ± 1.0	5.1 ± 0.8
	$5.2^{+13.9}_{-\ 4.3}$	637^{+966}_{-347}	$1.6^{+1.1}_{-0.6}$					
EM(500)	$14.1^{+2.4}_{-1.9}$	488 ± 25	1.3 ± 0.2	0.61 ± 0.03	0.74 ± 0.08	0.77 ± 0.04	8.4 ± 0.4	3.7 ± 0.5
	$9.8^{+9.8}_{-5.4}$	238^{+426}_{-138}	$1.1^{+0.5}_{-0.3}$					
EMN	15.5 ± 1.3	513^{+94}_{-69}	1.5 ± 0.1	0.58 ± 0.09	0.7 ± 0.07	0.77 ± 0.06	8.2 ± 0.5	3.2 ± 0.1
	$4.7^{+4.5}_{-2.6}$	98^{+347}_{-69}	$1.2^{+0.3}_{-0.2}$					

calculations lies in the technical differences between the interactions. While EM(400) uses a local 3N regulator, EM(500) and EMN employ non-local regulators. As such, this case would demonstrate the sensitivity of the electromagnetic transition strength to such details of the interaction, which do not manifest in the energy spectrum.

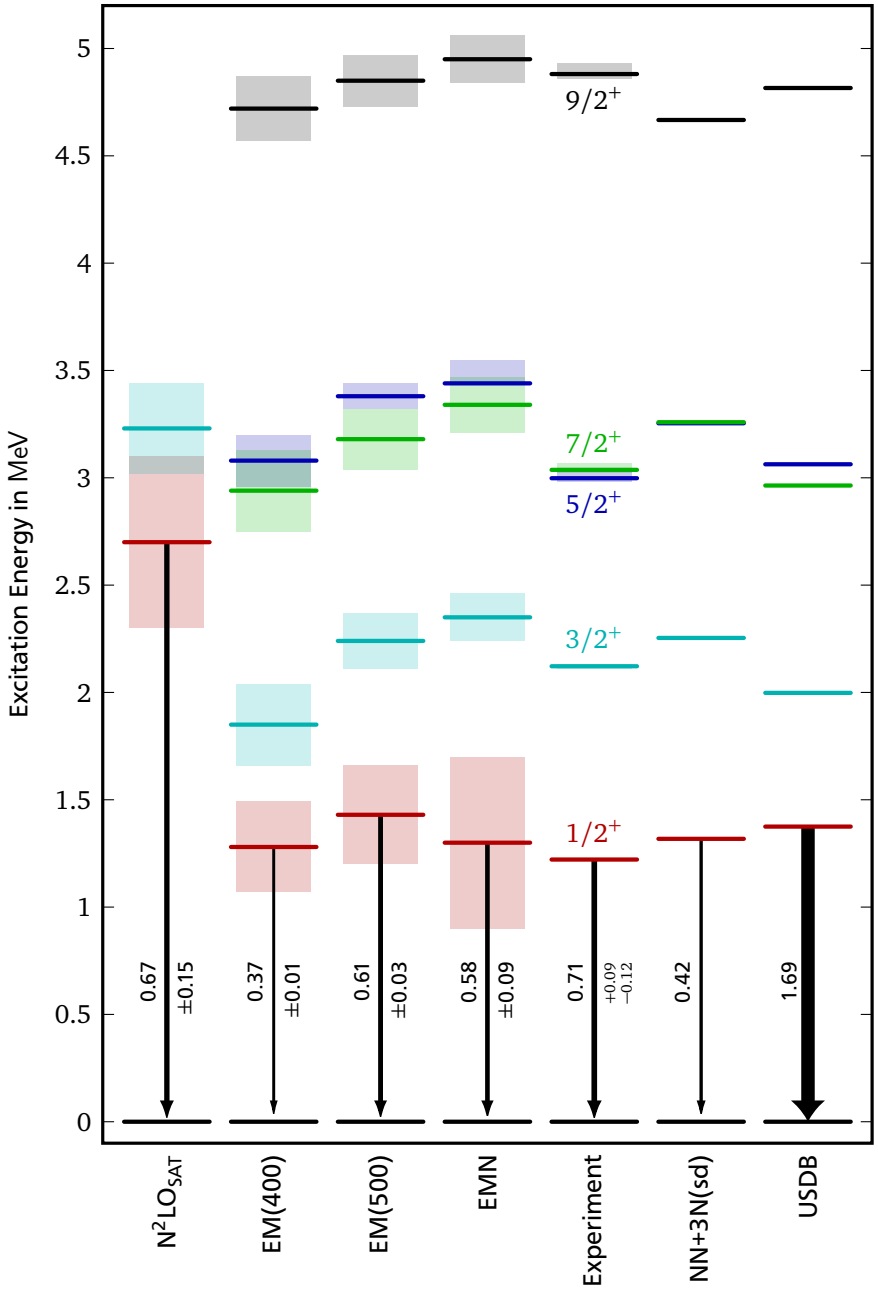

Figure 8.7: Comparison of the calculated energies of the excited states in ^{21}O from various models. Where applicable, uncertainties are given by shaded bands. Furthermore, the respective B(E2) transition strengths are given with black arrows. For the NCSM calculations with the N^{2}LO$_{\text{SAT}}$ interaction the energy spectrum did not converge to reasonable results. On the other hand, the EM(400), EM(500), and EMN interactions produces consistent results, with an overall good description of the energy spectrum. NN+3N(sd) slightly overestimates all but the highest excitation energy, with an, in total, good agreement. Also USDB provides in general a very good agreement with the experimental energy spectrum. One issue, common among all models, is the difficulty to reproduce the ordering of the $5/2^+$ and the $7/2^+$ state. For NN+3N(sd) these two excitations are on top of each other.

9 Conclusion

This thesis presented two distinct topics, the introduction of the self-calibration concept for CTAs and the measurement of the electromagnetic transition rates in ^{21}O.

The self-calibration and the underlying concept was introduced and its general viability demonstrated. Based on simulations and starting from idealized test cases, the method proved to be very stable for increasingly realistic scenarios. The influence of, e.g., the energy resolution can be seen as mostly negligible, while the acquired statistics in a respective measurement are key to an optimal calibration. Furthermore, the influence of the coalescence distance of interactions and an unknown interaction sequence was investigated with a simplistic tracker. The input data was thereby preprocessed with this tracker to determine the interaction sequence. The resulting data, including the wrong interaction sequences, was used as input for the self-calibration. Motivated by the successful handling of this input data, the tracking was included into the iterative process, making the self-calibration independent of any external signal basis for the tracking.

The achievable fidelity and accuracy of the produced signal basis is thereby primarily limited by the statistics. An estimation of the required measurement time suggests a successful calibration of the full detector array on the scale of two weeks. The explicit application to a real detector, though, still requires significant work. Nonetheless, the results of this investigation are very promising, bringing the intrinsic limits of the position reconstruction of these detector systems within reach.

The measurement of the electromagnetic properties of ^{21}O was performed and analysed. The analysis builds upon Geant4 simulations of the various excited states and the background, which were then compared to the measured γ-ray spectra. The DRR was found to be (22.6 ± 1.8)%, yielding a lifetime of the first excited state of $\tau_{1/2^+}=420^{+35}_{-32}(\text{stat})^{+34}_{-12}(\text{sys})$ ps. The transition between the $3/2^+$ and the $1/2^+$ state of (900.5 ± 1.0) keV was observed for the first time and the respective branching ratio was found to be (11.7 ± 1.2)%. Furthermore, an effective upper limit for the lifetime of the second excited state was determined as $\tau_{3/2^+}=7.5^{+21}_{-7.5}$ ps. In addition, the branching ratios of the $5/2^+$ state at 3 MeV were measured as $\text{BR}\left(5/2^+ \rightarrow 1/2^+\right)=(48.3 \pm 1.6)$% and $\text{BR}\left(5/2^+ \rightarrow 5/2^+_{\text{gs}}\right)=(49.1 \pm 1.5)$%.

These results allow for a comparison to shell model calculations and NCSM calculations, benchmarking the underlying interactions. The comparison to shell model calculations using the effective USDB interaction reveals a good agreement of the energy spectrum, however, also a clear overestimation of the B(E2) transition strength in ^{21}O. The calculations based on the NN+3N(sd) interaction also produce a good energy spectrum. On the other hand, however, the results underestimate the B(E2) strength. This, might not be unexpected, since a general underestimation of the B(E2) strength for such calculations has been reported before [HHR18]. The origin of this underestimation, though, is still under discussion.

The NCSM calculation based on $\text{N}^2\text{LO}_{\text{SAT}}$ does not produce a good energy spectrum, in contrast to the three other interactions, which produce very consistent results. This is especially surprising, given that $\text{N}^2\text{LO}_{\text{SAT}}$ has been fitted to some properties of oxygen isotopes in addition to the typical low mass data.

The NCSM result based on EM(400) underestimates the B(E2) strength, similar to the NN+3N(sd) case. This might be a consequence of EM(400) using a local 3N regulator. This assumption is consistent with the good reproduction of the B(E2) strength by the NCSM calculations with EM(500) and EMN, as these interactions use a non-local 3N regulator. The detailed interpretation of the results is, however, still ongoing. In this case, though, it would demonstrate the sensitivity of the electromagnetic transition rates to such details of the interaction, which do not manifest in the energy spectrum.

A Appendix to Self-Calibration

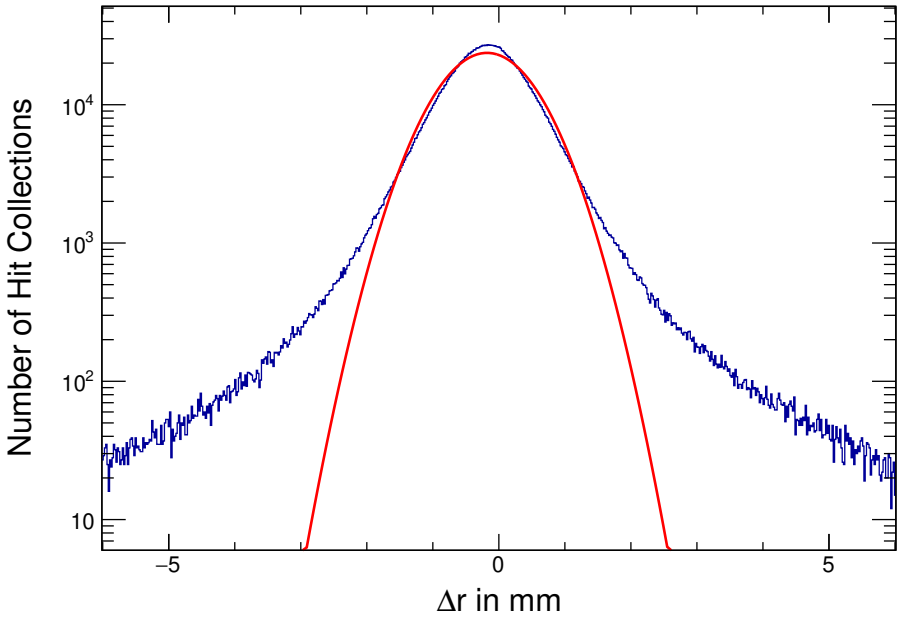

Figure A.1: Illustration of the non-Gaussian shape of the resulting position distribution after 10 iterations for a hit collection width of 3 mm. A Gaussian fit to the data is shown in red. The difference of the RMSD_r and σ_r is caused by the shoulders of the distribution.

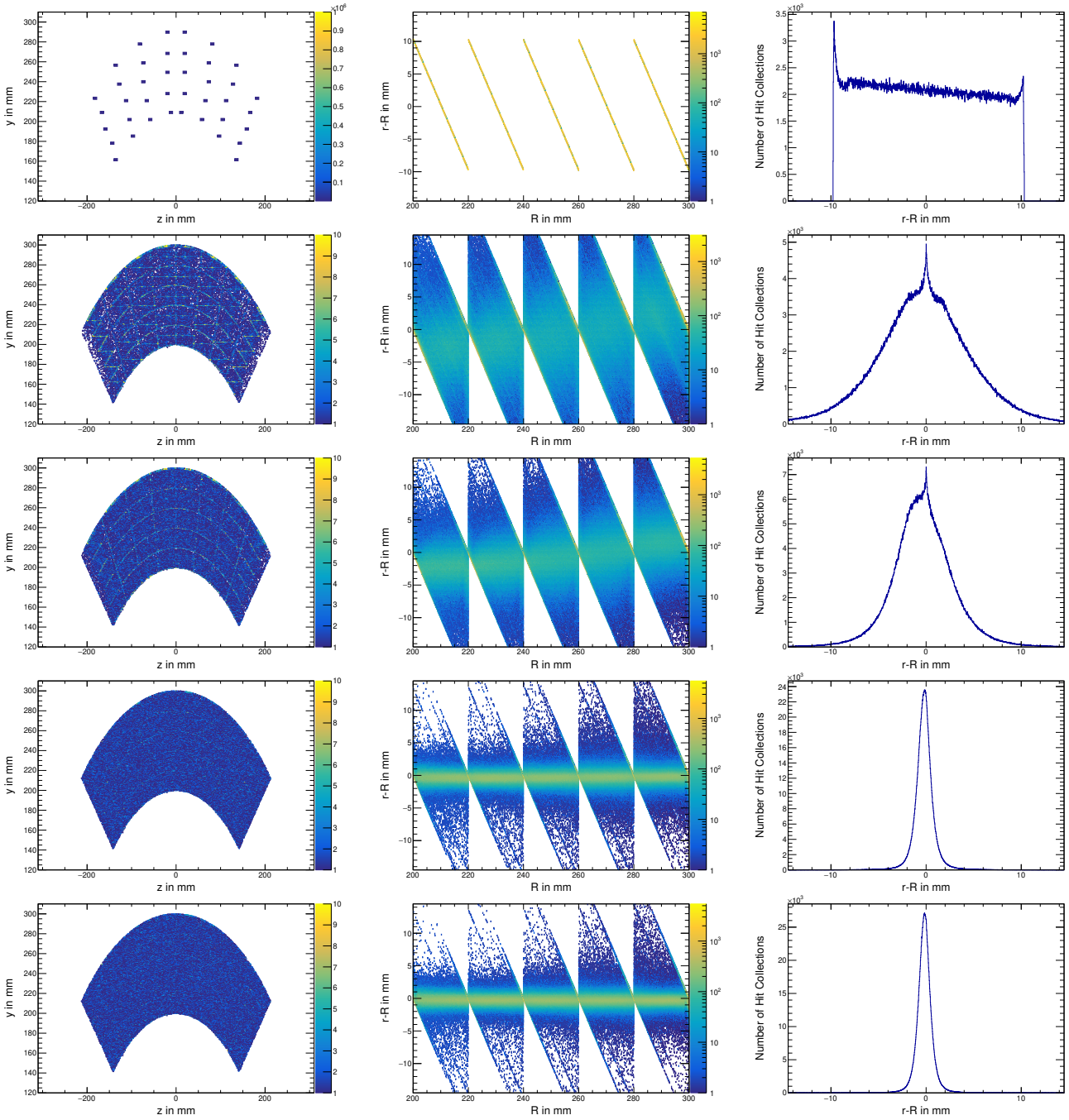

Figure A.2: Overview of the results of the self-calibration procedure for a realistic detector size and a hit collection diameter of 3 mm. The left column shows the hit collection positions in a slice of the detector. The middle column shows the difference Δr of the radius of the self-calibrated position r and the real position R plotted over R. The right column shows Δr for all hit collections. The plots show from top to bottom: Starting condition, 1st, 2nd, 10th, and 100th iteration. The resulting $\mathrm{RMSD_r}$ of the radius of the self-calibrated and real position of the hit collections after 100 iterations is 0.979 mm. The systematic offset is −0.174 mm.

B Appendix to ^{21}O

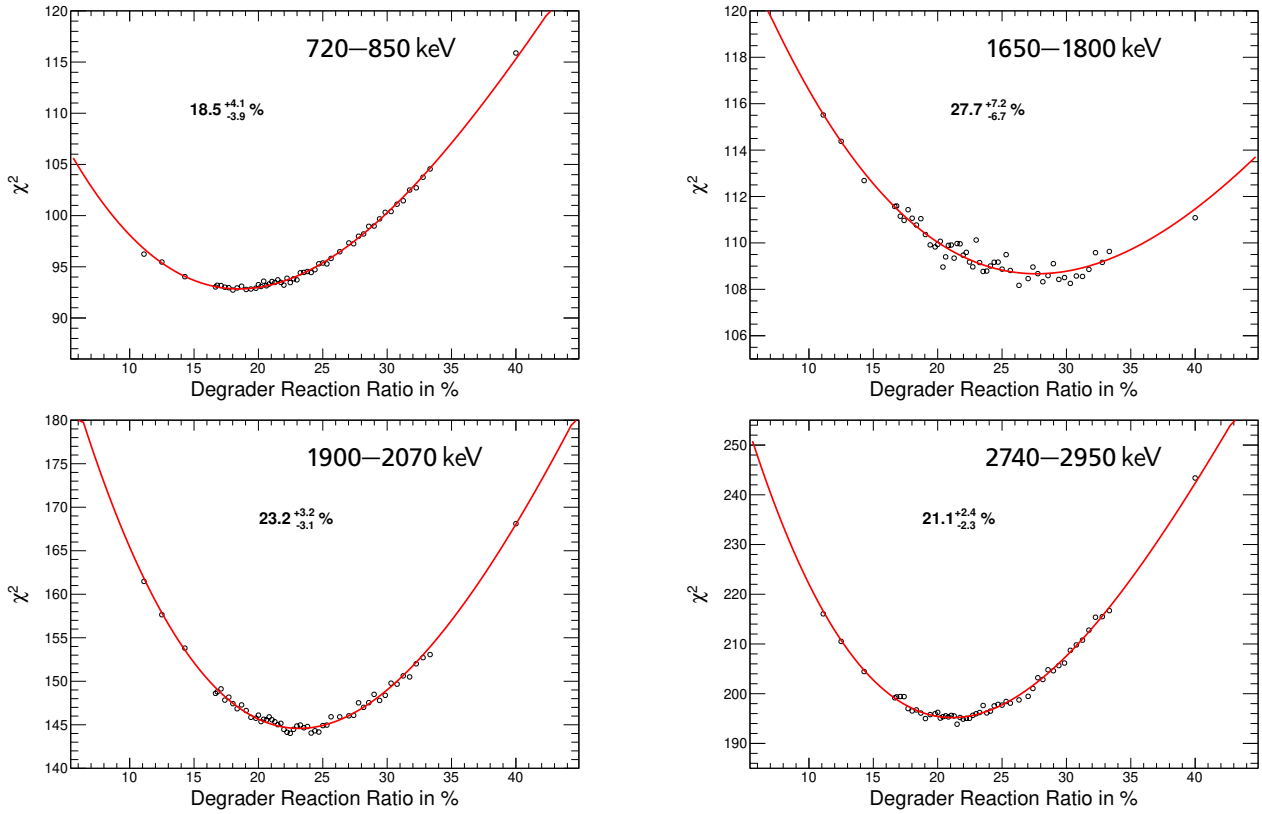

Figure B.1: χ^2 distributions for the DRR for each transition separately. Fourth order polynomials are fitted to the data. The minima of the polynomials and the $\chi^2_{\text{min}}+1$ intervals are given in the figures.

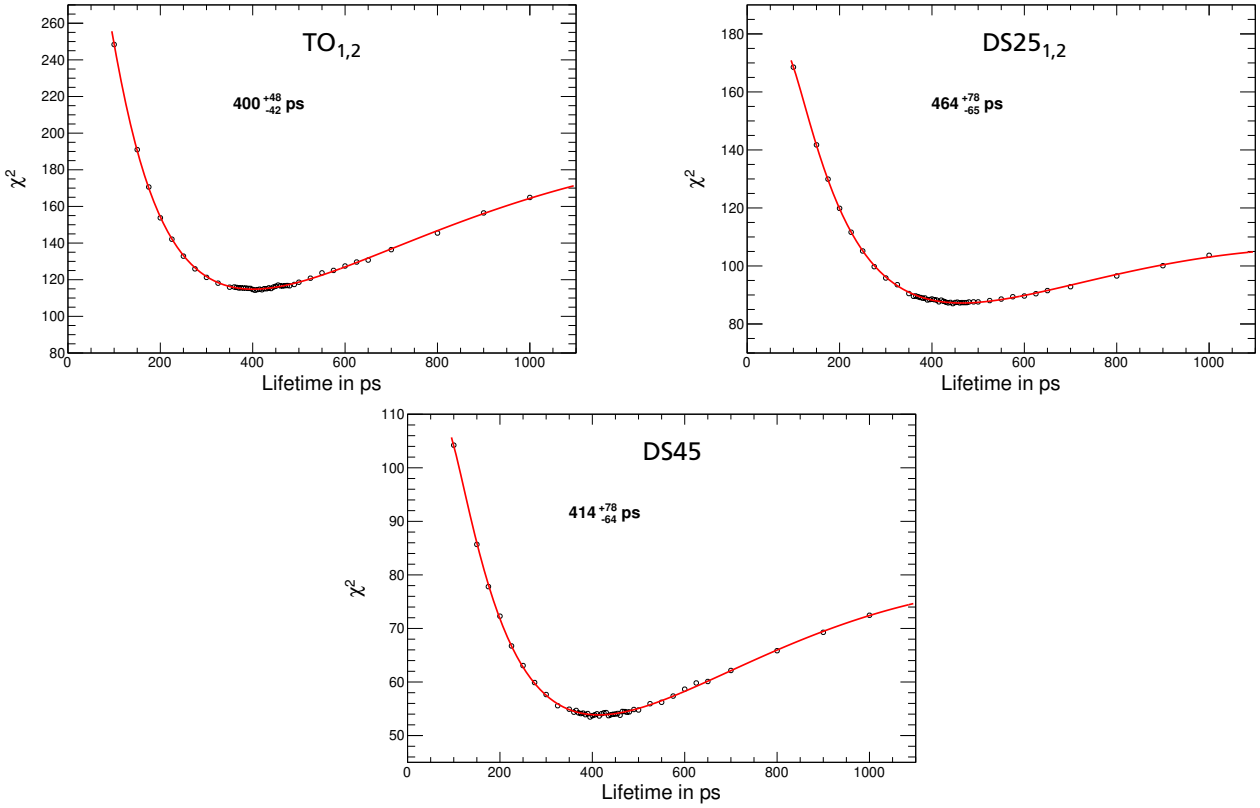

Figure B.2: χ^2 distributions for the lifetime of the $1/2^+$ state for the different settings. The data for settings $TO_{1,2}$ are combined, as are the data for $DS25_{1,2}$. Fourth order polylogarithmic functions are fitted to the data. The minima of the fits and the $\chi^2_{min}+1$ intervals are given in the figures.

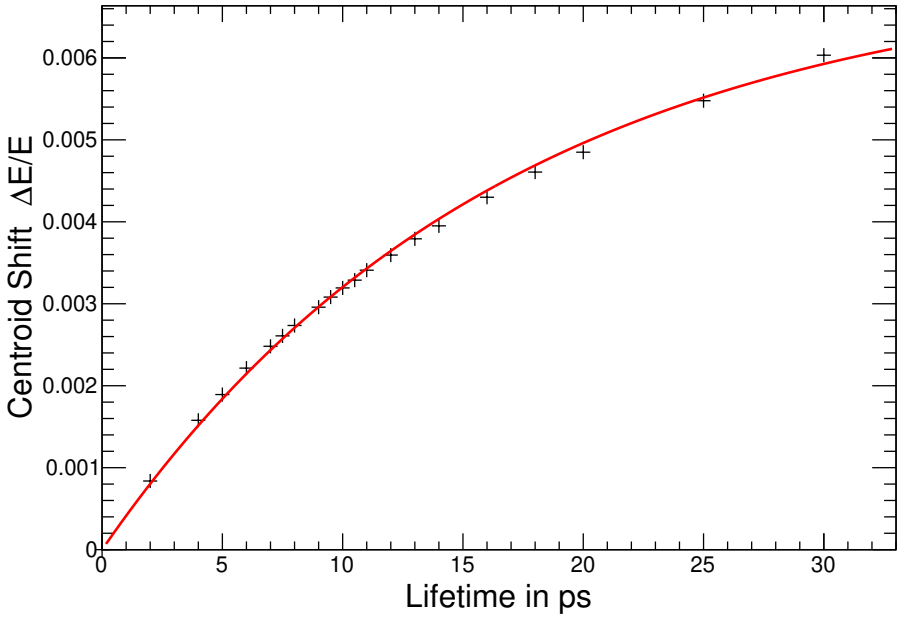

Figure B.3: Centroid shift depending on the lifetime. The centroid shift has been simulated with the beam parameters of the ^{21}O measurement. The red fit is an approximation to the data, given by Equation 8.5.

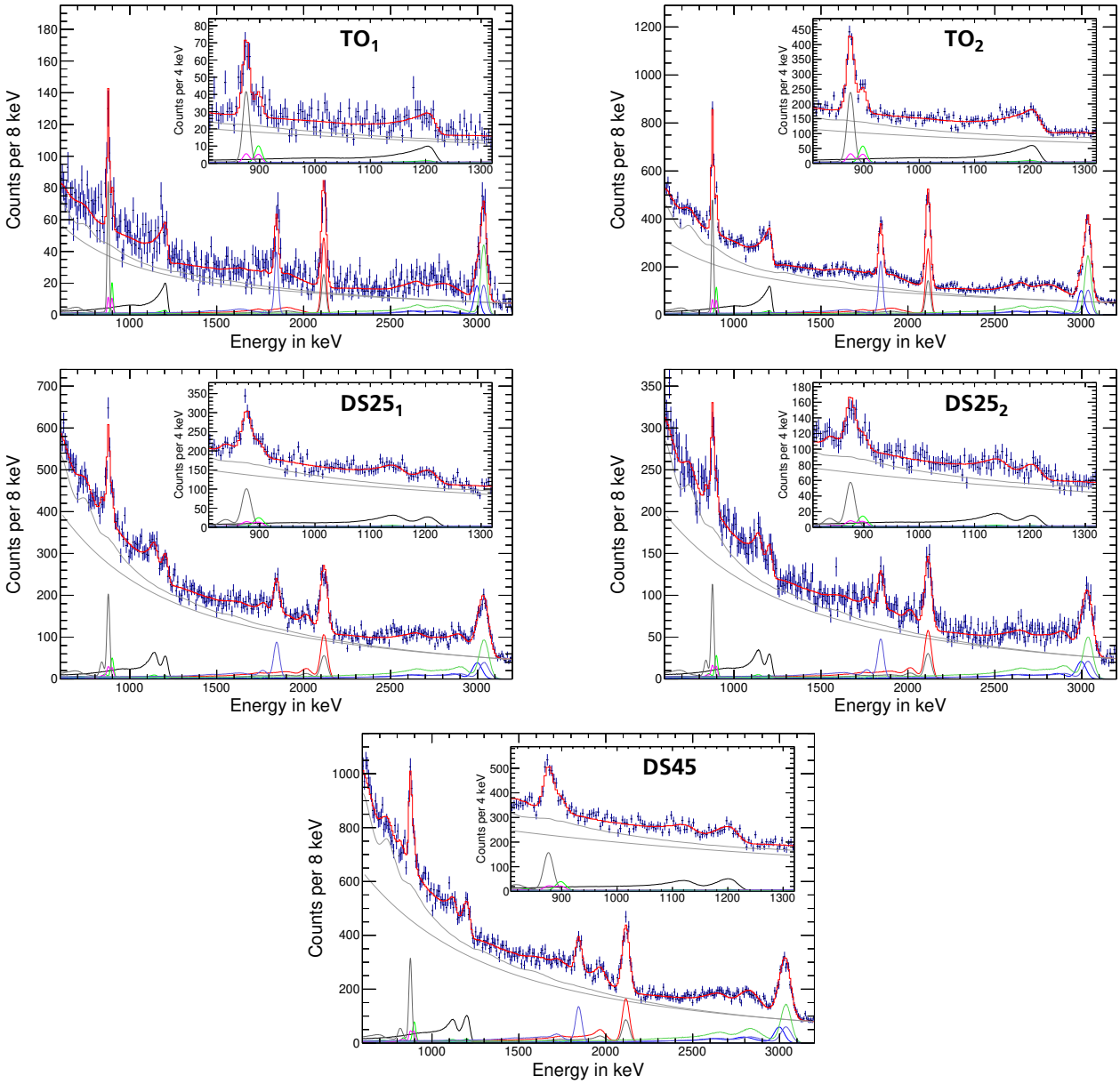

Figure B.4: Comparison of the ^{21}O spectra with the final simulations for a lifetime $\tau_{1/2^+}$=420 ps, a feeding lifetime $\tau_{3/2^+}$=7.5 ps, and a DRR of 22.6 % for all settings. The simulations for the different transition chains are shown in various colours. The laboratory frame background (grey) is shown on top of the double exponential background (grey). The sum of all simulated spectra (red) reproduces the measured data (blue) very well.

List of Figures

List of Tables

Bibliography

[AAA03] S. Agostinelli, J. Allison, K. Amako, et al. Geant4 - A Simulation Toolkit. *Nuclear Instruments and Methods in Physics Research Section A: Accelerators, Spectrometers, Detectors and Associated Equipment*, 506(3):250–303, July 2003. doi:10.1016/s0168-9002(03)01368-8.

[AAA12] S. Akkoyun, A. Algora, B. Alikhani, et al. AGATA - Advanced Gamma Tracking Array. *Nuclear Instruments and Methods in Physics Research, Section A: Accelerators, Spectrometers, Detectors and Associated Equipment*, 668:26–58, March 2012. doi:10.1016/j.nima.2011.11.081.

[AEM09] P. Adrich, D. Enderich, D. Miller, et al. A Simulation Tool for Recoil Distance Method Lifetime Measurements at NSCL. *Nuclear Instruments and Methods in Physics Research Section A: Accelerators, Spectrometers, Detectors and Associated Equipment*, 598(2):454–464, January 2009. doi:10.1016/j.nima.2008.09.055.

[Ale17] Constantia Alexandrou. Novel applications of Lattice QCD: Parton Distributions, proton charge radius and neutron electric dipole moment. *EPJ Web of Conferences*, 137:01004, 2017. doi:10.1051/epjconf/201713701004.

[ALOM81] D. E. Alburger, C. J. Lister, J. W. Olness, and D. J. Millener. Beta Decay of ^{21}O. *Physical Review C*, 23(5):2217–2233, May 1981. doi:10.1103/physrevc.23.2217.

[Bay50] Z. Bay. Calculation of Decay Times from Coincidence Experiments. *Physical Review*, 77(3):419–419, February 1950. doi:10.1103/physrev.77.419.

[Baz04] Dino Bazzacco. The Advanced Gamma Ray Tracking Array AGATA. *Nuclear Physics A*, 746:248–254, December 2004. doi:10.1016/j.nuclphysa.2004.09.148.

[BB13] B. Bruyneel, , B. Birkenbach, et al. Correction for Hole Trapping in Agata Detectors Using Pulse Shape Analysis. *The European Physical Journal A*, 49(5):61, May 2013. doi:10.1140/epja/i2013-13061-4.

[BBOS06] S. R. Beane, P. F. Bedaque, K. Orginos, and M. J. Savage. Nucleon-Nucleon Scattering from Fully Dynamical Lattice QCD. *Physical Review Letters*, 97(1), July 2006. doi:10.1103/physrevlett.97.012001.

[BBR16] B. Bruyneel, B. Birkenbach, and P. Reiter. Pulse Shape Analysis and Position Determination in Segmented HPGe Detectors: The Agata Detector Library. *The European Physical Journal A*, 52(3):70, March 2016. doi:10.1140/epja/i2016-16070-9.

[BC84] Steve Baker and Robert D. Cousins. Clarification of the Use of Chi-square and Likelihood Functions in Fits to Histograms. *Nuclear Instruments and Methods in Physics Research*, 221(2):437–442, April 1984. doi:10.1016/0167-5087(84)90016-4.

[BCS03] D. Bazin, J. A. Caggiano, B. M. Sherrill, J. Yurkon, and A. Zeller. The S800 Spectrograph. *Nuclear Instruments and Methods in Physics Research Section B: Beam Interactions with Materials and Atoms*, 204:629–633, May 2003. doi:10.1016/s0168-583x(02)02142-0.

[Ber07] Carlos A. Bertulani. *Nuclear Physics in a Nutshell*. Princeton University Press, 2007.

[BFP07] S. K. Bogner, R. J. Furnstahl, and R. J. Perry. Similarity renormalization group for nucleon-nucleon interactions. *Physical Review C*, 75(6), June 2007. doi:10.1103/physrevc.75.061001.

[BHH14] S. K. Bogner, H. Hergert, J. D. Holt, et al. Nonperturbative Shell-model Interactions from the In-medium Similarity Renormalization Group. *Physical Review Letters*, 113(14), October 2014. doi:10.1103/physrevlett.113.142501.

[BHK55] Z. Bay, V. P. Henri, and H. Kanner. Statistical Theory of Delayed-Coincidence Experiments. *Physical Review*, 100(4):1197–1208, November 1955. doi:10.1103/physrev.100.1197.

[BHS18] M. J. Berger, J. H. Hubbell, S. M. Seltzer, et al. XCOM: Photon Cross Section Database (version 1.5). `http://physics.nist.gov/xcom`, December 2018.

[BJN93] M. Berz, K. Joh, J. A. Nolen, B. M. Sherrill, and A. F. Zeller. Reconstructive correction of aberrations in nuclear particle spectrographs. *Physical Review C*, 47(2):537–544, February 1993. doi:10.1103/physrevc.47.537.

[BKS03] S. K. Bogner, T. T. S. Kuo, and A. Schwenk. Model-independent Low Momentum Nucleon Interaction from Phase Shift Equivalence. *Physics Reports*, 386(1):1–27, October 2003. doi:10.1016/j.physrep.2003.07.001.

[BLCR14] Sven Binder, Joachim Langhammer, Angelo Calci, and Robert Roth. Ab initio path to heavy nuclei. *Physics Letters B*, 736:119–123, September 2014. doi:10.1016/j.physletb.2014.07.010.

[BNV13] Bruce R. Barrett, Petr Navrátil, and James P. Vary. Ab initio no core shell model. *Progress in Particle and Nuclear Physics*, 69:131–181, March 2013. doi:10.1016/j.ppnp.2012.10.003.

[BR96] Rene Brun and Fons Rademakers. ROOT - An Object Oriented Data Analysis Framework. *Nucl. Inst. & Meth. in Phys. Res. A*, 389:81–86, September 1996. See also http://root.cern.ch.

[BR06] B. Alex Brown and W. A. Richter. New USD Hamiltonians for the sd shell. *Physical Review C*, 74(3), September 2006. doi:10.1103/physrevc.74.034315.

[Bro17] B. Alex Brown. The Oxygen Isotopes. *International Journal of Modern Physics E*, 26(01n02):1740003, January 2017. doi:10.1142/s0218301317400031.

[Bro18] Alex Brown, March 2018. Private communication.

[BW88] B. A. Brown and B. H. Wildenthal. Status of the Nuclear Shell Model. *Annual Review of Nuclear and Particle Science*, 38(1):29–66, December 1988. doi:10.1146/annurev.ns.38.120188.000333.

[BW12] J. M. Blatt and V. F. Weisskopf. *Theoretical Nuclear Physics*. Springer New York, 2012.

[Cas01] Richard F. Casten. *Nuclear Structure from a Simple Perspective*. Oxford University Press, 2001.

[CBN13] A. Cipollone, C. Barbieri, and P. Navrátil. Isotopic Chains Around Oxygen from Evolved Chiral Two- and Three-Nucleon Interactions. *Physical Review Letters*, 111(6), August 2013. doi:10.1103/physrevlett.111.062501.

[CFOW89] W. N. Catford, L. K. Fifield, N. A. Orr, and C. L. Woods. Study ^{19}N and ^{21}O by multinucleon transfer. Technical report, Australian National Univ., 1989.

[CSA13] C. Caesar, J. Simonis, T. Adachi, et al. Beyond the Neutron Drip Line: The Unbound Oxygen Isotopes ^{25}O and ^{26}O. *Physical Review C*, 88(3), September 2013. doi:10.1103/physrevc.88.034313.

[CWB93] W.-T. Chou, E. K. Warburton, and B. Alex Brown. Gamow-Teller beta-decay rates for A≤18 nuclei. *Physical Review C*, 47(1):163, January 1993. doi:10.1103/physrevc.47.163.

[Dem04] Wolfgang Demtröder. *Experimentalphysik 4: Kern-, Teilchen- und Astrophysik (Springer-Lehrbuch) (German Edition)*. Springer, 2004.

[DLL05] M. Descovich, I. Y. Lee, P. N. Luke, et al. Effects of Neutron Damage on the Performance of Large Volume Segmented Germanium Detectors. *Nuclear Instruments and Methods in Physics Research Section A: Accelerators, Spectrometers, Detectors and Associated Equipment*, 545(1-2):199–209, June 2005. doi:10.1016/j.nima.2005.01.308.

[DLV99] M. A. Deleplanque, I. Y. Lee, K. Vetter, et al. Greta: Utilizing New Concepts in γ-ray Detection. *Nuclear Instruments and Methods in Physics Research, Section A: Accelerators, Spectrometers, Detectors and Associated Equipment*, 430(2-3):292–310, July 1999. doi:10.1016/S0168-9002(99)00187-4.

[DPBD12] C. Domingo-Pardo, D. Bazzacco, P. Doornenbal, et al. Conceptual Design and Performance Study for the First Implementation of AGATA at the In-flight RIB Facility of GSI. *Nuclear Instruments and Methods in Physics Research Section A: Accelerators, Spectrometers, Detectors and Associated Equipment*, 694:297–312, December 2012. doi:10.1016/j.nima.2012.08.039.

[DRG10] P. Doornenbal, P. Reiter, H. Grawe, et al. Lifetime effects for high-resolution gamma-ray spectroscopy at relativistic energies and their implications for the RISING spectrometer. *Nuclear Instruments and Methods in Physics Research Section A: Accelerators, Spectrometers, Detectors and Associated Equipment*, 613(2):218–225, February 2010. doi:10.1016/j.nima.2009.11.017.

[EF55] J. P. Elliott and B. H. Flowers. The Structure of the Nuclei of Mass 18 and 19. *Proceedings of the Royal Society A: Mathematical, Physical and Engineering Sciences*, 229(1179):536–563, May 1955. doi:10.1098/rspa.1955.0108.

[EJW15] A. Ekström, G. R. Jansen, K. A. Wendt, et al. Accurate Nuclear Radii and Binding Energies from a Chiral Interaction. *Physical Review C*, 91(5), May 2015. doi:10.1103/physrevc.91.051301.

[EKMN15] D. R. Entem, N. Kaiser, R. Machleidt, and Y. Nosyk. Peripheral Nucleon-Nucleon Scattering at Fifth Order of Chiral Perturbation Theory. *Physical Review C*, 91(1), January 2015. doi:10.1103/physrevc.91.014002.

[EM03] D. R. Entem and R. Machleidt. Accurate charge-dependent nucleon-nucleon potential at fourth order of chiral perturbation theory. *Physical Review C*, 68(4), October 2003. doi:10.1103/physrevc.68.041001.

[EMN17] D. R. Entem, R. Machleidt, and Y. Nosyk. High-quality Two-nucleon Potentials up to Fifth Order of the Chiral Expansion. *Physical Review C*, 96(2), August 2017. doi:10.1103/physrevc.96.024004.

[ES08] J. Eberth and J. Simpson. From Ge(Li) Detectors to Gamma-ray Tracking Arrays - 50 Years of Gamma Spectroscopy with Germanium Detectors. *Progress in Particle and Nuclear Physics*, 60(2):283–337, April 2008. doi:10.1016/j.ppnp.2007.09.001.

[FMP96] G. Fehrenbacher, R. Meckbach, and H.G. Paretzke. Fast Neutron Detection with Germanium Detectors: Computation of Response Functions for the 692 keV Inelastic Scattering Peak. *Nuclear Instruments and Methods in Physics Research Section A: Accelerators, Spectrometers, Detectors and Associated Equipment*, 372(1-2):239–245, March 1996. doi:10.1016/0168-9002(95)01289-3.

[Gam28] G. Gamow. Zur Quantentheorie des Atomkernes. *Zeitschrift für Physik*, 51(3-4):204–212, March 1928. doi:10.1007/bf01343196.

[Gam18] Gammasphere. Gammasphere Online Booklet Homepage. `http://nucalf.physics.fsu.edu/~riley/gamma/gamma3.html`, December 2018.

[GC28] R. W. Gurney and E. U. Condon. Wave Mechanics and Radioactive Disintegration. *Nature*, 122(3073):439–439, September 1928. doi:10.1038/122439a0.

[GDPH13] N. Goel, C. Domingo-Pardo, T. Habermann, et al. Characterisation of a symmetric AGATA detector using the γ-ray imaging scanning technique. *Nuclear Instruments and Methods in Physics Research Section A: Accelerators, Spectrometers, Detectors and Associated Equipment*, 700:10–21, February 2013. doi:10.1016/j.nima.2012.10.028.

[GMJK90] D. Guillemaud-Mueller, J. C. Jacmart, E. Kashy, et al. Particle Stability of the Isotopes ^{26}O and ^{32}Ne in the Reaction 44 MeV/nucleon ^{48}Ca + Ta. *Physical Review C*, 41(3):937–941, March 1990. doi:10.1103/physrevc.41.937.

[GVHR17] Eskendr Gebrerufael, Klaus Vobig, Heiko Hergert, and Robert Roth. Ab Initio Description of Open-Shell Nuclei: Merging No-Core Shell Model and In-Medium Similarity Renormalization Group. *Physical Review Letters*, 118(15), April 2017. doi:10.1103/physrevlett.118.152503.

[HBB13] H. Hergert, S. K. Bogner, S. Binder, et al. In-medium similarity renormalization group with chiral two- plus three-nucleon interactions. *Physical Review C*, 87(3), March 2013. doi:10.1103/physrevc.87.034307.

[HBC13] H. Hergert, S. Binder, A. Calci, J. Langhammer, and R. Roth. Ab Initio Calculations of Even Oxygen Isotopes with Chiral Two-Plus-Three-Nucleon Interactions. *Physical Review Letters*, 110(24), June 2013. doi:10.1103/physrevlett.110.242501.

[HBM16] H. Hergert, S. K. Bogner, T. D. Morris, A. Schwenk, and K. Tsukiyama. The In-medium Similarity Renormalization Group: A Novel Ab Initio Method for Nuclei. *Physics Reports*, 621(Supplement C):165–222, March 2016. doi:10.1016/j.physrep.2015.12.007.

[Her16] H. Hergert. In-medium Similarity Renormalization Group for Closed and Open-shell Nuclei. *Physica Scripta*, 92(2):023002, December 2016. doi:10.1088/1402-4896/92/2/023002.

[HHR18] J. Henderson, G. Hackman, P. Ruotsalainen, et al. Testing Microscopically Derived Descriptions of Nuclear Collectivity: Coulomb Excitation of ^{22}Mg. *Physics Letters B*, 782:468–473, July 2018. doi:10.1016/j.physletb.2018.05.064.

[HJS49] Otto Haxel, J. Hans D. Jensen, and Hans E. Suess. On the "Magic Numbers" in Nuclear Structure. *Physical Review*, 75(11):1766–1766, June 1949. doi:10.1103/physrev.75.1766.2.

[HMS13] J. D. Holt, J. Menéndez, and A. Schwenk. Chiral Three-nucleon Forces and Bound Excited States in Neutron-rich Oxygen Isotopes. *The European Physical Journal A*, 49(3):39, March 2013. doi:10.1140/epja/i2013-13039-2.

[HPD09] G. Hagen, T. Papenbrock, D. J. Dean, M. Hjorth-Jensen, and B. Velamur Asokan. Ab initio computation of neutron-rich oxygen isotopes. *Physical Review C*, 80(2), August 2009. doi:10.1103/physrevc.80.021306.

[HPP18] S. Heil, S. Paschalis, and M. Petri. On the Self-calibration Capabilities of Gamma-Ray Energy Tracking Arrays. *The European Physical Journal A*, 54(10), October 2018. doi:10.1140/epja/i2018-12609-0.

[HSM18] Jason Holt, Achim Schwenk, and Javier Menendez, March 2018. Private communication.

[IDB16] H. Iwasaki, A. Dewald, T. Braunroth, et al. The TRIple PLunger for EXotic Beams TRIPLEX for Excited-state Lifetime Measurement Studies on Rare Isotopes. *Nuclear Instruments and Methods in Physics Research Section A: Accelerators, Spectrometers, Detectors and Associated Equipment*, 806(Supplement C):123–131, January 2016. doi:10.1016/j.nima.2015.09.091.

[KB66] T. T. S. Kuo and G. E. Brown. Structure of finite nuclei and the free nucleon-nucleon interaction: An application to ^{18}O and ^{18}F. *Nuclear Physics*, 85(1):40–86, September 1966. doi:10.1016/0029-5582(66)90131-3.

[KBB13] Z. Kohley, T. Baumann, D. Bazin, et al. Study of Two-Neutron Radioactivity in the Decay of ^{26}O. *Physical Review Letters*, 110(15), April 2013. doi:10.1103/physrevlett.110.152501.

[KCA17] J. Kahlbow, C. Caesar, T. Aumann, et al. Neutron radioactivity - Lifetime measurements of neutron-unbound states. *Nuclear Instruments and Methods in Physics Research Section A: Accelerators, Spectrometers, Detectors and Associated Equipment*, 866:265–271, September 2017. doi:10.1016/j.nima.2017.06.002.

[KN29] O. Klein and Y. Nishina. Über die Streuung von Strahlung durch freie Elektronen nach der neuen relativistischen Quantendynamik von Dirac. *Zeitschrift für Physik*, 52(11-12):853–868, November 1929. doi:10.1007/bf01366453.

[Kno89] Glenn F. Knoll. *Radiation Detection and Measurement, 2nd Edition*. Wiley, 1989.

[LCC04] I. Y. Lee, R. M. Clark, M. Cromaz, et al. GRETINA: A gamma ray energy tracking array. *Nuclear Physics A*, 746(1-4 SPEC.ISS.):255–259, December 2004. doi:10.1016/j.nuclphysa.2004.09.038.

[LDK12] E. Lunderberg, P. A. DeYoung, Z. Kohley, et al. Evidence for the Ground-State Resonance of ^{26}O. *Physical Review Letters*, 108(14), April 2012. doi:10.1103/physrevlett.108.142503.

[LDV03] I. Y. Lee, M. A. Deleplanque, and K. Vetter. Developments in Large Gamma-ray Detector Arrays. *Reports on Progress in Physics*, 66(7):1095–1144, May 2003. doi:10.1088/0034-4885/66/7/201.

[Lee90] I.-Yang Lee. The Gammasphere. *Nuclear Physics A*, 520:641–655, 1990. doi:10.1016/0375-9474(90)91181-P.

[Lee09] I. Yang Lee. Gamma-ray tracking detectors: Physics opportunities and status of GRETINA/GRETA. In *AIP Conference Proceedings*, volume 1139, pages 23–28, 2009.

[Leo87] William R. Leo. *Techniques for Nuclear and Particle Physics Experiments: A How-To Approach*. Springer-Verlag, 1987.

[LLY09] Z. H. Li, J. L. Lou, Y. L. Ye, et al. Experimental Study of the β-delayed Neutron Decay of ^{21}N. *Physical Review C*, 80(5), November 2009. doi:10.1103/physrevc.80.054315.

[LMHK04] A. Lopez-Martens, K. Hauschild, A. Korichi, J. Roccaz, and J-P. Thibaud. γ-ray Tracking Algorithms: A Comparison. *Nuclear Instruments and Methods in Physics Research Section A: Accelerators, Spectrometers, Detectors and Associated Equipment*, 533(3):454–466, November 2004. doi:10.1016/j.nima.2004.06.154.

[LQB85] M. Langevin, E. Quiniou, M. Bernas, et al. Production of Neutron-rich Nuclei at the Limits of Particles Stability by Fragmentation of Projectiles. *Physics Letters B*, 150(1-3):71–74, January 1985. doi:10.1016/0370-2693(85)90140-6.

[Mac01] R. Machleidt. High-precision, Charge-dependent Bonn Nucleon-nucleon Potential. *Physical Review C*, 63(2), January 2001. doi:10.1103/physrevc.63.024001.

[May49] Maria Goeppert Mayer. On Closed Shells in Nuclei. II. *Physical Review*, 75(12):1969–1970, June 1949. doi:10.1103/physrev.75.1969.

[ME11] R. Machleidt and D. R. Entem. Chiral Effective Field Theory and Nuclear Forces. *Physics Reports*, 503(1):1–75, June 2011. doi:10.1016/j.physrep.2011.02.001.

[MSS03] D. J. Morrissey, B. M. Sherrill, M. Steiner, A. Stolz, and I. Wiedenhoever. Commissioning the A1900 Projectile Fragment Separator. *Nuclear Instruments and Methods in Physics Research Section B: Beam Interactions with Materials and Atoms*, 204:90–96, May 2003. doi:10.1016/s0168-583x(02)01895-5.

[Nav07] P. Navrátil. Local three-nucleon interaction from chiral effective field theory. *Few-Body Systems*, 41(3-4):117–140, November 2007. doi:10.1007/s00601-007-0193-3.

[NDRS82] F. Naulin, C. Détraz, M. Roy-Stéphan, et al. Excited States of ^{19}N and ^{21}O. *Journal de Physique Lettres*, 43(2):29–32, 1982. doi:10.1051/jphyslet:0198200430202900.

[NGT85] P. J. Nolan, D. W. Gifford, and P. J. Twin. The performance of a bismuth germanate escape suppressed spectrometer. *Nuclear Instruments and Methods in Physics Research Section A: Accelerators, Spectrometers, Detectors and Associated Equipment*, 236(1):95–99, 1985. doi:10.1016/0168-9002(85)90131-7.

[NSS79] P J Nolan and J F Sharpey-Schafer. The measurement of the lifetimes of excited nuclear states. *Reports on Progress in Physics*, 42(1):1–86, January 1979. doi:10.1088/0034-4885/42/1/001.

[OSH10] Takaharu Otsuka, Toshio Suzuki, Jason D. Holt, Achim Schwenk, and Yoshinori Akaishi. Three-Body Forces and the Limit of Oxygen Isotopes. *Physical Review Letters*, 105(3), July 2010. doi:10.1103/physrevlett.105.032501.

[PG16] C. Patrignani and Particle Data Group. Review of Particle Physics. *Chinese Physics C*, 40(10):100001, August 2016. doi:10.1103/physrevd.98.030001.

[PLM13] S. Paschalis, I. Y. Lee, A. O. Macchiavelli, et al. The performance of the Gamma-Ray Energy Tracking In-beam Nuclear Array GRETINA. *Nuclear Instruments and Methods in Physics Research, Section A: Accelerators, Spectrometers, Detectors and Associated Equipment*, 709:44–55, May 2013. doi:10.1016/j.nima.2013.01.009.

[PW01] Steven C. Pieper and R. B. Wiringa. Quantum Monte Carlo Calculations of Light Nuclei. *Annual Review of Nuclear and Particle Science*, 51(1):53–90, December 2001. doi:10.1146/annurev.nucl.51.101701.132506.

[Rot09] Robert Roth. Importance Truncation for Large-scale Configuration Interaction Approaches. *Physical Review C*, 79(6), June 2009. doi:10.1103/physrevc.79.064324.

[S8018] S800. The NSCL S800 Spectrograph. `https://wikihost.nscl.msu.edu/S800Doc/doku.php`, May 2018.

[SAD04] M. Stanoiu, F. Azaiez, Zs. Dombrádi, et al. N=14 and 16 Shell Gaps in Neutron-rich Oxygen Isotopes. *Physical Review C*, 69(3), March 2004. doi:10.1103/physrevc.69.034312.

[SCO00] E Sauvan, F Carstoiu, NA Orr, et al. One-neutron removal reactions on neutron-rich psd-shell nuclei. *Physics Letters B*, 491(1-2):1–7, October 2000. doi:10.1016/s0370-2693(00)01003-0.

[SDL99] G. J. Schmid, M. A. Deleplanque, I. Y. Lee, et al. A γ-Ray Tracking Algorithm for the Greta Spectrometer. *Nuclear Instruments and Methods in Physics Research Section A: Accelerators, Spectrometers, Detectors and Associated Equipment*, 430(1):69–83, June 1999. doi:10.1016/S0168-9002(99)00188-6.

[Sim97] J. Simpson. The Euroball Spectrometer. *Zeitschrift für Physik A Hadrons and Nuclei*, 358(2):139–143, February 1997. doi:10.1007/s002180050290.

[SMD10] C. S. Sumithrarachchi, D. J. Morrissey, A. D. Davies, et al. States in ^{22}O via β Decay of ^{22}N. *Physical Review C*, 81(1), January 2010. doi:10.1103/physrevc.81.014302.

[SP08] O. Sorlin and M.-G. Porquet. Nuclear Magic Numbers: New Features Far from Stability. *Progress in Particle and Nuclear Physics*, 61(2):602–673, October 2008. doi:10.1016/j.ppnp.2008.05.001.

[TAA97] O. Tarasov, R. Allatt, J. C. Angélique, et al. Search for ^{28}O and Study of Neutron-rich Nuclei near the N=20 Shell Closure. *Physics Letters B*, 409(1-4):64–70, September 1997. doi:10.1016/s0370-2693(97)00901-5.

[TBS11] K. Tsukiyama, S. K. Bogner, and A. Schwenk. In-Medium Similarity Renormalization Group For Nuclei. *Physical Review Letters*, 106(22), June 2011. doi:10.1103/physrevlett.106.222502.

[vdMC99] J. van der Marel and B. Cederwall. Backtracking As a Way to Reconstruct Compton Scattered Gamma-Rays. *Nuclear Instruments and Methods in Physics Research Section A: Accelerators, Spectrometers, Detectors and Associated Equipment*, 437(2–3):538–551, November 1999. doi:10.1016/S0168-9002(99)00801-3.

[VKD00] K. Vetter, A. Kuhn, M. A. Deleplanque, et al. Three-dimensional Position Sensitivity in Two-dimensionally Segmented HP-Ge Detectors. *Nuclear Instruments and Methods in Physics Research Section A: Accelerators, Spectrometers, Detectors and Associated Equipment*, 452(1-2):223–238, September 2000. doi:10.1016/S0168-9002(00)00430-7.

[VKL00] K. Vetter, A. Kuhn, I. Y. Lee, et al. Performance of the Greta Prototype Detectors. *Nuclear Instruments and Methods in Physics Research Section A: Accelerators, Spectrometers, Detectors and Associated Equipment*, 452(1-2):105–114, September 2000. doi:10.1016/S0168-9002(00)00431-9.

[VR18] Klaus Vobig and Robert Roth, September 2018. Private communication.

[vW35] C. F. v. Weizsäcker. Zur Theorie der Kernmassen. *Zeitschrift für Physik*, 96(7-8):431–458, July 1935. doi:10.1007/bf01337700.

[WBB17] D. Weisshaar, D. Bazin, P. C. Bender, et al. The Performance of the γ-ray Tracking Array GRETINA for γ-ray Spectroscopy with Fast Beams of Rare Isotopes. *Nuclear Instruments and Methods in Physics Research Section A: Accelerators, Spectrometers, Detectors and Associated Equipment*, 847(Supplement C):187–198, March 2017. doi:10.1016/j.nima.2016.12.001.

[Wei51] VF Weisskopf. Radiative transition probabilities in nuclei. *Physical Review*, 83(5):1073, September 1951. doi:10.1103/physrev.83.1073.

[WS54] Roger D. Woods and David S. Saxon. Diffuse Surface Optical Model for Nucleon-Nuclei Scattering. *Physical Review*, 95(2):577–578, July 1954. doi:10.1103/physrev.95.577.

[WSS95] R. B. Wiringa, V. G. J. Stoks, and R. Schiavilla. Accurate Nucleon-nucleon Potential with Charge-independence Breaking. *Physical Review C*, 51(1):38–51, January 1995. doi:10.1103/physrevc.51.38.

Acronyms

3N	Three-nucleon
A1900	A1900 fragment separator
AGATA	Advanced gamma tracking array
BGO	Bismuth germanium oxide
CRDC	Cathode-readout drift chamber
CTA	Compton tracking array
DRR	Degrader reaction ratio
DS25$_1$	First setting with a degrader separation of 25 mm
DS25$_2$	Second setting with a degrader separation of 25 mm
DS45	Setting with a degrader separation of 45 mm
E1	Plastic scintillator at the focal plane of the S800
EFT	Effective field theory
EM	Entem-Machleidt
EMN	Entem-Machleidt-Nosyk
ESPE	Effective single particle energy
FOM	Figure of merit
GRETA	Gamma-ray energy tracking array
GRETINA	Gamma-ray energy tracking in-beam nuclear array
HO	Harmonic oscillator
HPGe	High-purity germanium
IC	Ionization chamber
IM-SRG	In-medium SRG
mOBJ	Mesytech electronics readout of OBJ
MR-IM-SRG	Multi-reference IM-SRG
N^{2}LO	Second-next to leading order
N^{3}LO	Third-next to leading order
NN	Nucleon-nucleon
NSCL	National superconducting cyclotron laboratory
NCSM	No-core shell-model
OBJ	Plastic scintillator at the object position of the S800
PID	Particle identification
QCD	Quantum chromo dynamics

RDM	Recoil distance method
RG	Renormalization group
RMSD	Root mean square deviation
S800	S800 spectrograph
SRG	Similarity renormalization group
TBME	Two-body matrix element
TO_1	First setting using only the target
TO_2	Second setting using only the target
TOF	Time of flight
TRIPLEX	Triple plunger for exotic beams
USD	Universal sd shell
XFP	Extended focal plane scintillator

Acknowledgement

Foremost, I thank Marina Petri for her supervision, guidance, and support during my PhD. Your input was always most welcome and challenging, and despite the eventual geographical separation, there was never any doubt about your continued engagement in my work. I enjoyed every one of our interactions and the many opportunities to travel and join experiments. And in hindsight, I look back with a big smile on even the most stressful and nerve-wrecking shifts during any experiment. This is due to the combination of your own ambition – motivating and driving us to our limits during such experiments – and your honest care for our well-being, characterized by "you need sleep, this has to wait until tomorrow" and "you go now and get something to eat!... and bring me some cookies". And from all this I learned a lot about myself, the environment I want to work in, and of course nuclear physics, while the only negative impression left is a hint of bitter taste in an otherwise enjoyable, yellow fruit. ;-)

At this point I also thank Stefanos Paschalis for introducing me to the self-calibration concept and his invaluable input during its development. In addition, your help during our common experiment was the foundation upon which the rest of us could stand.

Furthermore, I want to thank Tom Aumann for welcoming me in his group. I highly value the insights to nuclear physics and I thank you for the opportunity to travel to Japan and visit the RCNP. It was always pleasant and productive to discuss with you and every problem found a quick and unbureaucratic solution.

I would also like to thank every member of the group, past and present. Be it the iFridge parties, the Christmas parties, or any other occasion, socializing with you has always been a great source of entertainment. And this translates to the work place as well. Problems are usually approached with the right amount of seriousness and humour, and in the end even the most absurd suggestions paved the way for an actual solution. Your input – serious and jest – is always welcome, and your willingness to provide it, is much appreciated. In particular, I would like to mention Fabia and Chris, who never were shy to point out if my spectra didn't look nice; Andrea and Dima for the most entertaining evenings and stories; and Sonja and Michael for the many discussions and updates. Thank you, Heiko and Vadim, for your support with the computer and server infrastructure. Thank you, Ashton and Chris, for proof reading my thesis, making sure that only those errors remain which are *their* on purpose. Thank you everyone for all the small and big things which made this possible and so enjoyable.

Outside of physics, I want to thank my friends for both, distraction and help; standing me, explaining my topic and problems, giving me an outside view and a new perspective. And after those many travels, in the name of our plants, "Carolin, thank you for saving our lives over and over again".

Und zu guter Letzt möchte ich meiner Familie danken. Meine Eltern haben es geschafft meinen Spaß am Verstehen aufrecht zu erhalten, mich weiter lernen und entwickeln zu lassen, entgegen der expliziten Bemühungen des einen oder anderen Lehrers. Ihr habt meine Entscheidungen stets unterstützt und mir geholfen diese mit gutem Gewissen treffen zu können. Ihr habt meine

Freunde zu euren gemacht und bildet den Dreh- und Angelpunkt meines Lebens. Und nicht weniger gilt für meine Schwestern und die (mittlerweile) Brüder, die sie mit sich bringen. Ihr seid die verrücktesten Chaoten, die mich stets Tränen lachen lassen. Ohne euch wäre ich nicht so geworden wie ich bin, und ich könnte nicht glücklicher damit sein.

Ähnliches gilt für Inas Familie, die mich nimmt wie ich bin, und meine Eigenarten mit einem breiten Lächeln wertschätzt. Und selbstverständlich danke ich Ina. Nichts was ich hier schreiben könnte, würde dem gerecht was du mir bedeutest.

The most exciting phrase to hear in science, the one that heralds the most discoveries, is not “Eureka“ but “That’s funny“.

(Isaac Asimov)

Erklärung zur Dissertation

Hiermit versichere ich, die vorliegende Dissertation ohne Hilfe Dritter nur mit den angegebenen Quellen und Hilfsmitteln angefertigt zu haben. Alle Stellen, die aus Quellen entnommen wurden, sind als solche kenntlich gemacht. Diese Arbeit hat in gleicher oder ähnlicher Form noch keiner Prüfungsbehörde vorgelegen.

Darmstadt, den 19. Juni 2019

(Sebastian Heil)